

## MASTER

### Design of a miniature laser scanning head for the femtoprint focal lens

Kruis, J.

*Award date:*  
2011

[Link to publication](#)

#### **Disclaimer**

This document contains a student thesis (bachelor's or master's), as authored by a student at Eindhoven University of Technology. Student theses are made available in the TU/e repository upon obtaining the required degree. The grade received is not published on the document as presented in the repository. The required complexity or quality of research of student theses may vary by program, and the required minimum study period may vary in duration.

#### **General rights**

Copyright and moral rights for the publications made accessible in the public portal are retained by the authors and/or other copyright owners and it is a condition of accessing publications that users recognise and abide by the legal requirements associated with these rights.

- Users may download and print one copy of any publication from the public portal for the purpose of private study or research.
- You may not further distribute the material or use it for any profit-making activity or commercial gain

# Design of a miniature laser scanning head

---

For the femtoprint focal lens

Johan Kruis

5/12/2011



Femtoprint, a novel 3D printing process for manufacturing integrated microstructures in transparent materials is being developed at the TU/e. One of the challenges in the development is to have sufficient printing speed for fast fabrication of complex microstructures. The challenge is addressed in this thesis with the design, fabrication and characterization of a miniature laser scanning-head based on a movable focusing lens principle. The realised suspension design of the miniature laser scanning-head is a parallel structure fabricated by folding three leaf springs that confers to the lens three degree-of-freedom, pan-, tilt- and vertical translation for beam focusing. Three voice coil actuators were chosen to actuate the suspension and fiber-optic-based sensors were used to characterize the suspension motion. A rudimentary openloop voltage based-control was implemented to analyse the scanning heads specifications and performance.





# I Table of Contents

---

---

I	Table of Contents .....	III
II	Summary.....	1
Chapter 1	Introduction: the manufacturing process and requirements for a laser-scanning head ....	3
1.1	Objective of this master thesis: problem statement.....	4
1.1.1	Design specifications .....	6
1.2	Project context: the Femtoprint project .....	6
1.2.1	The femtoprinter .....	6
1.2.2	Research and applications for the Femtoprinter .....	7
Chapter 2	Focal optics selection and analysis of beam steering with a focusing lens.....	10
2.1	Focal optics selection .....	11
2.1.1	Possible future optics investigation .....	11
2.1.2	Conclusion .....	12
2.2	Beam steering methods .....	13
2.3	Theoretical beam steering model .....	13
2.3.1	Assumptions .....	13
2.3.2	Boundary conditions.....	14
2.3.3	Ray-tracing methodology .....	17
2.3.4	Model analysis.....	22
2.4	Beam steering experiments: models validation.....	28
2.4.1	Experimental setup.....	28
2.4.2	Measurement method .....	28
2.4.3	Measurement analysis .....	31
2.5	Conclusion on beam steering methods.....	33

Chapter 3	Scanning head design .....	35
3.1	Selected kinematics.....	36
3.1.1	Mobility analysis.....	36
3.2	Design realisation: miniature laser scanning head suspension.....	37
3.2.1	Dimensioning of the folded leaf springs.....	40
3.2.2	Eigenfrequencies .....	43
3.2.3	Stiffness .....	44
3.2.4	Von Mises Stress.....	49
3.3	Actuation .....	51
3.3.1	Comparison and choice .....	51
3.3.2	The voice coil .....	52
3.3.3	Sensors .....	54
3.4	Design synthesis, fabrication and assembly .....	55
3.4.1	Suspension design overview .....	55
Chapter 4	Experimental design validation .....	57
4.1	Experimental setup .....	58
4.2	Sensors qualification .....	59
4.3	Motion range measurements.....	60
4.3.1	Methodology .....	60
4.3.2	Z movement range .....	60
4.3.3	Angular motion range.....	61
4.3.4	Expected setup motion range .....	61
4.4	Stiffness measurement.....	63
4.4.1	Methodology .....	63
4.5	Frequency response measurement.....	66
4.6	The relative gain array.....	68
Chapter 5	Conclusions & Recommendations.....	71
5.1	Conclusions.....	72
5.2	Recommendations.....	72
Appendices	.....	74
A.	Other considered optics .....	75
A.1.	Reflecting objective .....	75
A.2.	Gimbal concave mirror setup .....	75
A.3.	Concave mirror through material setup.....	76

A.4.	GRIN lens .....	76
B.	Definitions of optical radii .....	77
B.1.	Airy disk radius .....	77
B.2.	GEO Radius .....	77
B.3.	RMS Radius.....	77
C.	Derivation of $Z_r(Y_r)$ .....	78
D.	Measurement results .....	79
D.1.	Translational tests with smaller NA.....	79
D.2.	Translation With larger NA.....	82
D.3.	Rotation with smaller NA .....	87
D.4.	Rotation With larger NA .....	90
E.	Additional kinematics concepts.....	94
E.1.	Concept1: Rotational bar mechanisms .....	94
E.2.	Concept 2: cardan mechanism with z-drive .....	94
E.3.	Concept3: Hybrid suspension, parasitic rotation and translation.....	95
E.4.	Concept4: Double Roberts mechanism.....	95
F.	Mechanical Drawings .....	96
F.1.	Parts list .....	96
F.2.	Frame.....	97
F.3.	Actuator leaf spring mount .....	98
F.4.	Leaf spring filling plate .....	99
F.5.	Actuator filling plate .....	100
F.6.	Folded leaf spring Membrane .....	101
F.7.	Leaf spring clamps (L clamp) .....	102
F.8.	Membrane clamp (down).....	103
F.9.	Membrane clamp (up).....	104
F.10.	Shielding tube.....	105
F.11.	Filling block.....	106
G.	Gravity and its effect on the laser scanning head .....	107
H.	Tolerance calculations.....	108
I.	System characterisation bode plots .....	110
J.	References.....	117





## II Summary

---

In the group of micro and nano scale engineering of the mechanical engineering department of the TU/e, a novel production process, called femtoprint, is being developed for manufacturing integrated microstructures in transparent materials. The process somewhat comparable to a printing process, consists of two steps: first a laser exposure step to modify material properties and second a chemical etching step to reveal laser-modified regions. The laser exposure step is a direct write process and consists of scanning contours and set of adjacent lines to define the patterns to be imprinted.

One of the challenges is to have sufficient printing speed for fabricating complex microstructures in a reasonable amount of time, i.e. compatible with industry requirements.

Although the process consists of two steps, this report focuses on the laser exposure step and on how to make it faster.

More specifically, this master thesis presents the design, fabrication and characterization of a miniature laser scanning-head based on a movable focusing lens principle.

Two beam steering principles –based on the rotations and translations of a focusing lens are discussed and compared theoretically and experimentally. The final choice was made for a pan-and-tilt beam steering method for which a lens suspension was designed.

The suspension design of the miniature laser scanning-head, forms a parallel structure fabricated by folding three leaf springs that confers to the lens three degree-of-freedom, pan- & tilt- and vertical translation for beam focusing. Three voice coil actuators were chosen to actuate the suspension and fibre-optic-based sensors were used to characterize the suspension motion. A rudimentary PID-control was implemented to test the device performances.

This report contains an overview of the design process, the dimensioning of the actual design, its implementation and fabrication as well as experimental results illustrating the performances achieved compared to the initial objectives. Recommendations for future improvements are discussed in conclusion.

This master thesis work was done part-time at Ecole Polytechnique Fédérale de Lausanne (EPFL) in Switzerland and part-time at Eindhoven University of Technology (TU/e) in the Netherlands.



## **Chapter 1 Introduction: the manufacturing process and requirements for a laser-scanning head**

---

---

This chapter discusses the production process from the viewpoint of implementing a laser-scanning head design. Our objective is to identify the critical parameters and to define the specifications for the laser scanning head. The context of this master project and how it integrates itself within a European collaborative effort is also briefly discussed.

## 1.1 Objective of this master thesis: problem statement

In the group of Micro and Nano Scale Engineering of the Mechanical Engineering department of Eindhoven University of Technology, a novel production process for monolithic glass micro devices in transparent material is being developed. A key aspect of this manufacturing process is the use of non-linear absorption properties resulting from specific exposure conditions that opens the possibility to modify transparent materials selectively and anywhere in their volume.

The production process (illustrated schematically in figure 1.1) consists of two steps: the first one being the exposure to a femtosecond pulsed-laser and the second step consisting of a chemical etching procedure. Details of the process can be found in [1][2]. Here, we briefly outline its main characteristics from the viewpoint of a laser-scanning head design.

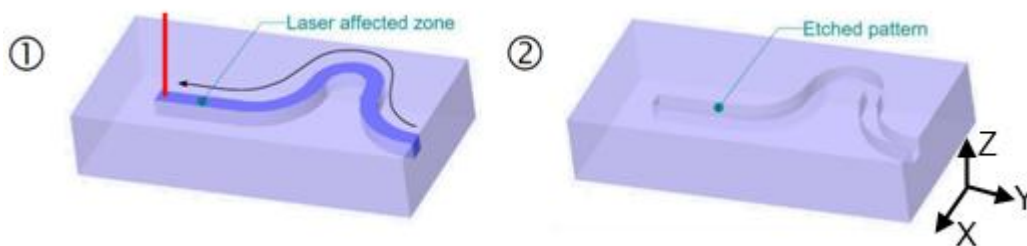


Figure 1.1: The femtoprint process as described in [3]. The first step: writing a pattern with the laser, creating the laser affected zone. The second step: Etching away the previously laser affected zone to create 3D structures.

During the first step, the laser affected zone (so called 'LAZ'), i.e. the volume in the transparent material that is modified consecutively to the laser exposure, defines an ellipsoid of which the longer axis is aligned with the light propagation direction. Although the dimensions depend on the laser exposure parameters (namely, the pulse energy, the pulse duration and the confocal parameters), typical radii of this ellipsoid are  $r_x=r_y=0.5$  [ $\mu\text{m}$ ] and  $r_z=4$  [ $\mu\text{m}$ ] [4] in the case considered in this study. By moving the LAZ across the specimen, one can form lines or more complex patterns that can be arranged spatially to form arbitrary three-dimensional patterns. In fused silica – a high purity glass, the laser affected volumes are etched about sixty times more rapidly than the pristine material.

The subject of this thesis is related to the laser exposure step and on how to make it more efficient and more integrated.

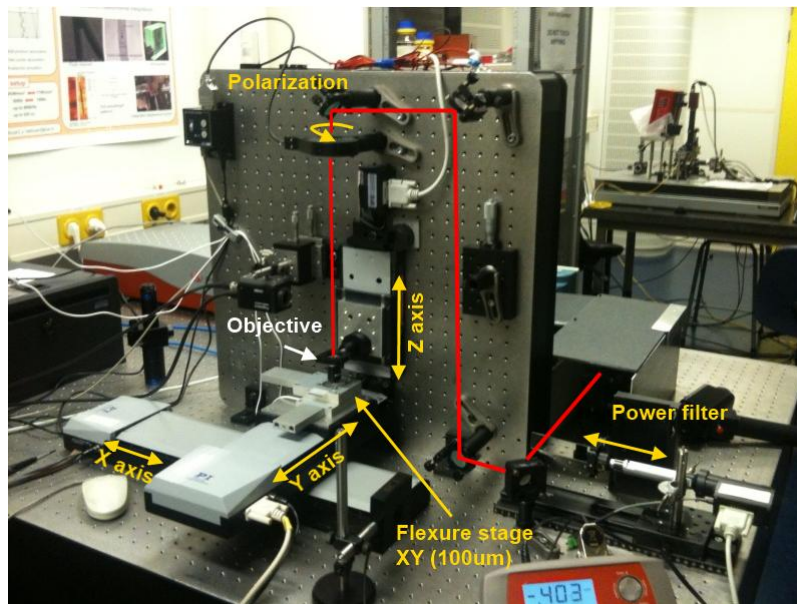


Figure 1.2: The femtoprint setup as it is currently used in the lab. The laser first is adjusted to the right power, then is polarised correctly after which it passé through an objective. The objective focuses the laser light on a moving sample.

In the current setup, the laser exposure step is performed as follows: translations in X and Y (see figure 1.2) are achieved by moving the substrate under the laser beam, translations in Z are achieved by translating the focussing objective. These movements are achieved with bulky (300 x 110 x 40 mm), relatively slow ( $V_X, V_Y = [30 \text{ mm/s}]$ , and  $V_Z = 3 [\text{mm/s}]$ ) and expensive commercial translational stages.

The machining time of products with complex geometries on the current setup is too long and should be reduced. , Furthermore, the cost and volume requirement for the current setup are limiting factors for a future low-cost integrated production centre of the size of a printer.

This thesis focuses on improving the exposure step by providing a new approach for fast writing of complex patterns. Among the possible methods for improving the process throughput, one method consists in combining coarse, large amplitude motion with a fast, short-range beam steering. This method would eventually result in trajectories such as indicated in figure 1.3, which allow for the fabrication of larger structures, these trajectories are oriented at layer by layer fabrication.

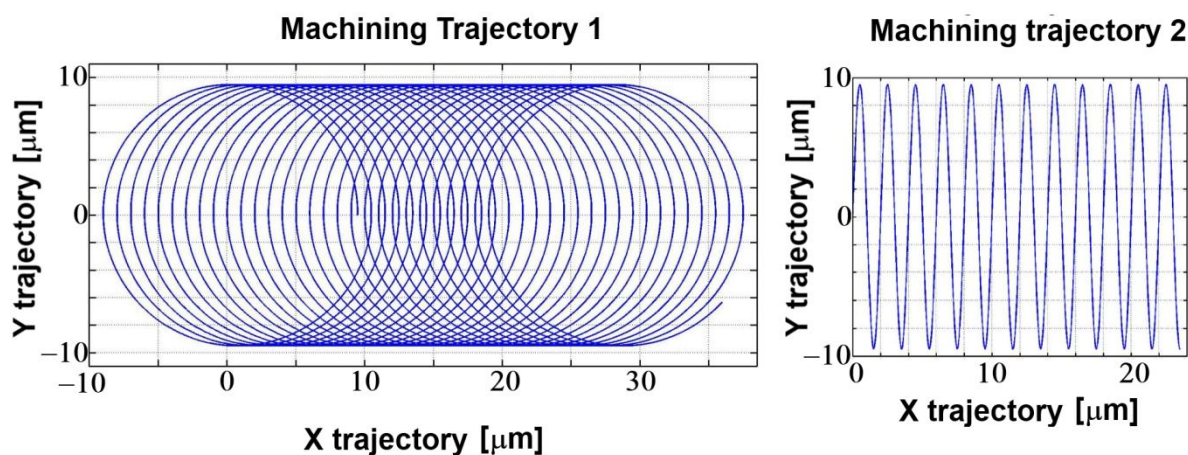


Figure 1.3: Two considered machining strategies for the production of larger structures.

Following this idea, this thesis addresses the “control of high dynamic movement of the laser affected zone by moving the focal lens.

Our goal is to develop a fast, low-cost, and miniaturized device to locally steer the laser affected zone.

### 1.1.1 Design specifications

To objective stated earlier opens up a large number of designs, optics and possibilities that cannot be entirely addressed within the scope of master thesis. So that a full design study that includes a practical realization could be realistically done within the allocated time, it was decided at the start of the project to narrow down the design options by defining a set of design specifications and requirements that are listed here:

- The considered solutions are only opto-mechanical
- The design will only consider rotational and translational variations of the focusing objective.
- The desired working space for ‘laser affected zone’ is a cylinder with a diameter of 100 [ $\mu\text{m}$ ]
- Accuracy and resolution should respectively be within 100 [nm] and 10 [nm].

## 1.2 Project context: the Femtoprint project

The project of this thesis is part of a European project called, Femtoprint ([www.femtoprint.eu](http://www.femtoprint.eu)). The project aims at designing a printer (nicknamed ‘the femtoprinter’) for Microsystems with nano-scale features in glass and other transparent materials

The objectives of this project [5] are

1. To Develop a femtosecond laser suitable for glass micro-/nano- manufacturing that fits in a shoe-box
2. To Integrate the laser in a machine similar to a printer that can position and manipulate glass sheets of various thicknesses
3. To demonstrate the use of the printer to fabricate a variety of micro-/nano-systems with optical, mechanical and fluid-handling capabilities.

The assignment of this thesis is a part of the second objective.

### 1.2.1 The femtoprinter

The femtoprinter is divided in three modules: a control module, the laser source and the printer per se. More specifically:

- The electronic and control unit contains the human-machine interface, the software and the hardware architecture of the controller.
- The Femtoprinter contains the laser head, which fulfils the laser beam scanning and the spot focusing functions. It also includes the glass substrate mounting and moving system.

- The Laser unit contains the laser source and the modulator, which will generate the femto-second pulses

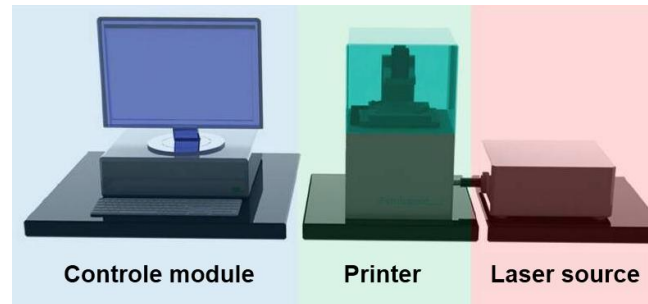


Figure 1.4: The Femtoprinter modules [5]. From left to right: The control module operates the printer and laser source. Where as the printer moves the laser affected zone through the sample to fabricate structures. The laser source provides the printer with femto-second laser pulses required for the machining.

The assignment of this thesis is to provide a novel suspension design for the optics of the Femtoprint unit. Though this will most likely not be part of the first femtoprinters, it provides a window of opportunity for miniaturisation and fast printing processes in future femtoprinters.

## 1.2.2 Research and applications for the Femtoprinter

A short overview of possible applications for the femtoprinter are provided in figure 1.5.

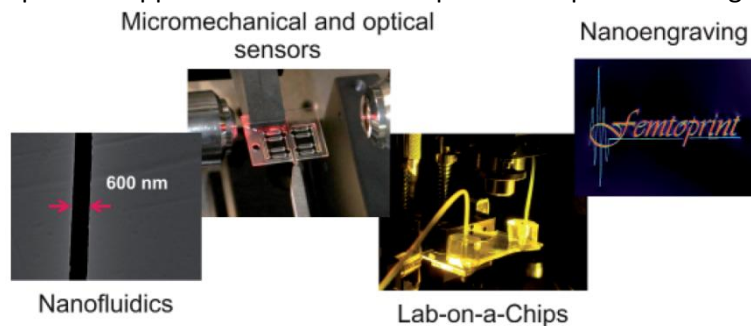


Figure 1.5: Examples of applications of the femtoprint project [5]

The topic of direct-writing of integrated optics, fluidics channels and other functional devices is broad and the literature is vast.

Some of the recent non-TU/e progress in the field has made possible fabrication of integrated optics (from first demonstrations[6][7] to complex integrated optical systems [8][9][10]), optical data storage [11], and new optical components [12].

Some of the topics which were and are being investigated by the research group at the TU/e are:

- The fabrication of high-aspect ratio microchannels[4].
- The integration of optics and micro-mechanics on a single substrate [2] [13].
- The fabrication of fused silica molds [14].
- The femtosecond laser generation of self-organised bubble patterns in fused silica [15].
- The physics of the femtoprint process itself [1][16][17].
- fabrication of transparent actuators [18]

- Lab-on-a-chip algae detection, with a femtosecond made lab-on-a-chip [19].

All in all fused silica processing with a femtosecond laser has become a good platform for monolithic integration.





## **Chapter 2 Focal optics selection and analysis of beam steering with a focusing lens**

---

---

The chapter starts by a review of the present and selected focal optics and then continues by presenting a theoretical model and its experimental validation, for two beamsteering methods with the selected focal optics.

## 2.1 Focal optics selection

### The optics used in the present-day setup

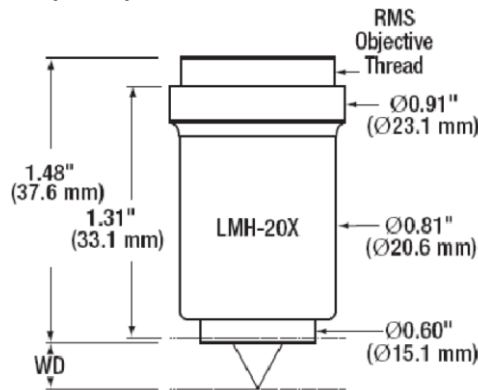


Figure 2.1: The present-day focal optics, the LMH-20X-1064 microscope objective.

In the setup used for micromachining at the TU/e, the current objective is the LMH-20X-1064 from Thorlabs. It weighs 51 g and costs approximately € 1300. The lenses are made from fused silica and are selected to severely limit diffraction; the airy disk size is 1.6  $\mu\text{m}$ . Furthermore the design has a better than 96-98% transmission for the design wavelength range. Also the volume it takes up is  $\varnothing$  23.1 by 38 mm.

#### 2.1.1 Possible future optics investigation

The focal optics of the future femtoprinter is desired to have several properties. They need to be relatively inexpensive whilst still achieving appropriate quality for the femtoprinted structures. From this demand a set of specifications can be derived being:

- Aberrations should be minimized, because they distort the focus and intensity profile. For a better overview of basic aberrations the reader is referred to [20].
- Design wavelength of the optics as close as possible to the lasers wavelength (1030 nm).
- As little optical path length through other mediums than air because it may modify the temporal characteristics of the pulses when the pulse duration gets shorter (like for instance less than 100 fs).
- The lens should preferably not be of a polymer material, due to the chance of material degradation and lens performance degradation.
- A lower mass than the current test-setup (< 51 g) objective, in order to achieve better system dynamics
- A numerical aperture (NA) of 0.4 or higher
- A relatively small volume, to minimise inertias.

Various optical possibilities were considered among these are, a reflecting objective, a concave mirror setup, GRIN lenses, and aspheric lenses. In the end an aspheric lens was selected, the other options are briefly reviewed in annex 0.

## Aspheric lens

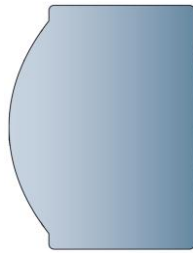


Figure 2.2: Aspheric lens

A possible replacement for the current objective is an aspheric lens. The main advantage of an aspheric lens is that it compensates for spherical aberration. Furthermore their mass is relatively low (about 200 mg).

### 2.1.2 Conclusion

The choice was made for an aspheric lens (more specifically the reference 352350-C from Thorlabs with a design wavelength of 980 [nm]) that offers the best compromise in term of weight, volume and optical performances.

The specifications of the aspheric lens chosen for this project are provided in table 2.1 and compared with the microscope objective currently used for micromachining. The definitions of the radii mentioned in table 2.1 can be found in annex B.

Table 2.1: Comparison between the selected Aspheric lens and the microscope objective currently used for machining.

Focal optics	LMH-20X-1064 Microscope Objective	352350-C Aspheric lens
Design Wavelength [nm]	1064	980
Geometry [mm]	Ø23.1 by 38	Ø4.7by 3.64
Mass [gram]	51	0.21
Air disk Radius[ $\mu\text{m}$ ]	1.607	1.503
Numerical Aperture [-]	0.4	0.42
Cost [€]	1300	80
GEO Radius [nm]	242	114
RMS Radius [nm]	162	74

From this comparison, although the design wavelength is slightly away from the laser wavelength, the asphere is expected to have comparable if not better optical performances with the advantage of having a lens significantly smaller, lighter and less expensive. On the other hand, the aspheric being made of plastic that has less good dispersion performance than fused silica, it is not excluded that the lens slightly degrades the temporal characteristics of the femtosecond laser beam. Considering the fact that relatively long pulses (between 300 and 400 fs) are used and the thickness of the material, it is assumed that such effects should be limited, if not negligible.

## 2.2 Beam steering methods

One of the approaches for beam steering is translation (illustrated in figure 2.3 middle) of the lens by a set distance. For a perfect lens, translating it by a distance  $\Delta X$ , results in the same displacement of the focused spot. So this principle can be used as a method of printing on a substrate.

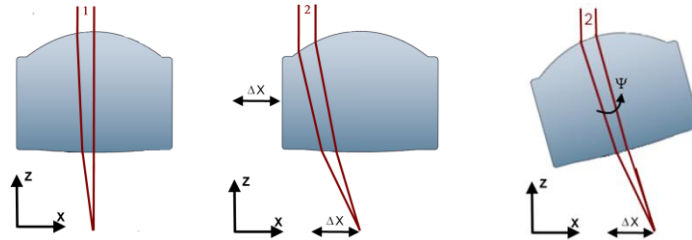


Figure 2.3: Beam steering principles, translation (middle) and rotation (right).

A second method for achieving beam steering is to rotate the lens around its centre of mass (illustrated in figure 2.3 right). Although this is less common due to the fact that it may introduce significant optical aberrations, this second method is potentially attractive from a scanner-head design perspective. With the centre of rotation being at the centre of mass, higher actuation frequencies can be attained, due to the fact that the felt effective mass is less than for the case where the lens is translated in a plane.

## 2.3 Theoretical beam steering model

### 2.3.1 Assumptions

For the calculations geometrical optics was assumed to be valid, implying the following:

- The description of the propagation of light with rays is applicable: i.e. the wavelength of the light is much smaller than the size of optical apertures into which the light wavefront travels (as illustrated in).

Here, the wavelengths of the lasers which were used in the experiments are: a helium neon laser emitting at 633 nm and a femtosecond pulsed laser emitting at 1053 nm. The clear aperture of the aspheric lens selected for this design is 3.70 mm. The ratios aperture/wavelengths are therefore about 6000 and 3500, respectively.

- Light in a given optical medium travels in straight lines, i.e. the materials and volume considered are homogeneous. Here, the lens can be assumed to be homogeneous. The light source which is used in the setup is a laser, it is collimated and monochromatic, which makes the assumption of the light travelling in straight lines valid.
- Diffraction and interference effects are not considered.
- The interface between the sample and the light is not taken into account in the modelling: i.e. the validity of the model is only for surface and near surface machining of the substrate.

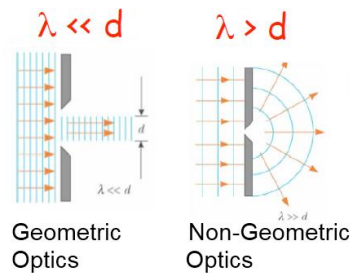


Figure 2.4: Geometric optics, adjusted from [21]. Left and right illustrate the behaviour of light under Geometric and Non-Geometric optics, respectively.

## 2.3.2 Boundary conditions

### 2.3.2.1 The Lens

Based on the current knowledge of the machining process, aspheric lenses were selected for their high numerical aperture performance and quality of the focused spot with limited aberrations. Aspheric lenses are characterized with complex surfaces departing from classical spherical or cylindrical profiles.

The lenses used for the theoretical calculations and experiments in Lausanne and Eindhoven are respectively the 352350-B coated lens, and the 350350-C coated lens sold by Thorlabs and manufactured by Lightpath optics. These lenses differ only in their material, but are comparable in optical specifications. The B and C indicate that they both have a different anti-reflective coating adapted to the laser source used for the experiments. The global dimensions of the lens and its holder can be seen in figure 2.5

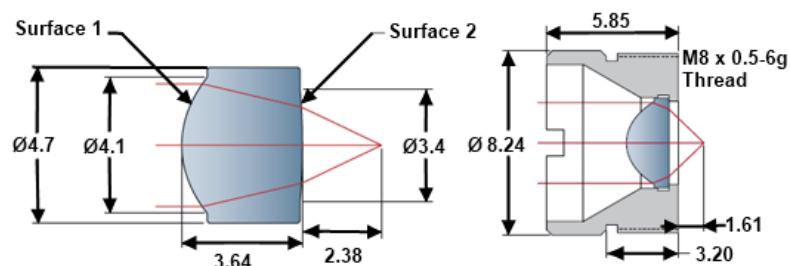


Figure 2.5: Lens (352350, 350350) and holder (M8) dimensions are in mm.

To model the ray tracing, the equations defining the two surfaces are needed. The height profiles of surface 1 and 2 are provided by their lens equations (see equation 2.1 and table 2.2).

$$Z_i = \frac{Y^2}{R_i \left( 1 + \sqrt{1 - (1 + k_i) \left( \frac{Y}{R_i} \right)^2} \right)} + A_{4i}Y^4 + A_{6i}Y^6 + A_{8i}Y^8 \quad 2.1$$

Table 2.2: Lens specifications

Parameter	Definition	i = 1		i = 2
$Z_i$	Sagittal plane height as $f(Y)$ [mm]	-		-
$R_i$	Radius of Curvature [mm]	2.88		-19.14
$k_i$	Conic constant [-]	-1.003315		0
$A_{4i}$	$N^{\text{th}}$ order aspheric constant [ $1/[mm^{N-1}]$ ] (where N is the first index)	$2.1823836 \cdot 10^{-3}$		0
$A_{6i}$		$2.3730881 \cdot 10^{-5}$		0
$A_{8i}$		$-4.5109539 \cdot 10^{-6}$		0
	Used wavelengths, He-Ne, Design wavelength, Femtoprint wavelength	@633nm	@980nm	@1030nm
$n$	Refractive index	1.603	1.593	1.592
$EFL$	Effective Focal Length [mm]	4.43	4.5	4.51

### 2.3.2.2 Laser beams and spot diameters

The laser beams used in this work had two different wavelengths. The femtosecond laser, available in Eindhoven, has a wavelength of 1030 nm. In Lausanne, the experiments were carried out with a He-Ne laser emitting at 632 nm.

Non-linear absorption phenomena are conditioned by the focused intensity. The tighter the focus (i.e. the higher the numerical aperture or NA), the higher the probability to achieve non linear absorption. On the other hand, a too high numerical aperture would limit the maximum depth of machining due to the limited depth of focus. Furthermore, high NA objectives are also more sensitive to optical aberrations if not properly used.

For the machining of all the desired features, a Numerical Aperture (NA) of 0.4 is a good compromise. The selected aspheric lens has an NA of 0.42, but because the beam will be either translating or rotating over the surface this implies that the effectively used NA will be smaller, due to the ingoing effective spot diameter not being the full clear aperture (i.e. the diameter of the accessible surface for an incoming beam on the lens). Equation 2.1 from Hecht [20] gives us the definition of the numerical aperture as a function of the clear aperture (this is further illustrated by figure 2.6).

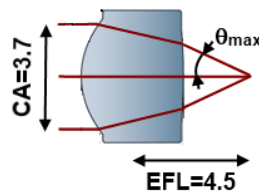


Figure 2.6: Definition of the numerical aperture (NA) for the aspheric lens considers in our experiments (all dimensions in [mm]).

$$NA = n_i \sin(\theta_{max}) \quad \theta_{max} = \text{atan}\left(\frac{CA}{2EFL}\right) \quad NA \approx \frac{CA}{2EFL} \quad 2.2$$

CA= Clear Aperture of the lens in mm.

EFL = Effective Focal Length of the lens in mm.

NA = Numerical Aperture of the lens.

$n_i$  = Refractive index of the immersive medium (air $\approx$ 1).

$\theta_{max}$  = Half angle of maximum cone picked up by the lens.

The effectively used numerical aperture depends on the spot size which enters the lens, which can be defined as the Effective Clear Aperture (ECA). In our case, the desired effective N.A. is 0.4 thus the ECA should be:

$$ECA = 2EFL \tan \left( a \sin \left( \frac{ENA}{n_i} \right) \right) \approx 2EFL ENA = 3.6 \text{ [mm]} \quad 2.3$$

The laser beams considered here have a Gaussian profile (figure 2.7). We define the beam radius at  $2\sigma$ ,  $\sigma$  being the standard deviation for the Gaussian profile.

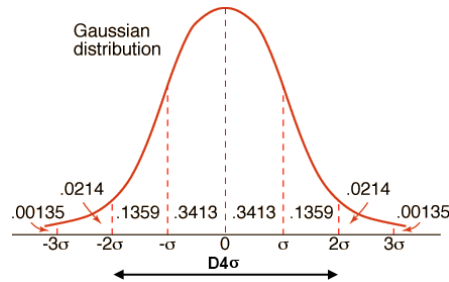


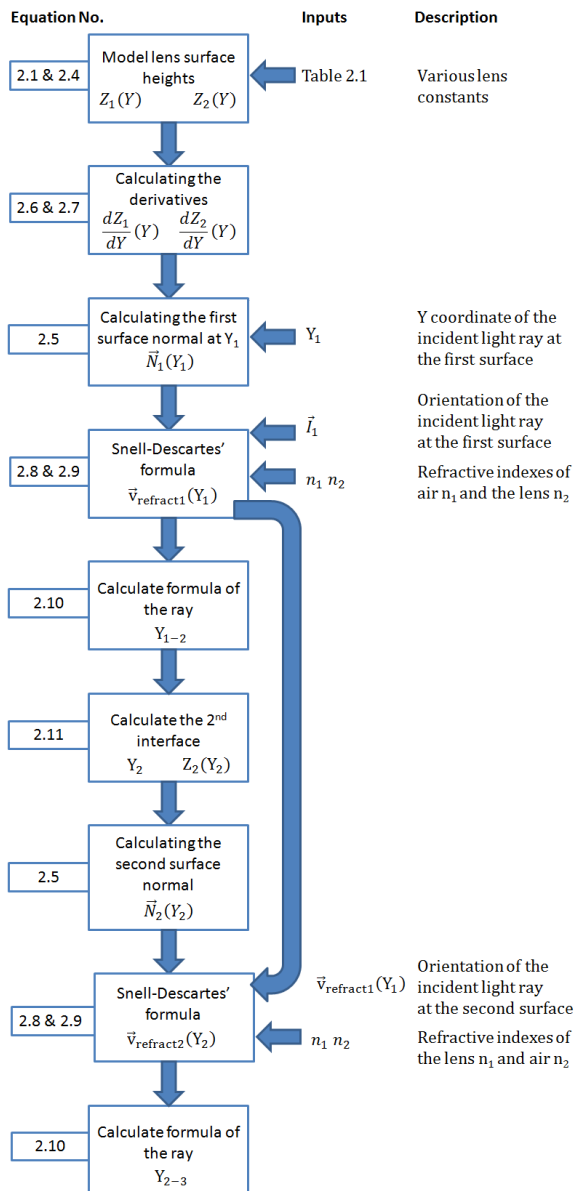
Figure 2.7: 2D Gaussian profile with laser beam diameter definition, adjusted from [20]



### 2.3.3 Ray-tracing methodology

In this thesis two ray-tracing models were derived in Matlab®, we discuss the ray-tracing methodology for these two models. An overview of the entire method for these two models is provided in figure 2.8.

#### Case 1: Translation



#### Case 2: Rotation

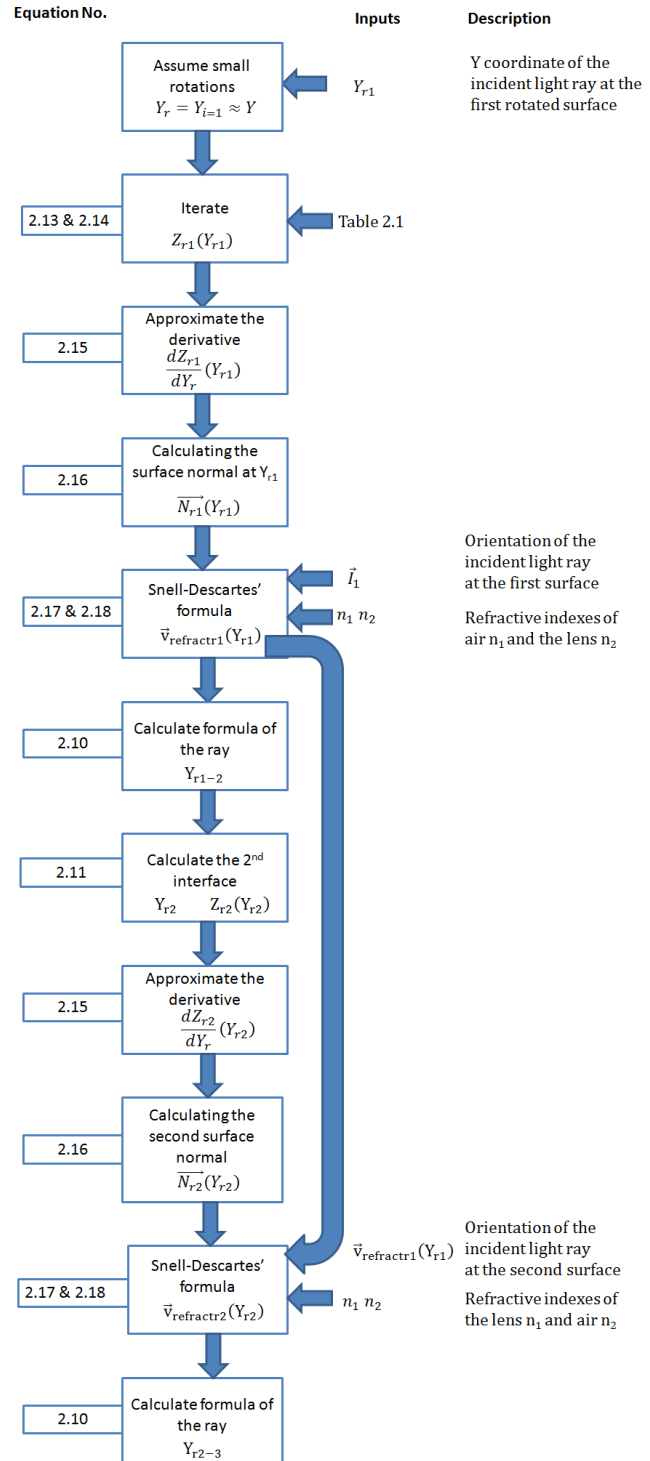


Figure 2.8: Ray-tracing methodology flowchart

**Case 1: Ray-Tracing a translation of the lens in a plane perpendicular to the beam axis.**

The first step of ray-tracing, modelling the lens surfaces in space, was done by combining equations 2.1 and 2.4 and resulted in Figure 2.9.

$$Z_1 = -Z_i + 3.64, \quad Z_2 = -Z_i \quad 2.4$$

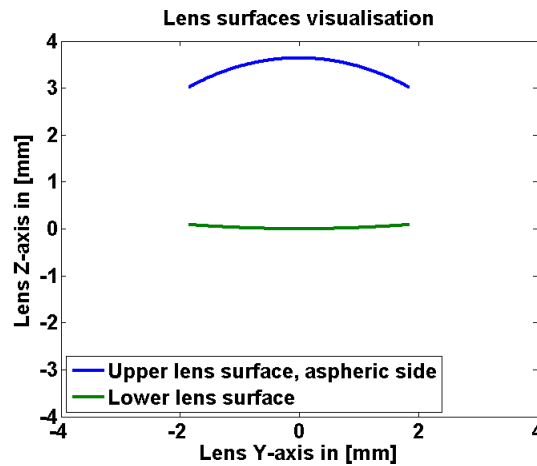


Figure 2.9: The aspheric lens surfaces plotted the Matlab®, the first step in ray-tracing.

The next task is to describe the light beam in space. This can be done by selecting a Y coordinate on the interface between refractive indexes and specifying the orientation of the ray propagation vector (in this case a beam oriented in  $-Z$  direction:  $\vec{T}_1 = \begin{bmatrix} 0 \\ -1 \end{bmatrix}$ ). The next step is to determine the normal vectors ( $\vec{N}$ ) of the surface at the positions where the light beam crosses interfaces. The surface normal unit vector is defined in equation 2.5.

$$\lim_{\Delta Y \rightarrow 0} \vec{N} = \frac{1}{\Delta Z + \Delta Y} \begin{bmatrix} \Delta Z \\ -\Delta Y \end{bmatrix} = \frac{1}{\frac{\Delta Z}{\Delta Y} + 1} \begin{bmatrix} \frac{\Delta Z}{\Delta Y} \\ -1 \end{bmatrix} \rightarrow \vec{N} = \frac{1}{\frac{\partial Z}{\partial Y} + 1} \begin{bmatrix} \frac{\partial Z}{\partial Y} \\ -1 \end{bmatrix}, \quad n_1 = 1, n_2 = 1.603 \quad 2.5$$

The  $\frac{\partial Z}{\partial Y}$  term is the derivative with respect to y of the sagittal height profiles, defined by equations 2.1 and 2.4. By only doing this for nonzero coefficients this result in equations 2.6 & 2.7, describing the derivative of surface 1 and 2 respectively:

$$\frac{dZ_1}{dY} = -\frac{2Y}{R_1 \left( \left( 1 - \frac{Y^2(k_1+1)}{R_1^2} \right)^{\frac{1}{2}} + 1 \right)} - \frac{Y^3(k_1+1)}{R_1^3 \left( \left( 1 - \frac{Y^2(k_1+1)}{R_1^2} \right)^{\frac{1}{2}} + 1 \right)^2 \left( 1 - \frac{Y^2(k_1+1)}{R_1^2} \right)^{\frac{1}{2}}} \dots \quad 2.6$$

$$\dots - 4A_{41}Y^3 - 6A_{61}Y^5 - 8A_{81}Y^7$$

$$\frac{dZ_2}{dY} = -\frac{2Y}{R_2 \left( \left( 1 - \frac{Y^2}{R_2^2} \right)^{\frac{1}{2}} + 1 \right)} - \frac{Y^3}{R_2^3 \left( 1 - \frac{Y^2}{R_2^2} \right)^{\frac{1}{2}} \left( \left( 1 - \frac{Y^2}{R_2^2} \right)^{\frac{1}{2}} + 1 \right)^2} \quad 2.7$$

With the normal vectors defined by equations 2.5, 2.6 and 2.7, the refractive indexes, and the orientation of the incident light beam ( $\vec{I}_1 = \begin{bmatrix} 0 \\ -1 \end{bmatrix}$ ), Snell-Descartes formula, equation 2.9, is applied to the first interface, yielding  $\vec{v}_{\text{refract1}}$ .

$$\cos(\theta_1) = \vec{N}_1 \cdot (-\vec{I}_1) \quad \cos(\theta_2) = \sqrt{1 - \left(\frac{n_1}{n_2}\right)^2 (1 - (\cos(\theta_1))^2)} \quad 2.8$$

$$\begin{aligned} \text{If } \cos(\theta_1) > 0 \quad \vec{v}_{\text{refract1}} &= \left(\frac{n_1}{n_2}\right)\vec{I}_1 + \left(\frac{n_1}{n_2}\cos(\theta_1) - \cos(\theta_2)\right)\vec{N}_1 \\ \text{If } \cos(\theta_1) \leq 0 \quad \vec{v}_{\text{refract1}} &= \left(\frac{n_1}{n_2}\right)\vec{I}_1 + \left(-\frac{n_1}{n_2}\cos(\theta_1) + \cos(\theta_2)\right)\vec{N}_1 \end{aligned} \quad 2.9$$

The vector  $\vec{v}_{\text{refract1}}$  gives the direction of the refracted light beam. Knowing this direction the next step is to find the location where the light beam intersects with the 2<sup>nd</sup> interface. This can be done by rewriting the vector into the equation of a line, starting at the first interface.

$$\vec{v}_{\text{refract1}} = \begin{bmatrix} dy_1 \\ dz_1 \end{bmatrix} \quad b = -\frac{dz_1}{dy_1} Y_1 \rightarrow Y_{1-2} = \frac{dz_1}{dy_1} Y + b \quad 2.10$$

For the light beam the intersection with the second surface can be calculated with the following equation.

$$Y_{1-2} - Z_2 = 0 \quad 2.11$$

This equation results in a  $Y_2$  and  $Z_2(Y_2)$  coordinate on the second surface, which can be used to again apply Snell-Descartes' formula (2.9). From Snell-Descartes' formula  $\vec{v}_{\text{refract2}}$  is determined.

With  $\vec{v}_{\text{refract2}}$  an equation of a line can be written to see the way light progresses through space. By repeating this process for multiple light beams, as illustrated in figure 2.10, the focal plane can be calculated.

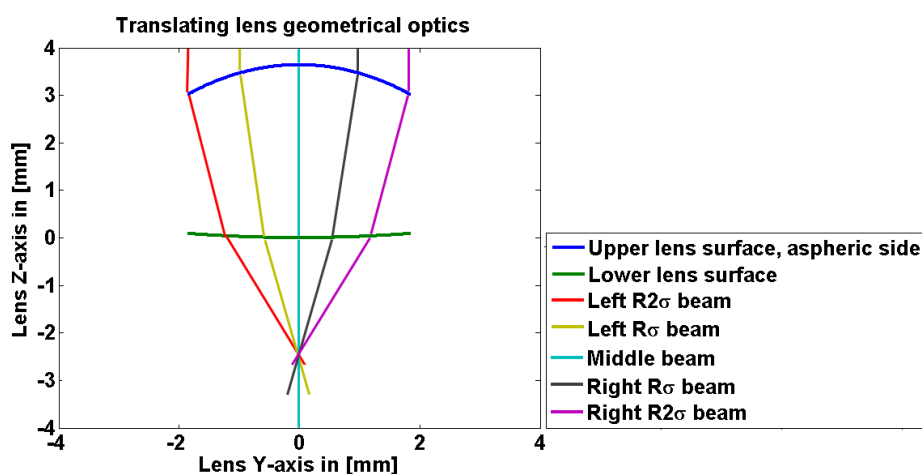


Figure 2.10: Ray tracing in the case of a beam collinear to the lens axis.

## Case 2: Ray-tracing a rotation of the lens with respect to beam axis.

The methodology is somewhat similar as for the previous case. The main difference is that the lens surfaces need to be rotated around a pre-defined rotational centre in space. For these rotated surfaces the respective vectors normal to the surface have to be calculated again.

The known inputs are the orientation of the beam ( $I_1$ ) and the location ( $Y_{r1}$ ) of the first refraction. This location is with respect to the rotated Y position ( $Y_{r1}$ ).

The known formulas are equation 2.12 defining the non-rotated height profile ( $Z$ ) as a function of the non-rotated height( $Y$ ), and equation 2.13 which defines the link between rotated and non-rotated coordinates. Equation 2.12 is a nonlinear function with 8<sup>th</sup> order terms which has to be rewritten into the rotated coordinates to solve it. Directly solving this is a tedious task, therefore the choice was made to solve the problem using Newton-Rhapson iterative method.

The problem consists of three unknowns which are: the original profile height ( $Z(Y)$ ), the rotated profile of the lens ( $Z_{r1}$ ), and the original Y position coordinate on the non-rotated lens ( $Y$ ). The problem is further defined by three equations (2.12, 2.13 & 2.14).

$$Z_{1i} = -\frac{Y_{1i}^2}{R_{1i}\left(1 + \sqrt{1 - (1+k_1)\left(\frac{Y_{1i}}{R_{1i}}\right)^2}\right)} - A_{4i}Y_{1i}^4 - A_{6i}Y_{1i}^6 - A_{8i}Y_{1i}^8 \quad 2.12$$

Assuming small rotations, we pose  $Y_r = Y_{i=1} \approx Y$ , and derive the height profile of the unrotated surface at iteration  $i$  ( $Z_{1i}$ ). With the use of equation 2.13, the new value  $Y_{1i+1}$  of  $Y_{1i}$  can be calculated and will become  $Y_{1i}$  for the next iteration.

$$\begin{bmatrix} Y_{1i+1} \\ Z_{r1i} \end{bmatrix} = \begin{bmatrix} \cos(\alpha) & \sin(\alpha) \\ \tan(\alpha) & \frac{1}{\cos(\alpha)} \end{bmatrix} \begin{bmatrix} Y_{r1} - Rc_y \\ Z_{1i} - Rc_z \end{bmatrix} + \begin{bmatrix} Rc_y \\ Rc_z \end{bmatrix} \quad 2.13$$

With Newton-Rhapson method, we can minimize the error to a given precision, after which the rotated position ( $Y_r, Z_r$ ) is known.

$$Err = |Y_i - Y_{i+1}| \leq 1 \cdot 10^{-8} \quad Z_{r1i} \approx Z_{r1} \quad 2.14$$

By repeating the same procedure for two other Y values located very close to the original  $Y_r \pm \delta Y$ , the normal vectors can be derived with equation 2.15.

$$\frac{dZ_r}{dY_r} \approx \frac{(Z_{r1} + \delta Z) - (Z_{r1} - \delta Z)}{(Y_{r1} + \delta Y) - (Y_{r1} - \delta Y)} = \frac{\delta Z}{\delta Y} \quad 2.15$$

To derive the normal we use the same formula as previously stated for the case of normal incidence:

$$\vec{N}_{r1} = \frac{1}{\left|\frac{dZ_r}{dY_r} + 1\right|} \begin{bmatrix} \frac{dZ_r}{dY_r} \\ -1 \end{bmatrix}, \quad \vec{I}_1 = \begin{bmatrix} 0 \\ -1 \end{bmatrix}, \quad n_1 = 1, \quad n_2 = 1.603 \quad 2.16$$

After which we apply Snell-Descartes' formula to derive  $v_{refract1}$  and write an equation of the laser beam propagating in the glass.

$$\cos(\theta_1) = \vec{N}_{r1} \cdot -\vec{I}_1 \quad \cos(\theta_2) = \sqrt{1 - \left(\frac{n_1}{n_2}\right)^2 (1 - \cos(\theta_1)^2)} \quad 2.17$$

$$\begin{aligned} \text{if } \cos(\theta_1) > 0 &\rightarrow \vec{v}_{refract1} = \left(\frac{n_1}{n_2}\right)\vec{I}_1 + \left(\frac{n_1}{n_2}\cos(\theta_1) - \cos(\theta_2)\right)\vec{N}_{r1} \\ \text{if } \cos(\theta_1) \leq 0 &\rightarrow \vec{v}_{refract1} = \left(\frac{n_1}{n_2}\right)\vec{I}_1 + \left(-\frac{n_1}{n_2}\cos(\theta_1) + \cos(\theta_2)\right)\vec{N}_{r1} \end{aligned} \quad 2.18$$

From this vector, we can express a tangent function that illustrates the movement of the light beam through the glass medium, as illustrated in the equation below:

$$\vec{v}_{refract1} = \left[\frac{dy}{dz}\right] \rightarrow b = Z_i - \frac{dz}{dy}Y_{ri} \rightarrow Y_{r1-2} = \frac{dz}{dy}Y_r + b \quad 2.19$$

Now for the second surface we need to derive the equation of the rotated lens surface with respect to the rotated Y coordinates this could be done with iteration, but because the formula is simpler than the first lens surface a direct analytic solution of  $Z_{r2}(Y_r)$ , as seen in equation 2.20, was derived. The derivation of this formula can be found in appendix 0.

$$\begin{aligned} Z_{r2} = Z_{rc} - R_2\cos(\alpha) - Z_{rc}2\cos(\alpha) - Y_{rc}\sin(\alpha) - \left(\cos(\alpha)(2Y_{rc}(Y_{rc} - Y_r) + \right. \\ \left. \dots \cos(\alpha)(R_2 + Z_{rc})^2) - Z_{rc}(2R_2 + Z_{rc}) + Y_{rc}^2\sin(\alpha)^2 + 2Y_{rc}Y_r - 2Y_{rc}^2 - Y_r^2 + \right. \\ \left. \dots 2\sin(\alpha)(R_2 + Z_{rc})(Y_r - Y_{rc} + Y_{rc}\cos(\alpha))\right)^{\frac{1}{2}} \end{aligned} \quad 2.20$$

Using the formula  $Z_r(Y_r)$  and the formula describing the ray in the glass  $Z_{ray} = \frac{dz}{dy}Y_{ray} + b$ , the intersection is calculated to locate the second interface.

$$Z_r = Z_{ray} \rightarrow Y_{interface2} \rightarrow Z_{interface2} \rightarrow T_2 N_2 \rightarrow v_{refract2} \rightarrow Y_{r2-3} = \frac{dz}{dy}Y_r + b \quad 2.21$$

Using the same method as before, calculating the Z coordinates for two Y coordinates close to the original  $Y_{r2i} \pm \delta Y$  gives the normal vectors. Snell-Descartes' formula can then be applied to calculate  $v_{refract2}$ , which is rewritten into an equation describing the ray. The intersection between this ray and an arbitrary focal plane can then be calculated to illustrate the motion of the beam. An illustrative example of the model is given in figure 2.11.

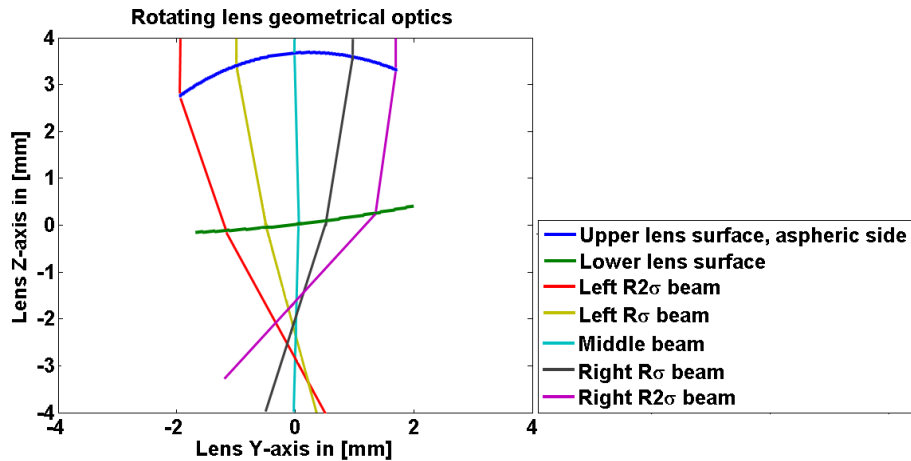


Figure 2.11: A 5 degrees Rotated lens geometrical optics model

### 2.3.4 Model analysis

Using the two ray-tracing models, we can now analyse in details what is happening at the focal plane when the lens is translated or rotated. Our objective is to derive a relation between the amplitude of rotation or translation of the lens and the motion of the spot in its focal plane.

#### Case 1: Ray-Tracing a translation of the lens in a plane perpendicular to the beam axis.

By translating the outer and centre light beam of a focussing spot over the top lens surface, the corresponding spot trajectory can be found.

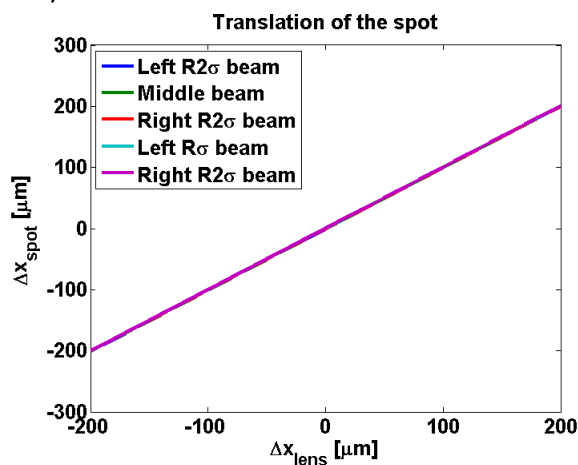


Figure 2.12: spot movement as function of translational input for a beam with D4σ=3.6 mm.

From this plot, we observe that for a given displacement of the lens, the displacement of the spot is roughly the same.

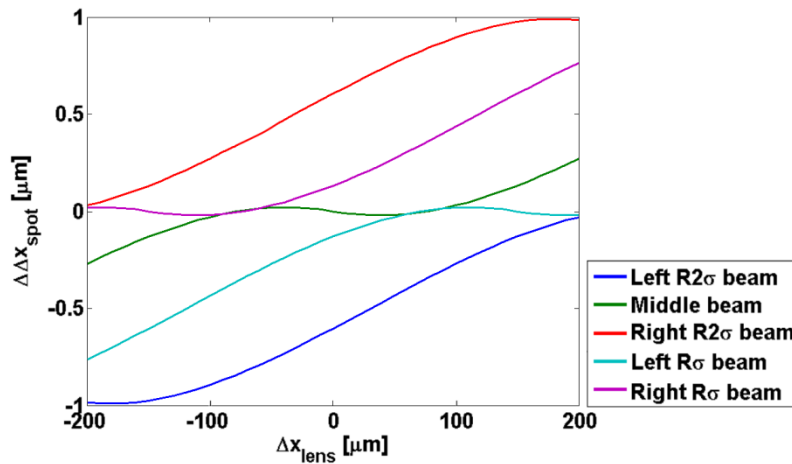


Figure 2.13: Relative displacement of the beam as function of translational input, for a beam with  $D4\sigma=3.6$  mm. the  $R2\sigma$ ,  $R\sigma$  and middle beam are shown, these display only a  $2 \mu\text{m}$  deviation over a  $400 \mu\text{m}$  range.

Figure 2.13 shows the relative displacement of the beam rays.

The main result is that, for a defined radius within the  $-200$  to  $200 \mu\text{m}$  region, a translation induces a small parasitic effect of  $\pm 1 \mu\text{m}$  which is small compared to the laser affected zone (ellipsoidal volume of  $1$  by  $1$  by  $8 \mu\text{m}$ ). This parasitic motion may induce small intensity fluctuations within the LAZ that might be observable during machining.

**Case 2: Ray-tracing a rotation of the lens with respect to beam axis.**

For this case, it is important to pre-define a centre of rotation. We first choose a centre of rotation located at half the lens height in order to have a first idea of the effect of this rotation on the spot translation. The result is shown in the figure below.

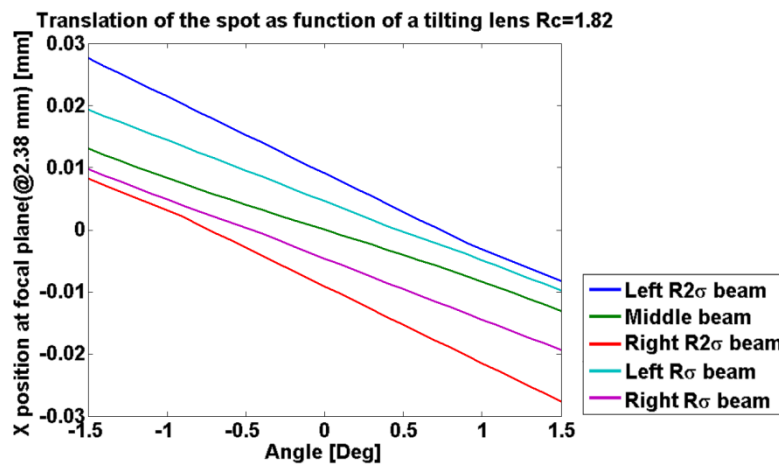


Figure 2.14: Translational displacement as a function of rotated angle, for a beam with  $D4\sigma=3.6$  mm. the total displacement is  $24 \mu\text{m}$  for  $\pm 1.5$  Deg. the aberrations will result in a Gaussian with a slight shift in intensity at the outer rotations.

Although there are some inherent aberrations introduced while translating or rotating the lens, we can see that the spot translates over a distance of  $\pm 12 \mu\text{m}$  for angle variations of  $\pm 1.5$  deg. The translated distance is however not yet sufficient as the desired values are  $\pm 50 \mu\text{m}$ . The same calculations were redone with different centre of rotations. As can be seen in the figure below, the

effect of using different rotational centres influences the relative translation as a function of the angle. In order to allow spot translations of  $\pm 50 \text{ } \mu\text{m}$ , the rotational centre should be about 4.64 mm from the bottom of the lens (figure 2.16)

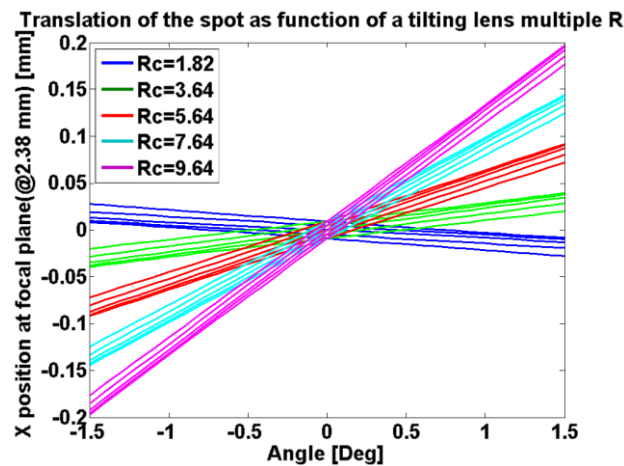


Figure 2.15: Displacement for different rotational centres, with  $D4\sigma=3.6 \text{ mm}$  the 5 lines per rotational lens are the R2 $\sigma$  beams, R $\sigma$  beams and central beam. It can be seen that with increased rotational centre increased displacement is realised.

**Selection of an appropriate centre of rotation**

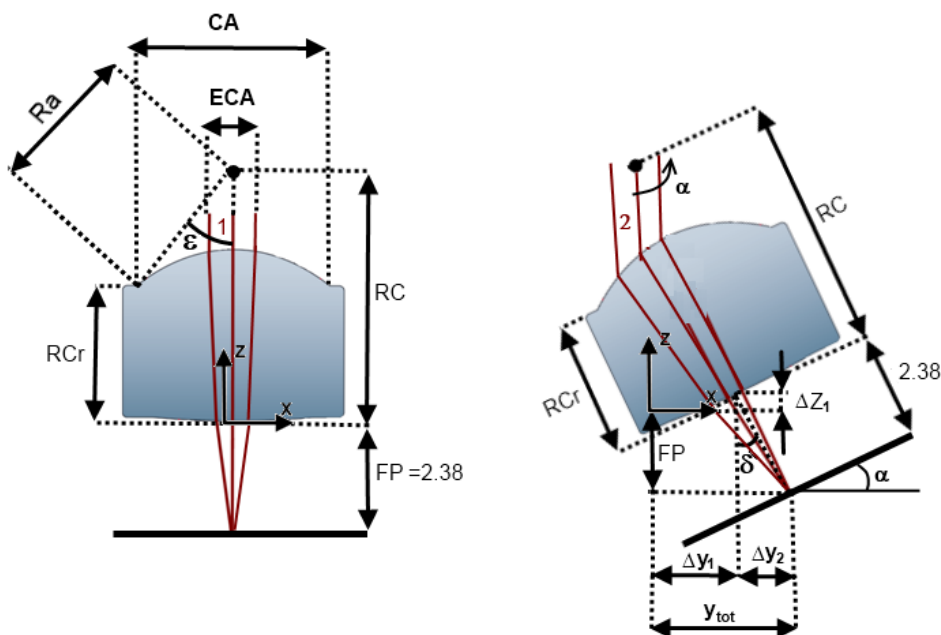


Figure 2.16: The lens and its position in space, a definition of the focal plane and the rotational centre of the lens depending on a tilt ( $\alpha$ ) around RC .

In order to have a better indication for where to allocate rotational centre, an optimisation problem can be formulated, we start of by defining the assumptions and boundary conditions.



*Assumptions and boundary conditions*

We assume that the centre line of the beam that goes through the centre of the non-rotated lens is representative for the focus. Although this is not entirely true, this ray will have the highest intensity near to it and therefore this assumption gives a first order indication.

Condition 1: The ENA of the beam should be at least 0.4 which puts a restriction on the beam diameter ( $D4\sigma$ ) also known as the effective clear Aperture (ECA).

$$D4\sigma = ECA = 2EFL \cdot ENA = 3.6 \quad 2.22$$

EFL= Effective focal length.

Condition 2 &3: the lens is not allowed to translate outside of the effective clear aperture

$$\frac{ECA}{2} - \sin(\epsilon - \alpha_{\text{rad}}) RA \leq 0 \quad 2.23$$

$$\frac{ECA}{2} - \sin(\epsilon + \alpha_{\text{rad}}) RA \leq 0 \quad 2.24$$

Condition 4: the projected surface must always be equal to at least the desired effective clear aperture

$$|\alpha_{\text{rad}}| - \arccos\left(\frac{ECA}{CA}\right) \leq 0 \quad 2.25$$

Condition 5: the angle of the lens is only allowed within the range verified by the experiments

$$|\alpha_{\text{rad}}| - 1.35 \leq 0 \quad 2.26$$

Condition 6: the angle is not allowed to be zero to avoid a rotational centre (RC) which approaches infinity

$$\alpha_{\text{rad}} \neq 0 \quad 2.27$$

Condition 7: the focal plane with respect to the absolute axis is limited by the effective focal length (EFL) of the lens. The deviation in focus should also be bounded.

$$\text{With } \delta = \text{atan}\left(\frac{\Delta y_2}{FP + \Delta z_1}\right), \Delta y_2 = y - RC * \sin(\alpha), \Delta z_1 = RC(1 - \cos(\alpha)) \quad 2.28$$

We get

$$FP\cos(\delta) - 2.38 \leq \pm 1\mu\text{m}, \quad 2.29$$

*Fitting of a spot displacement function*

By repeating the rotational ray-tracing for a wide range of angles (-1.5 to 1.5 Deg), focal planes (2 till 8 mm) and rotational centres (1.82 till 9.82 mm), a simplification of the ray-tracing was made by fitting a function to (equation 2.30) on the data of the central beam.

$$Y = \beta_1\alpha + \beta_2RC + \beta_3FP + \beta_4\alpha RC + \beta_5\alpha FP + \beta_6RC FP + \beta_7 \quad 2.30$$

Y= Displacement of the spot in y due to an angle  $\alpha$ , in mm.

$\beta_i$ = Linear coefficients fitted to the data.

$\alpha$  = Angle of rotation, in Deg.

RC= Rotational centre height in mm with respect to the lowest point of the non-rotated lens.

FP = The focal plane in mm, absolute distance with respect to the lowest point of the lens without applying a rotation

The function of equation 2.30 was simplified using stepwise linear regression as a fitting method to eliminate unimportant parameters, the fitted coefficients were:

$$\beta_1 \approx -3.96 \cdot 10^{-2} \frac{mm}{Deg}; \beta_2 = \beta_3 = \beta_6 = 0; \beta_4 \approx 1.74 \cdot 10^{-2} \frac{1}{Deg}; \beta_5 \approx -2.71 \cdot 10^{-4} \frac{1}{Deg};$$

$$\beta_7 \approx -1.92 \cdot 10^{-6} mm = 0$$

These results for the spot displacement function are not that surprising. The displacement is not a function of just the focal plane or the centre of rotation or a combination of the two. The constant  $\beta_7$  is relatively small (-2 nm) compared to the most dominant coefficient  $\beta_1$  (about  $10^4$  smaller) and is smaller than the root mean square error ( $1.8 \cdot 10^{-4}$ [mm]), implying that though this offset calculated after doing the stepwise linear regression model is negligible and thus zero.

Due to the fact that the coefficients are not dimensionless, the most influential parameters can be found by dividing the absolute total terms over the range.

$$\frac{\beta_4 RC}{|\beta_1|} > 1 \text{ for } Rc > 2.27mm \quad \text{and} \quad \frac{|\beta_5 FP|}{|\beta_1|} > 1 \text{ for } FP > 146mm \quad 2.31$$

Base on equation 2.30 it can be seen that over the most useful part of the entire range (RC>2.27 due to larger spot displacement) the product of the angle and RC is dominant, followed by the angle itself.

The least dominant term, but still important for the root mean square error is coefficient  $\beta_5$ , the product of the angle and Focal plane. The value of a focal plane at 146 mm holds no meaning, because this is far from the actual focus and is far from the data used to fit the equation.

Another interesting result is the root mean square error: RMSE  $\approx 1.8 \cdot 10^{-4}$ [mm]. This implies an error of roughly 200 [nm] made with this formula over the fitted data. The range of interest is of micron level. This RMS error is still a factor 5 below the necessary resolution, thus sufficient for optimization.

## Results

With the previously stated assumptions, boundary conditions and optimisation function an optimisation was done, the results of the optimisation were the following

$\alpha_{\min/\max} = \pm 1.35$ [Deg], $RC \approx 4.91$ [mm], $y_{\text{disp}} \approx \pm 0.061$ [mm], $FP_{\min} \approx 2.38$ [mm]	2.32
--	------

The angles are the maximum investigated angles, and that these were chosen makes sense because a larger angle equals a larger spot displacement. This is also a maximum allowed by Condition 5 (equation 2.26).

The interesting factor is the RC of 4.91 if we compare this with the results from figure 2.15, this value seems about were one should estimate it for the attained range.

The attained spot displacement is  $122$  [ $\mu\text{m}$ ] this is larger than the minimal desired movement range of  $100$  [ $\mu\text{m}$ ]. The focal plane is where one would expect it for the lens which is  $2.38$  mm, this is a result of the previously defined condition 7 (equation 2.29 stating that the deviation in focal plane height should be kept at a minimum).

Besides the results of this optimisation the deviation in Z between the outer displacements was evaluated to be roughly  $-800$  [nm], which is roughly a  $10^{\text{th}}$  of the laser affected zones height (ellipsoid with dimensions 1 by 1 by  $8$   $\mu\text{m}$ ). These parameters seem to supply us with an interesting first option for the centre of rotation in a design.

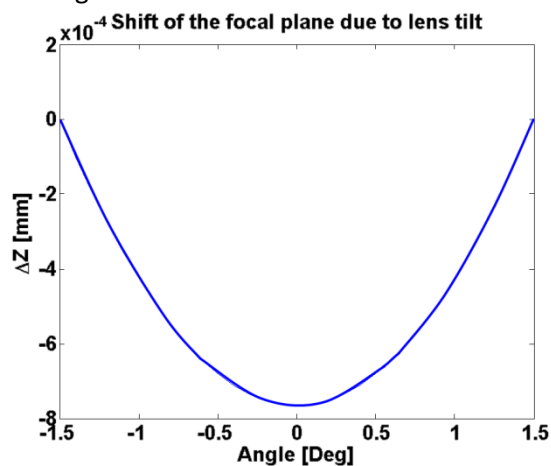


Figure 2.17: The displacement of the focal plane due to lens tilt. One can see that over the entire range there is a variation in focal plane height of about 800 nm.

## 2.4 Beam steering experiments: models validation

### 2.4.1 Experimental setup

To validate the models presented in the previous paragraphs, an experimental setup (shown in figure 2.18) was built.

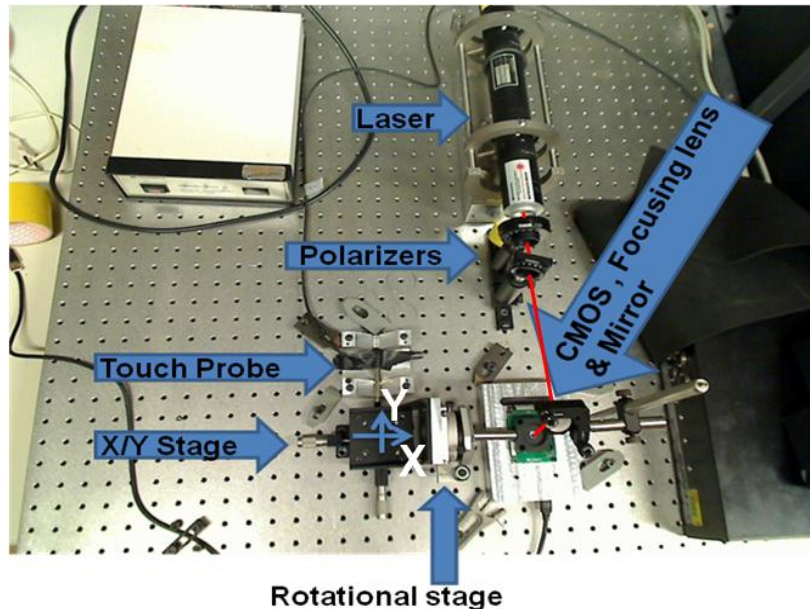


Figure 2.18: Top view of the optical breadboard on which the test setup was mounted. The various components are indicated.

The experimental setup consists of a Helium-Neon laser which intensity is modulated by two polarisers in order to avoid saturation on the CMOS chip. The beam is reflected on a mirror before passing through the aspheric focusing lens. The focused beam is observed on a CMOS chip (resolution: 1600 x 1200 pixels, with pixel size: 4.2 by 4.2  $\mu\text{m}$ ). The lens itself is mounted on a rotational stage itself mounted on a translational stage. A touch probe (Uncertainty 4  $\mu\text{m}$ ) is mounted to directly measure the applied translation and to increase the measurement resolution and accuracy.

### 2.4.2 Measurement method

A CMOS sensor (Luminera) from the camera Lu205L is used to measure the displacement and shape of the focused laser spot. The measurement method consists of taking a picture after adjusting rotating or translating the lens. The laser used for these measurements has a wavelength of 633 nm and a high quality circular beam profile. To reduce the signal noise, only the red component from the colour CMOS sensor was used.

The spectral response of the camera is shown in figure 2.19,

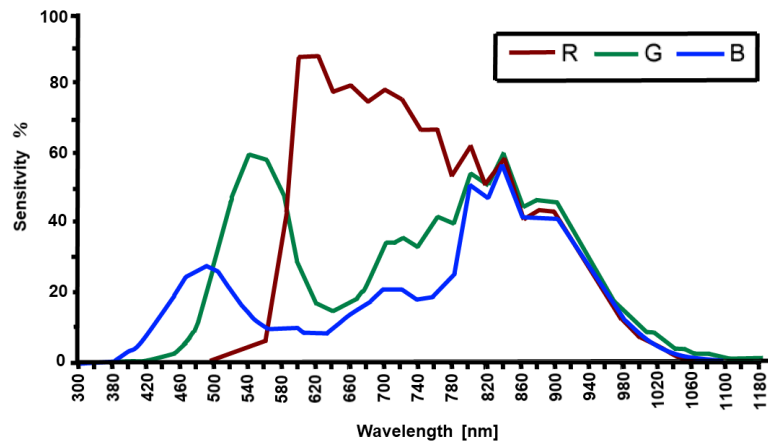


Figure 2.19: CMOS RGB spectral response adjusted from [22] . We used only the red component to reduce the noise.

After acquiring the red signal and avoiding saturation of the sensor by tuning the laser beam cross-polarizers, the X and Y data is adjusted from pixels to real values and plotted in three dimensions.

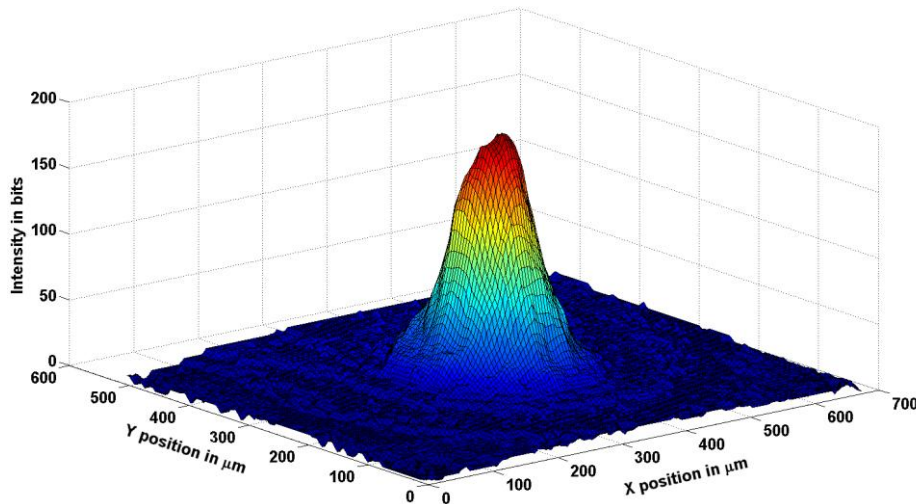


Figure 2.20: Measurement of a Gaussian spot profile, depicting its position on a part of the CMOS in  $\mu\text{m}$ .

Using the collected data, a two-dimensional Gaussian surface fit is made using equation 2.33.

$$Z = Ae^{\left(\frac{(x-x_0)^2}{2\sigma_x^2} + \frac{(y-y_0)^2}{2\sigma_y^2}\right)} \quad 2.33$$

A= The maximum value of the Gaussian in bits.

x= Active x variable  $\mu\text{m}$ .

$x_0$  = Zero x position of the centre of the Gaussian spot  $\mu\text{m}$ .

y= Active y variable in  $\mu\text{m}$ .

$y_0$ = Zero y position of the centre of the Gaussian spot [ $\mu\text{m}$ ]

$\sigma_x$  = Standard deviation of the Gaussian spot in x direction [ $\mu\text{m}$ ]

$\sigma_y$  = Standard deviation of the Gaussian spot in y direction [ $\mu\text{m}$ ]

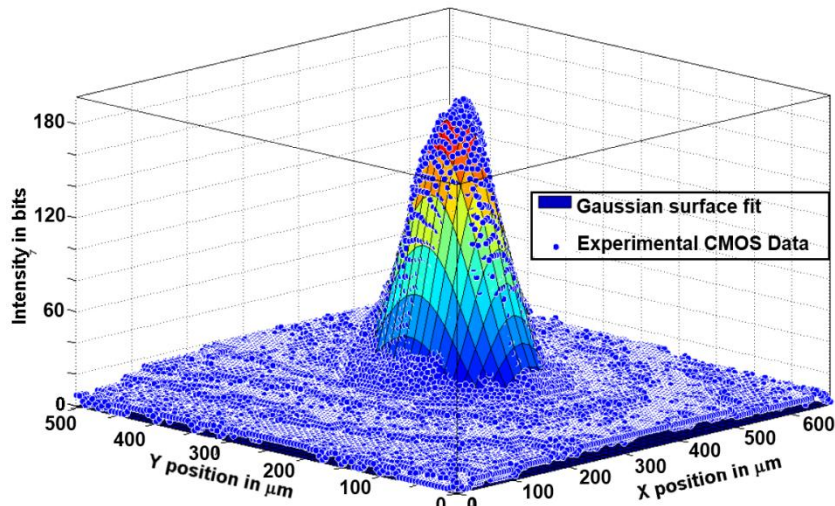


Figure 2.21: Gaussian surface fit

The residuals are analysed as in figure 2.22. The  $R^2$  adjusted (defined in the next paragraph) is also used to assess the quality of the fit.

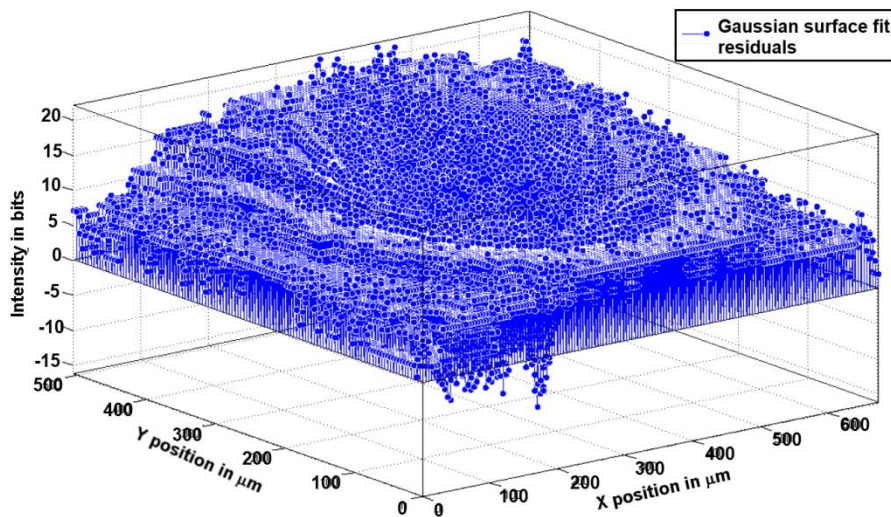


Figure 2.22: The residuals of the plot

The  $R_{adj}^2$  is a normalized metric of the quality of a fit, ranging from 0 (no fit) to 1 (best fit). It is defined according equation 2.34.

$$R_{adj}^2 = 1 - \frac{\frac{SS_e}{n-p}}{\frac{SS_T}{n-1}} \quad \text{with} \quad SS_T = \sum_i (y_i - \bar{y})^2 \quad SS_e = \sum_i (y_i - f_i)^2 \quad 2.34$$

$SS_e$  = The residual sum of squares.

$SS_T$  = The sum of squares.

$n$  = Total number of measured points.

$p$  = Total number of regressor variables which are in this case (equation 2.33)  $x$  and  $y$ .

$y_i$  = Measured value at point  $i$ .

$\bar{y}$  = The mean value of all measured  $y$  values.

$f_i$  = Fitted value evaluated at point  $i$ .

For a more detailed definition and discussions about these fit quality metrics, the reader is referred to [23], [24] & [25].

### 2.4.3 Measurement analysis

To test the measurement procedure, the tests are first performed with a lower effective numerical aperture (0.091) and higher effective numerical aperture (0.362). This was done, to show the effects related to different effective numerical apertures.

For a given lens position, each measurement was repeated multiple times (typically four times) to take into account possible laser power fluctuations and to test the repeatability of the procedure.

#### Lens translation

The complete dataset, discussed in this section, can be found in appendices D.1 & D.2.

Figure 2.23 shows the spot displacement after moving the stage in one direction, going back and forth. A hysteresis attributed to the friction between the ball bearings and the moving part of the stage is observed. This is visible especially in, the 2<sup>nd</sup> and 4<sup>th</sup> measurement sets show a parasitic displacement along the x-direction ranging from +1.5  $\mu\text{m}$  for low NA and up to 4  $\mu\text{m}$  for higher NA.

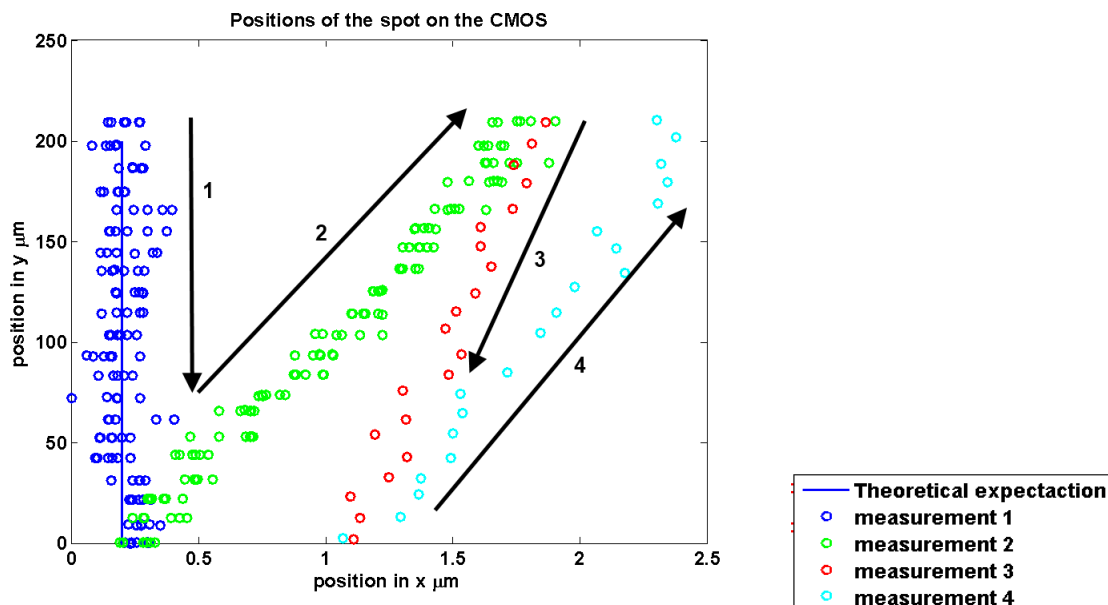


Figure 2.23: The translational tests, the test consisted of four consecutive measurements (indicated by direction and measurement no. in the figure), of which the first two took 6 measurements per interval. From this figure one can see that an applied displacement of 200  $\mu\text{m}$  to the lens roughly equals the expected translation of 200  $\mu\text{m}$  of the spot.

For both NAs, the results show that the applied translation roughly equals the measured translation. (The translation occurring at the CMOS is about 10  $\mu\text{m}$  more than expected for a low NA while for the higher NA, this effect is almost unnoticeable and limited to about 1-2  $\mu\text{m}$ . The author expects that these inaccuracies are mainly attributed to summed up uncertainties of the individual steps, the difference itself is most likely attributed to relatively large difference in spot sizes which means with a smaller spot there are less points of measurement on the CMOS so the uncertainty becomes larger).

While the prescribed displacements were 10  $\mu\text{m}$ , deviations of up to 4  $\mu\text{m}$  are measured. If we subtract these deviations from the measured displacement on the touch probe, the uncertainties become  $\pm 2 \mu\text{m}$  for both NAs, which equals the uncertainty of the touch probe. Therefore, within the limits of our experimental setup, the prescribed displacement is equal to the measured one.

The displacements in the X-direction are even smaller ( $\pm 0.3 \mu\text{m}$  for the lower NA and  $\pm 4 \mu\text{m}$  for larger NA). All displacements in x are related to imperfections in the y-translation axis and the alignment of the motion axis with the CMOS axis. Furthermore, the x axis is not measured with a touch-probe; the movement along this axis is therefore not verified.

The standard deviations of the Gaussians fit over a  $200 \mu\text{m}$  movement range are:  $\sigma_x = 11.5$  up to  $13.5 [\mu\text{m}]$  and  $\sigma_y = 12$  upto  $14.25 [\mu\text{m}]$  for a low NA. For higher NA, these values become:  $\sigma_x = 113$  to  $110 [\mu\text{m}]$  and  $\sigma_y = 114$  to  $108 [\mu\text{m}]$ . The large difference of low NA and high NA spot size is most likely caused, by a combination of imperfect alignment of the focal plane with the CMOS sensor and using a larger NA itself causing more aberrations. The absolute variation of the radii is in the same order of magnitude.

The ratio  $\frac{\sigma_x}{\sigma_y}$  ranges from 0.97 to 0.95 for low NA and from 0.99 to 1.04 for high NA. This implies that the Gaussian is slightly ellipsoidal.

Finally, the quality of the fit itself was examined for the lower NA:  $R_{adj}^2$  ranged from 0.97 down to 0.89 while for the larger NA, the  $R_{adj}^2$  ranged 0.92 to 0.95. This implies that over the measured displacement range, the beam stayed Gaussian (within the specified acceptable deviations). Larger deviations were noticed at the end of the motion range. This result is not surprising as one would expect more aberrations as the beam is moved further away from the lens central axis.

### Lens rotation

As for the lens translation, the complete data sets discussed in this section can be found in appendices D.3 & D.4.

From the small NA tests, we observe that the axis of rotation is not aligned with the Y axis of the CMOS sensor itself. The measured displacement in Y is around  $180 \mu\text{m}$  while the displacement in x is about  $9 [\mu\text{m}]$ . With a larger NA, the relative X displacement remains very small ( $7 \mu\text{m}$  over a  $160 \mu\text{m}$ -Y-motion range).

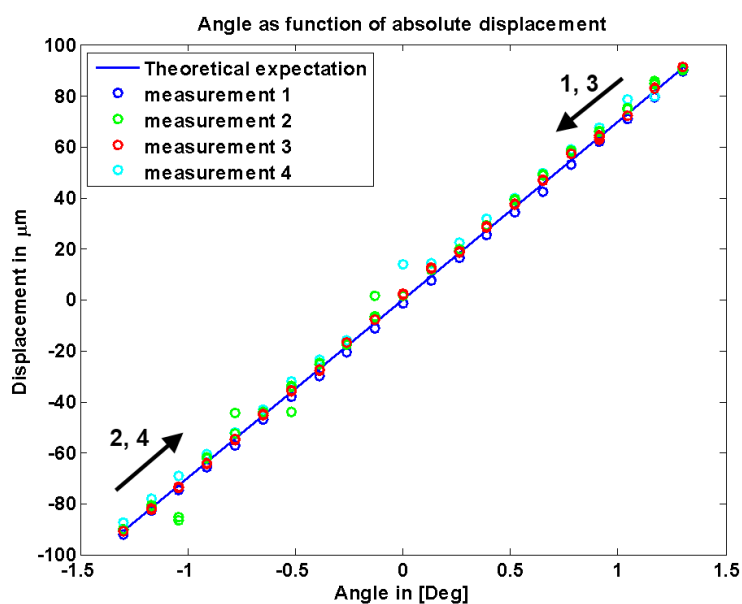


Figure 2.24: Displacement as a function of the angular rotation.



After converting the measured displacement into an angle, we observe a good agreement between the theoretical expectations the measured ones. For the low NA the total range motion is +/- 90  $\mu\text{m}$  while for high NA it is +/-70  $\mu\text{m}$ . This is respectively +/-20 and +/-9  $\mu\text{m}$  more than the maximum +/-61  $\mu\text{m}$  expected with the constrained optimisation (equation 2.32) implying that the rotational centres are estimated at 6.13 and 5.28 mm, respectively. The difference in rotational centre and can be explained by the fact that the setup was remounted in between the two series of experiments. The position of the centre of rotation may have slightly changed. It should also be noted that with the setup accurate positioning of the RC was quite tedious, and having this better defined with respect to the lens is a recommendation for if ever a future measurement setup.

The relative displacements per angular interval is on average 9  $\mu\text{m}$  for the low NA and 7  $\mu\text{m}$  for the large NA.

The standard deviations of the Gaussian fit are ranging between  $\sigma_x = 13.4$  and  $\sigma_y = 15$  to  $\sigma_x = 14.6$  and  $\sigma_y = 15$  for the low NA. For the high NA, we found  $\sigma_x$  between 112 and 114  $\mu\text{m}$ , and  $\sigma_y$  between 110 and 114  $\mu\text{m}$ .

The ellipsoidicity over the range motion for the low NA  $\frac{\sigma_x}{\sigma_y}$  ranges from 0.93 to 0.98. For the high NA, it ranges from 1.03 to 1.

The  $R_{adj}^2$  ranged from 0.99 to 0.95 for the low NA. For the High NA,  $R_{adj}^2$  ranges from 0.94 down to 0.93.

## 2.5 Conclusion on beam steering methods

In conclusion, we demonstrated that both rotation and translation are feasible over investigated motion ranges.

The ellipsoidicity (ratio of the standard deviations) is distorted slightly more by rotation than translation, but remains acceptable within the investigated ranges of +/- 70  $\mu\text{m}$ .

The choice was made to further investigate suspensions that produce rotation. The rationale for this decision is that we expected to obtain higher dynamics with such suspensions and therefore, an overall higher bandwidth for the system.



## **Chapter 3    Scanning head design**

---

This chapter considers the scanning head design per se, from an optomechatronics perspective. The chapter starts with the conceptual design of the suspension, followed by the implementation of the selected kinematics concept. Suitable actuators and sensors are also investigated and a final choice for the overall design implementation is proposed.

### 3.1 Selected kinematics

Various kinematics inspired the selection process some of the notable ones are [26], [27], [28] and [29].

From our study on optimal methods for beam steering, we have selected the scanning concept where the lens is rotated. This choice is motivated by the potentially higher achievable performances. Five kinematics variants to rotate the lens were studied. In this chapter, for conciseness, we only discuss the selected concept. The alternative variants can be found in annex 0.

The final kinematics consists of a suspension that prevent the lens and its mounting body of moving along the coordinates X and Y, and of rotating around the axis Rz.

The three degrees of freedom of the lens, let free by the suspension (Z, Ry and Rx) are actuated.

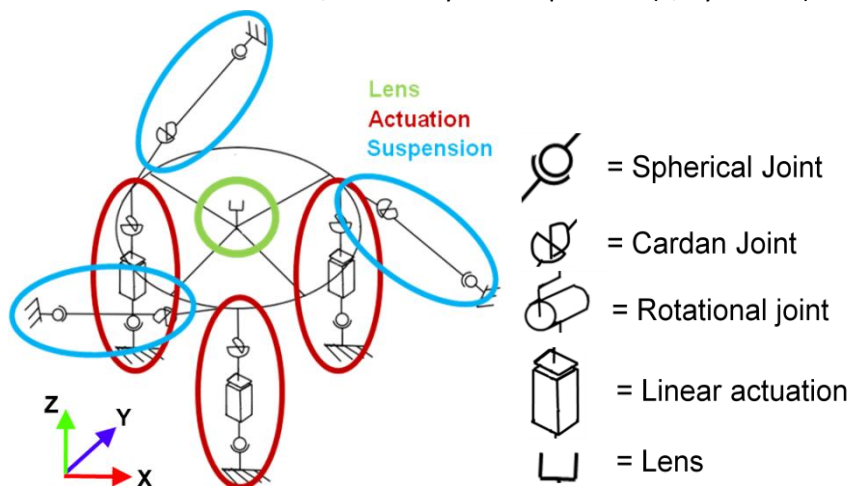


Figure 3.1: Parallel 3xZ structure, consisting of a suspension, actuation and lens.

This concept was selected for its simplicity, its symmetry and the parallel stiffness chains that result in a relatively low-mass high stiffness suspension (for the non actuated axis). Attainable control frequencies are generally proportional to the stiffness and the inverse of the mass, such a design seems to be the best choice among the various investigated solutions to attain high control frequencies.

#### 3.1.1 Mobility analysis

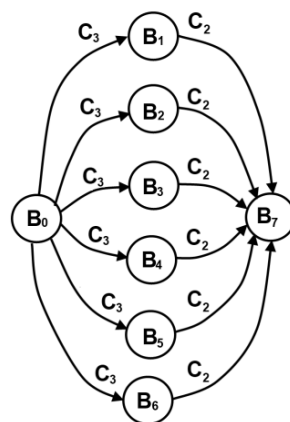


Figure 3.2: Graph representation of the mechanism. The B0 till B7 indicate the identifiable bodies, where B0 is the fixed world and B7 is the lens and its clamp. The C3 and C2s indicate the respective joints of the mechanism, where the number indicates the degrees of freedom of the joint.

The mobility of the mechanism (that includes both the suspension and the actuator) is analysed using the Chebyshev-Grübler-Kutzbach formula [30] [31].

$$m = \sum_{i=1}^6 n_i C_i - 6(N_L - N_B + 1) \rightarrow m = 12 + 18 - 6(12 - 8 + 1) = 0 \quad 3.1$$

$m$ = mobility of the mechanism

$n_i$ = the number of joints of class  $C_i$

$C_i$ = the number of links of

$N_L$ =the number of links

$N_B$ =the number of bodies

The mobility of this mechanism is zero indicated that the mechanism is fully defined and has no non-actuated or over-constrained degree of freedom.

## 3.2 Design realisation: miniature laser scanning head suspension

It was chosen to implement the 3xZ kinematics (as displayed in figure 3.1) by using three folded leaf springs (figure 3.3). The lens will be glued into a lens clamp connected to the three folded leaf springs. During the design the author was inspired by designs and principles mentioned in [30], [32],[33] & [34].

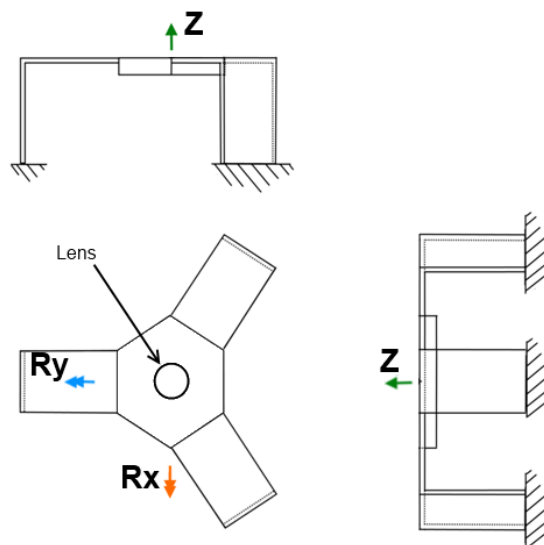


Figure 3.3: The folded leaf spring concept, the degrees of freedom  $\phi$  rotation around x,  $\psi$  the rotation around y and z are indicated.

The advantage of using three folded leaf springs is that the design is not over-constrained and has a linear stiffness over its range.

The folded leaf-springs can be made in different ways. To reduce the design options, we aimed for a cylindrical working volume (with a radius of  $60 \mu\text{m}$  (2.32) and z displacement of  $\pm 50 \mu\text{m}$ ) and for the highest possible control bandwidth.

The goal was to realise non-actuated eigenfrequencies as high as possible and have sufficiently stiff actuators (as explained in the next paragraph), to achieve a high control bandwidth (400 Hz). The aims for the suspension itself are summarised in equation 3.2.

$$\frac{F_{act}}{K_{z_}} \geq 50[\mu m] \quad \frac{M_{actx\_max}}{K_{Rx}} \geq 60[\mu m] \quad \frac{M_{acty\_max}}{K_{Ry}} \geq 60[\mu m] \quad f_{1suspension} \approx 1600[Hz] \quad 3.2$$

### FEM details

A significant part of the design was analysed with COMSOL 4.1. Within the solid mechanics module the eigenfrequency and linear stationary solver were used. The applied mesh consisted of free tetrahedral elements. The meshing itself was physics controlled resulting in significantly more elements in the thickness and length of the leaf spring. More details regarding Comsol in general, the operation of these solvers and the used elementtype can be found in the Comsol manual [35].

The applied boundary conditions for these calculations (except where otherwise indicated) are that the folded leaf springs were assumed fixed with respect to their frame (as in figure 3.3).

The actual mass which was modelled in the setup is:

$$m_{total} = 3m_{coil} + m_{lens} + m_{clamp} + 3m_{leafspring} = 2.73 + 0.21 + 5.4 + 0.97 = 9.31[g] \quad 3.3$$

The clamps density which was made of aluminium was deliberately overestimated to have a simplified model which takes into account the mass of the bolts used in the final design, and provide a safety margin to achieve the desired eigenfrequencies.

### Decoupling between suspension and actuation

The reason for desiring sufficiently stiff actuators is related to the actuated eigenfrequencies, of the system. Their frequency depends on the stiffness of the actuators and thus with actuators which are not sufficiently stiff ( $<10^6$ ) will be a limiting factor (as can be seen in figure 3.4).

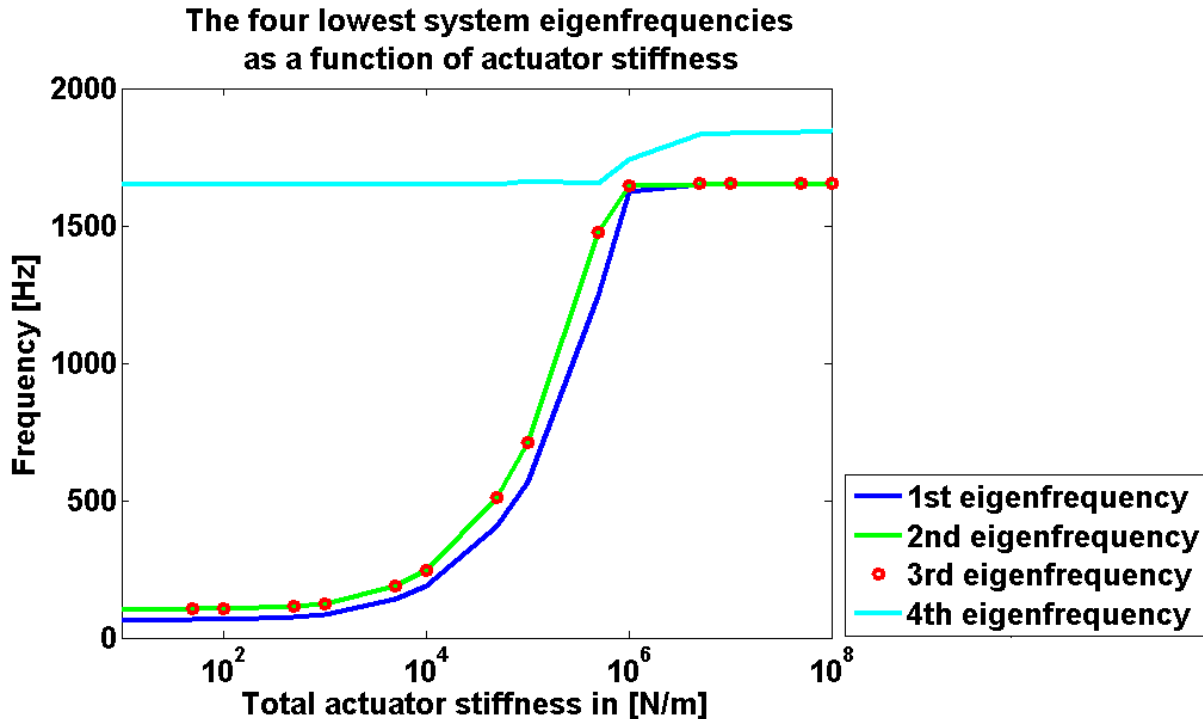


Figure 3.4: actuator stiffness effects on the eigenfrequency of a system, it can be seen that the system will be limited in performance for actuation stiffness lower than  $10^6$

With sufficient stiffness, the non-actuated eigenfrequencies become the lowest eigenfrequencies of the system; this is further indicated by looking at the mode shapes at the frequencies as in table 3.1. What can be seen in this table is that for  $K_{act} < 10^5$  the three lowest eigenfrequencies belong to the principle modes (Z, Rx, Ry) of the system.

As the actuation stiffness increases to  $K_{act} = 5 \cdot 10^5$  we see the first three mode shapes become a combination of higher order modes and the principal modes. Increasing the actuator stiffness to  $K_{act} = 10^6$  results in the non-actuated modes becoming the three lowest eigenfrequencies.

When increasing the actuator stiffness  $K_{act} > 10^6$  even further results in the Z mode having the highest of the three lowest frequencies (due to the lens and its clamp which can almost be considered fixed). As for the 4<sup>th</sup> modes shown with  $K_{act} = 10^6$  and  $K_{act} > 10^6$  these are related to the X, Y and Rz stiffnesses combined with torsional modes of the leaf spring. Indicating that the actuated eigenfrequencies have become higher than the stiffness of the suspension itself.

Table 3.1: Lowest 4 system modes as a function of the actuator stiffness.

	Total actuator stiffness N/m			
	$<10^5$	$5 \times 10^5$	$10^6$	$> 10^6$
1st mode				
2nd mode				
3rd mode				
4th mode				

### 3.2.1 Dimensioning of the folded leaf springs

With the simplification the folded leaf spring was first optimised as a fixed-fixed folded leaf spring taking into account tapers, widths differences in bottom and top length, height and diameter.

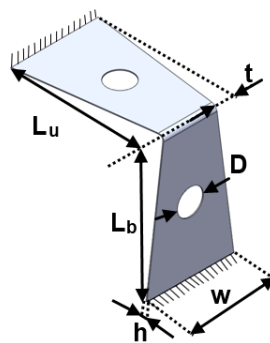


Figure 3.5: Leaf spring, and the parameters in the frequency optimisation.

Although various materials were considered, due to limited availability, a leaf spring steel (1.4310) (from Hasberg [36]), with thickness 0.1 mm was chosen.



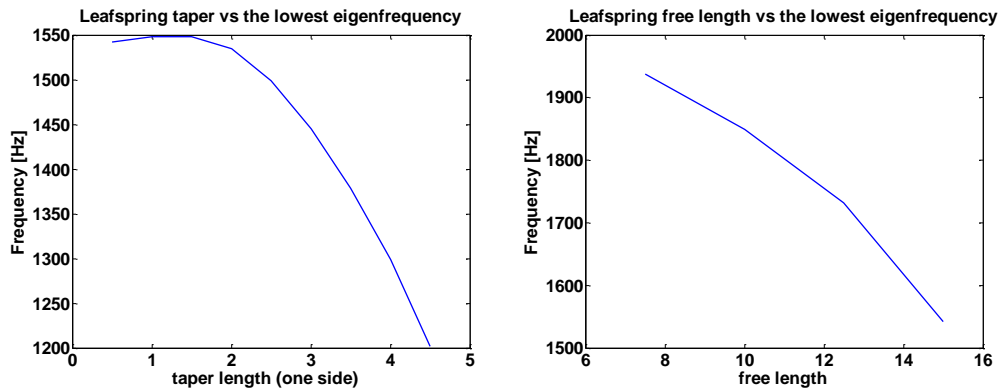


Figure 3.6: left: the effect of the taper ( $t$ ) on the eigenfrequency, showing an optimum around 1.5 [mm] right: the effect of the free length ( $L_u$ ) on the frequency, the shorter the free length the higher the frequency. Dimensions in mm

For the results seen in figure 3.6, we can see is that there is an optimum taper around 1.5 [mm], the reason for this is that basically the mass reduction outweighs the stiffness reduction, however going Past this optimum results in weakening the leaf springs other stiffnesses ( $X$ ,  $Y$  and  $R_z$ ), which then will result in them becoming the lower eigenfrequencies. An additional purpose for the taper is to allow for better alignment of the fold during the fabrication.

As for the free length as one would expect the longer the length the lower the eigenfrequency this is related to it being proportional to the stiffness. This length is especially important for the stiffness in the  $Z$  direction of the mechanism, thus should not be too short as to allow the desired strokes and not cause too high internal stresses.

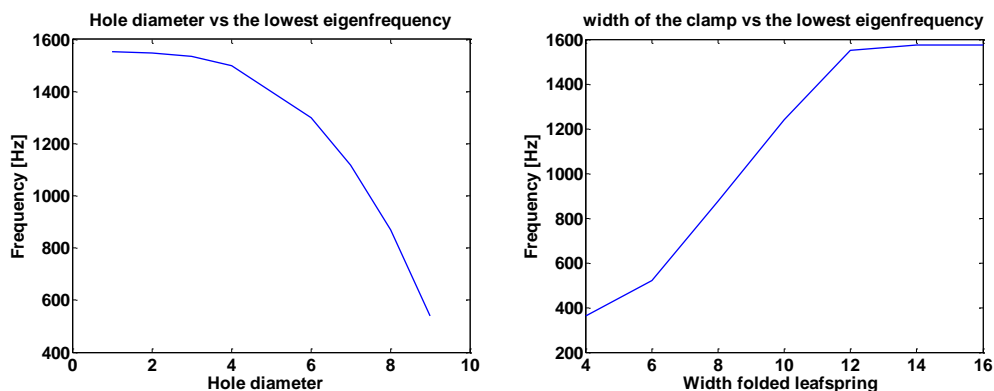


Figure 3.7 left: the effect of adding a hole (with diameter  $D$ ) on the eigenfrequency, showing that adding a hole only reduces the eigenfrequency. Right: the effect of the width of the folded leaf spring ( $W$ ) on the frequency, typically we see that widening the folded leaf spring is only useful to a certain limit. Dimensions in mm

In figure 3.7, we see that adding a hole does not add to the eigenfrequencies, apparently the mass reduction achieved by adding the hole does not compensate for the stiffness loss.

The width of the leaf spring was limited by the compromise of having an as small as possible mass of the lens clamp, while still achieving sufficient stiffness to have high enough eigenfrequencies.

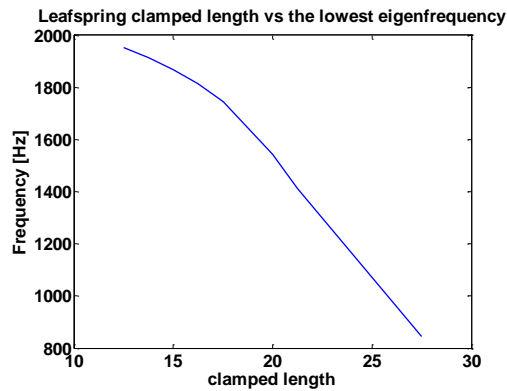


Figure 3.8: The effect of changing the clamped length of the leaf spring. Increasing the length significantly reduces the lowest eigenfrequency of the system. Dimensions in mm

As expected making the leaf springs clamped length longer significantly reduces the eigenfrequency of the system. The clamped length of the folded leaf spring serves mainly to keep linear stiffness over the range and have sufficient shear stiffnesses to reduce the lower modes.

Based on the effects of dimensioning the folded leaf spring on the eigenfrequency a design (equation 3.4) was selected to further investigate for feasibility.

$L_b = 15 \text{ mm}, L_u = 15 \text{ mm}, t = 1.5 \text{ mm}, W = 12 \text{ mm}, \text{thickness} = 3, D = 0 \text{ (no hole) and } f_1 > 1650 \text{ [Hz]}.$	3.4
--	-----

### 3.2.2 Eigenfrequencies

The first six low frequency modes for the system are shown in table 3.2. The design objective is to have the non-actuated eigenfrequencies as high as possible so that the system can be driven at high frequencies without exciting the resonant frequencies of the non-actuated modes.

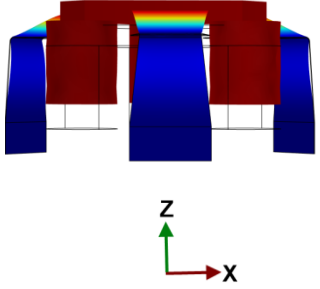
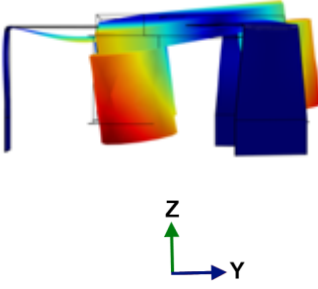
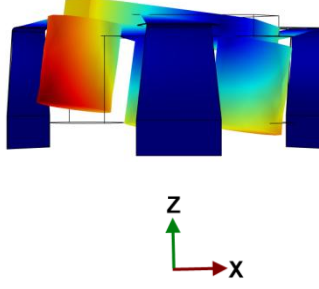
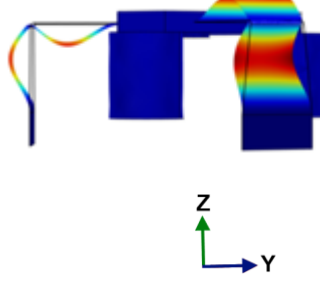
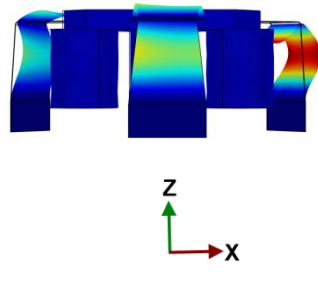
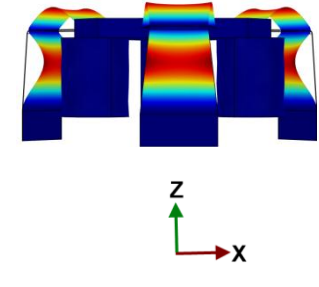
<p><b>1<sup>st</sup> mode Z</b></p>  <p><math>f_1 = 64.76 [Hz]</math></p>	<p><b>2<sup>nd</sup> mode Rx</b></p>  <p><math>f_2 = 103.85 [Hz]</math></p>	<p><b>3<sup>rd</sup> mode Ry</b></p>  <p><math>f_3 = 103.90 [Hz]</math></p>
<p><b>4<sup>th</sup> mode torsional folded leaf spring mode</b></p>  <p><math>f_4 = 1652 [Hz]</math></p>	<p><b>5<sup>th</sup> mode torsional folded leaf spring mode 2</b></p>  <p><math>f_5 = 1652 [Hz]</math></p>	<p><b>6<sup>th</sup> mode bending Folded leaf spring mode</b></p>  <p><math>f_6 = 1660 [Hz]</math></p>

Table 3.2: First six eigenfrequencies of the system.

The first mode ( $f_1 = 64.76 [Hz]$ ) is clearly the Z mode of the system, this would also be expected as the translational mass is larger than the systems inertia. The 2<sup>nd</sup> ( $f_2 = 103.85 [Hz]$ ) and 3<sup>rd</sup> mode ( $f_3 = 103.9 [Hz]$ ), are two rotational modes perpendicular to each other Rx and Ry.

The 4<sup>th</sup> ( $f_1 = 1652 [Hz]$ ) and 5<sup>th</sup> mode ( $f_1 = 1652 [Hz]$ ) are most likely torsional modes of the folded leaf springs. The 4<sup>th</sup> mode shows two folded leaf springs vibrating in opposite direction while the third one stands still. The 5<sup>th</sup> mode shows two folded leaf springs vibrating in the same manner whilst the third vibrates in opposite direction with larger amplitude. The 6<sup>th</sup> mode ( $f_1 = 1660 [Hz]$ ) shows three folded leaf springs vibrating with same direction and amplitude, therefore this is most likely the bending mode of these folded leaf springs.

### 3.2.3 Stiffness

#### Analytic stiffness calculation

In order to model the system, an analytic stiffness model was made using the methodology mentioned in [30]. Besides having the necessary FEM calculations, an analytic model can supply the designer with a fast tool for redesigning the suspension.

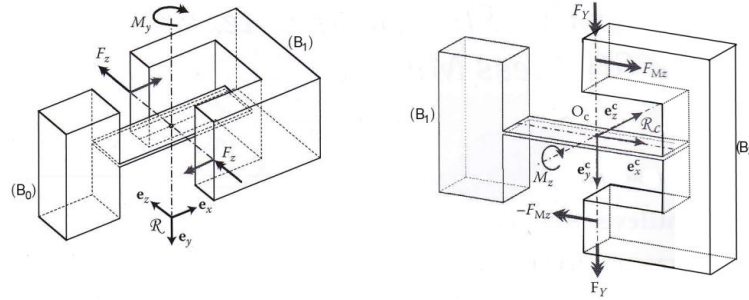


Figure 3.9: The definition of the axis of an individual leaf spring, image taken from [30],

To calculate the stiffness of a folded leaf spring combination as shown in figure 3.10. The stiffness matrix of an individual leaf spring (equation 3.5) is used, with the coordinates as defined in figure 3.9.

$$K_l = \begin{bmatrix} K_{F_x, d r x} & & & & & & \\ & K_{F_y, d r y} & & & & & \\ & & K_{F_z, d r z} & & & & \\ & & & K_{M_x, d \theta_x} & & & \\ & & & & K_{M_y, d \theta_y} & & \\ & & & & & K_{M_z, d \theta_z} & \\ & & & & & & \end{bmatrix} \quad 3.5$$

The components of the stiffness matrix are defined as in equation 3.6.

$$K_{F_x, d r x} = E \left( \frac{hb}{L} \right) \left[ \frac{N}{m} \right], K_{F_y, d r y} = E \left( \frac{bh^3}{L^3} \right) \left[ \frac{N}{m} \right], K_{F_z, d r z} = E \left( \frac{bh^3}{L^3} \right) \left[ \frac{N}{m} \right] \quad 3.6$$

$$K_{M_x, d \theta_x} = \frac{1}{3} \left( \frac{bh^3}{L} \right) \left( \frac{E}{2(1+\mu)} \right) \left[ \frac{Nm}{rad} \right], K_{M_y, d \theta_y} = \frac{E}{12} \left( \frac{hb^3}{L} \right) \left[ \frac{Nm}{rad} \right], K_{M_z, d \theta_z} = \frac{E}{12} \left( \frac{hb^3}{L} \right) \left[ \frac{Nm}{rad} \right]$$

Wherein

b= Leaf spring width, in m.

h = Leaf spring height, in m.

L = Leaf spring length, in m.

E= Young's modulus, in N/m<sup>2</sup>.

v= poisson ratio.

We start by calculating the stiffness matrix of an individual leaf spring in the point P indicated in figure 3.10. To calculate this matrix we need two transformation matrices ( $T_{11}$  and  $T_{12}$ ) as defined in equation 3.7, to calculate the stiffness matrix of a folded leaf spring in P.

$$T_{1i} = \begin{bmatrix} \cos(\alpha) & -\sin(\alpha) & & & & \\ \sin(\alpha) & \cos(\alpha) & & & & \\ & & 1 & & & \\ & -z & y & \cos(\alpha) & -\sin(\alpha) & \\ z & & -x & \sin(\alpha) & \cos(\alpha) & \\ -y & x & & & & 1 \end{bmatrix} \quad \begin{array}{l} \text{for } i = 1: \alpha = -\frac{\pi}{2}, x = \frac{L}{2}, y = r, z = 0 \\ \text{for } i = 2: \alpha = \pi, x = r - \frac{L}{2}, y = 0, z = 0 \end{array} \quad 3.7$$

$\alpha$  = is the angle, in rad.

$x$ ,  $y$  and  $z$  = are the displacements along the local leaf spring coordinate system, in m.

The stiffness matrix of one folded leaf spring in P can then be calculated as in equation 3.8.

$$K_{f@P} = T_{11}K_l T_{11}^T + T_{12}K_l T_{12}^T \quad 3.8$$

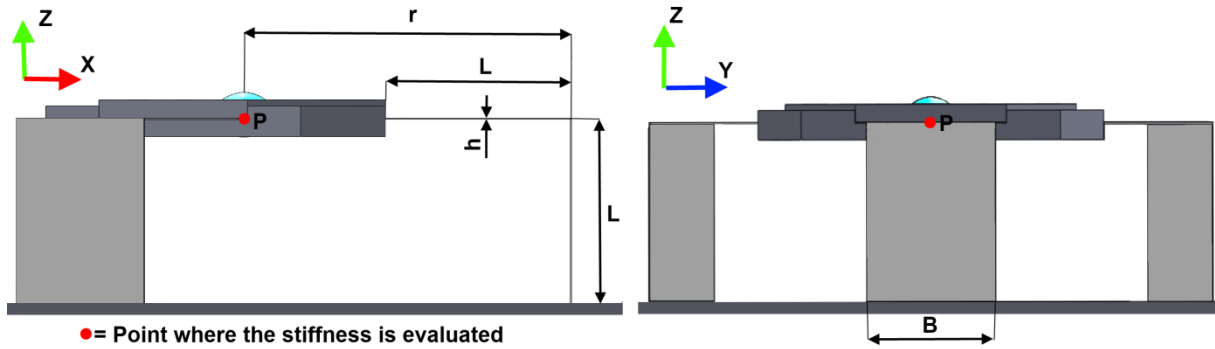


Figure 3.10: The folded leaf spring dimensions for the analytic calculation

To calculate the stiffness matrix in point P for three folded leaf springs (equation 3.11) in the global coordinates (defined in figure 3.10), we need three additional rotation matrices (equation 3.9 and 3.10).

$$T_{2i} = \begin{bmatrix} \cos(\alpha) & & \sin(\alpha) & & & \\ & 1 & & & & \\ -\sin(\alpha) & & \cos(\alpha) & & & \\ & & & \cos(\alpha) & & \sin(\alpha) \\ & & & & 1 & \\ & & & -\sin(\alpha) & & \cos(\alpha) \end{bmatrix} \quad \begin{array}{l} \text{for } i = 1: \alpha = \frac{2\pi}{3} \\ \text{for } i = 2: \alpha = \frac{4\pi}{3} \end{array} \quad 3.9$$

$$T_3 = \begin{bmatrix} 1 & & & & & \\ & \cos(\alpha) & -\sin(\alpha) & & & \\ & \sin(\alpha) & \cos(\alpha) & & & \\ & & & 1 & & \\ & & & & \cos(\alpha) & -\sin(\alpha) \\ & & & & \sin(\alpha) & \cos(\alpha) \end{bmatrix} \quad \text{with } \alpha = \frac{\pi}{2} \quad 3.10$$

$$K_{T@P} = T_3 \left( K_{f@P}^{-1} + (T_{21}K_{f@P}T_{21}^T)^{-1} + (T_{22}K_{f@P}T_{22}^T)^{-1} \right)^{-1} T_3^T \quad 3.11$$

The symbolic expression of  $K_T$  is very lengthy and omitted from the report, however if we evaluate the expression for  $B=10.5[\text{mm}]$ ,  $L=15[\text{mm}]$ ,  $r=26.13[\text{mm}]$ ,  $h=0.1[\text{mm}]$ ,  $E=2.05[\text{GPa}]$  and  $\nu=0.28$ , this results in the stiffness matrix in equation 3.12.

$$K_T = \begin{bmatrix} 2.80 \cdot 10^2 \left[ \frac{\text{N}}{\text{mm}} \right] & & & & -3.45 \cdot 10^1 \left[ \frac{\text{N}}{\text{Deg}} \right] \\ & 2.80 \cdot 10^2 \left[ \frac{\text{N}}{\text{mm}} \right] & & & -3.45 \cdot 10^{-1} \left[ \frac{\text{N}}{\text{Deg}} \right] \\ & & 6.53 \cdot 10^{-1} \left[ \frac{\text{N}}{\text{mm}} \right] & & \\ & -1.98 \cdot 10^1 \left[ \frac{\text{Nmm}}{\text{mm}} \right] & & 1.56 \cdot 10^1 \left[ \frac{\text{Nmm}}{\text{Deg}} \right] & \\ 1.98 \cdot 10^1 \left[ \frac{\text{Nmm}}{\text{mm}} \right] & & & 1.56 \cdot 10^1 \left[ \frac{\text{Nmm}}{\text{Deg}} \right] & \\ & & & & 9.00 \cdot 10^2 \left[ \frac{\text{Nmm}}{\text{Deg}} \right] \end{bmatrix} \quad 3.12$$

**FEM stiffness calculation**

The principal stiffnesses of the suspension were examined and plotted in table 3.3 and table 3.4. A detailed comparison of the theoretical, FEM and measured stiffness can be found in chapter 4.3.4. In addition a small analysis regarding gravity and the suspension was done this can be found in annex G.

Table 3.3: the system X, Y, Z and Rx stiffness

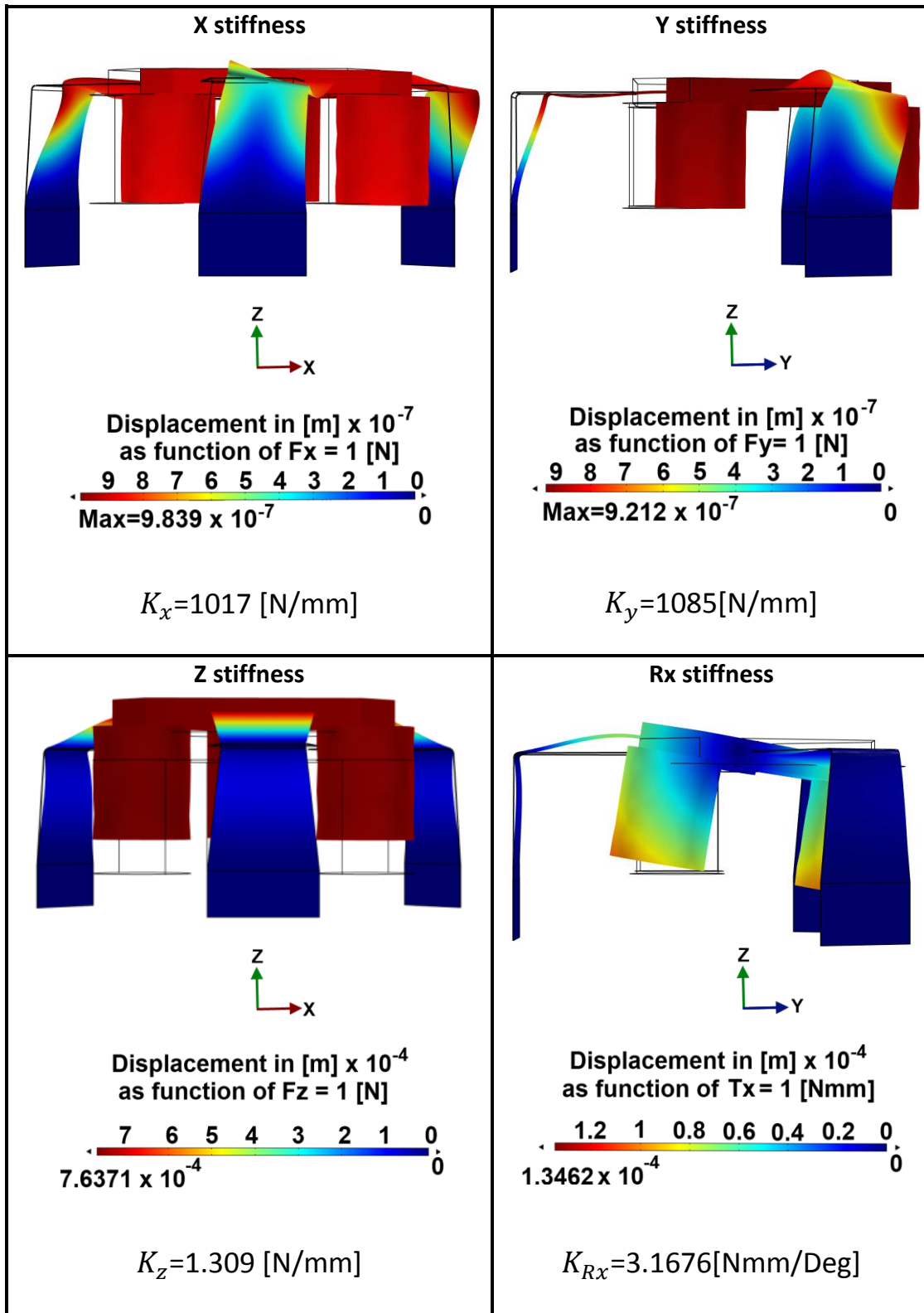
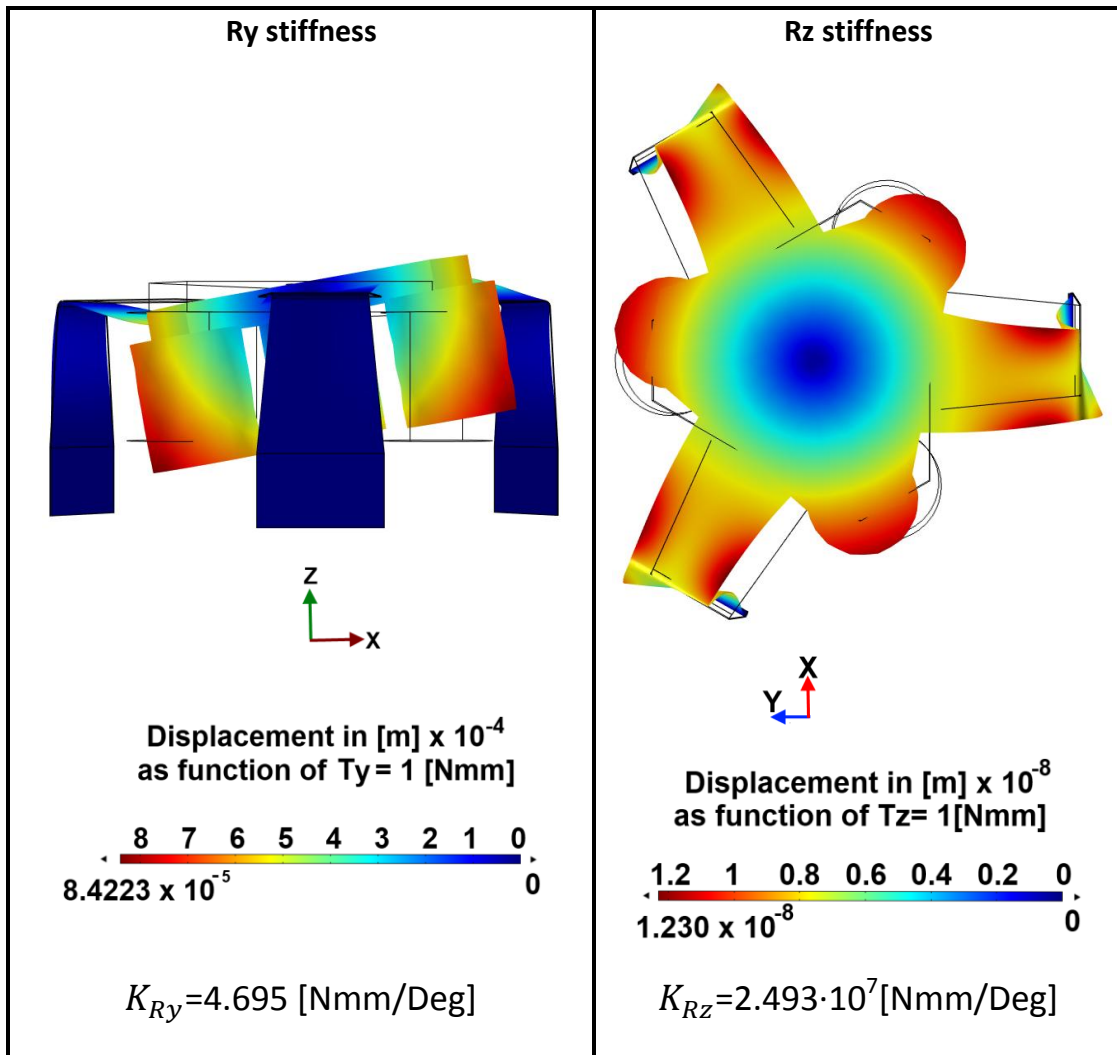


Table 3.4: the system Ry and Rz stiffness





### 3.2.4 Von Mises Stress

In order to know whether the design will not fail due to the stresses caused by applying the actuation forces and gravity to the suspension. To have an indication of whether the suspension will fail we will use the von Mises yield criterion defined in equation 3.13.

$\sigma_{vm} < \sigma_Y$	3.13
--------------------------	------

Where  $\sigma_{vm}$  is defined as

$$\sigma_{vm} = \sqrt{\frac{1}{2}((\sigma_1 - \sigma_2)^2 + (\sigma_2 - \sigma_3)^2 + (\sigma_3 - \sigma_1)^2)} \quad 3.14$$

With  $\sigma_1$ ,  $\sigma_2$  and  $\sigma_3$  being the principal stresses.

The von Mises stress was calculated for the combinations and the individual components of the applied displacements (table 3.5).

Of the 1.4310 steel the material properties which were used are, the yield strength ( $\sigma_{0.2} = 205[MPa]$ ) and tensile strength ( $\sigma_T = 515[MPa]$ ) taken from [37].

Although the design is not yet optimised for combined loads or long term fatigue, this preliminary optimization and the simulated stress distribution indicate that the current design is sufficient for a proof of principle to illustrate the full movement range for all axis, because all maximum stresses of single axis movements ( $\sigma_z = 2.925 \cdot 10^7 Pa$ ,  $\sigma_{Rx} = 1.526 \cdot 10^8 Pa$ ,  $\sigma_{Ry} = 1.773 \cdot 10^8 Pa$ ) are lower than the yield strength ( $\sigma_{0.2} = 2.05 \cdot 10^8 Pa$ ). The combined stress ( $\sigma_c = 4.00 \cdot 10^8 Pa$ ) though lower than the tensile strength is still significantly higher than the  $\sigma_{0.2}$ .

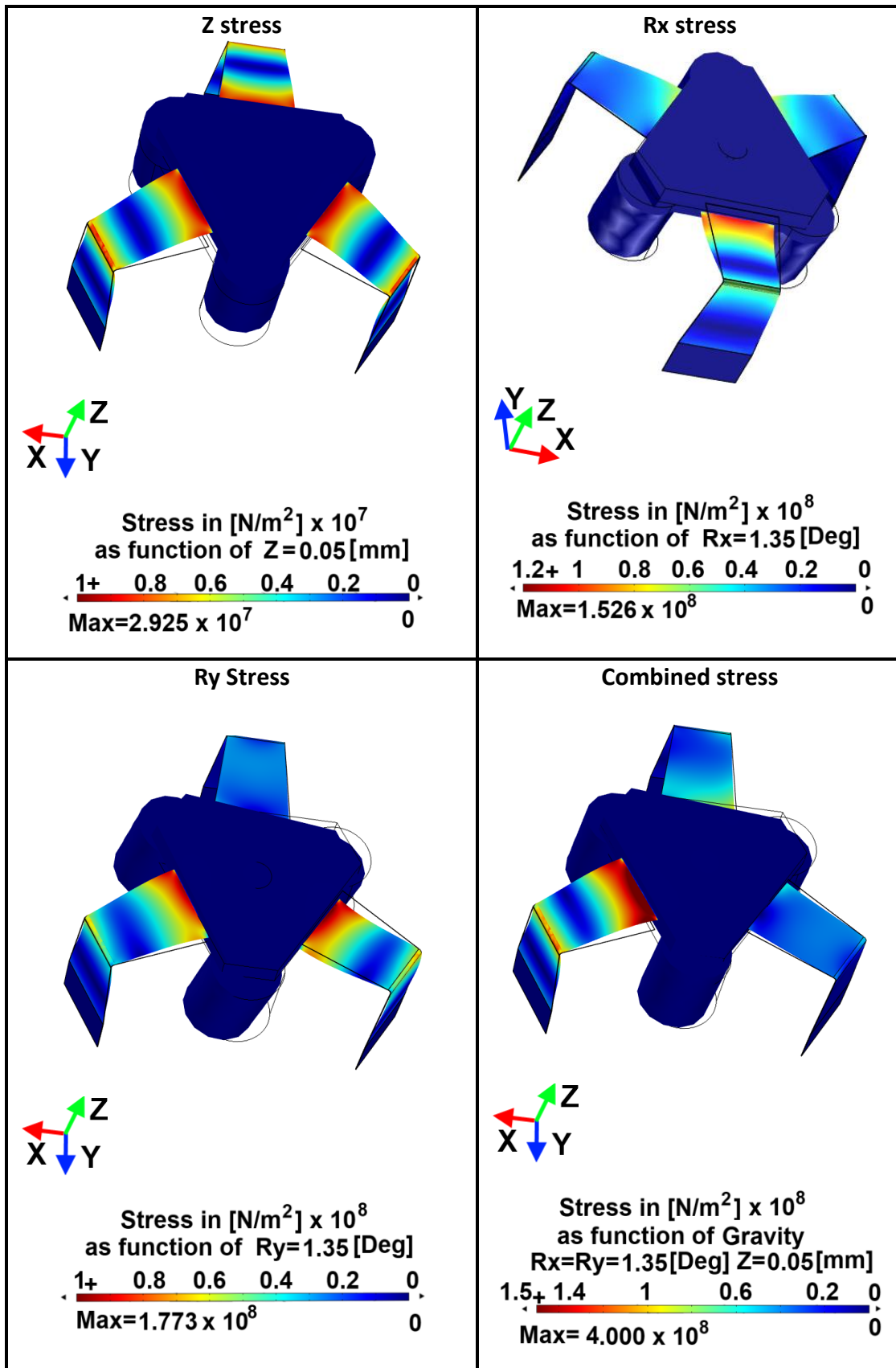
In order to confirm that the internal stresses originating from the fabrication process together with the stresses from movement would not cause problems, a small practical experiment was done by cutting a suspension out of the leaf spring steel and folding the leaf springs. These quick tests gave enough confidence, as the suspension did not fail over the desired movement range.

The highest stress concentrations are located at the fold and at the part clamped to the moving body of the folded leaf springs; this is caused by the large deformations occurring locally at these locations.

For the full range high-dynamic motion, the design will have to be further optimised to further reduce stress concentrations. These final optimisations are beyond the scope of this work.

Internal stresses induced by the manufacturing process are currently also not taken into account in the FEM and should be considered for a final optimization.

Table 3.5: Von Mises stress for the designed displacements. One can see from all load cases that the most critical parts are the clamped part and the fold, as these have the highest stress concentrations.



## 3.3 Actuation

### 3.3.1 Comparison and choice

For the actuator three different concepts were considered, the first being amplified piezo stacks, the second a direct piezo stack and the third linear voice coil actuation. Though actuator selection is unique for every design, the comparison of these options is summarized in table 3.6. (the statistics were based on a comparison of various feasible options from [38](Cedrat apa150m), [39] (PI P-841.6), [40](BEI Kimco LA05-05-000A). Other resources which were used for the selection are mentioned in references [30] and [40–45].

**Table 3.6: Actuator considerations, from the comparison it was concluded that using a linear voice coil seemed the best option in this design.**

	Amplified piezo stack	Piezo stack	Linear voice coil
Dynamics over a 100 $\mu\text{m}$ stroke	0	-	+
Actuator force	+	++	-
Stroke	0	-	++
Construction volume	-	-	++
Stiffness in N/m	$\sim 5 \cdot 10^5$	$\sim 10^7$	0 (Full control stiffness)
Requires coupling to avoid an over-constrained moving body.	Yes	Yes	No
Added mass	Part of the mass of the coupling	Part of the mass of the coupling	0.907 g (per coil)
Cost	$\sim \text{€}1000$	$\sim \text{€}10000$	$\sim \text{€}400$
Availability within	4 weeks	6 weeks	4 weeks

Eventually the choice was made for a linear voice coil actuator, besides reasons such as delivery time and cost, voice coil actuators have a relatively larger stroke ( $\pm 0.5$  mm), which allows for larger angles and combined motions.

Also voice coils can be optimized for high dynamics over the full stroke (depending on the sensor and amplifier choice).

While piezos are generally more optimised for high dynamics strokes in the 1-10  $\mu\text{m}$  range, high dynamics optimised over the full range. I.e. strokes of 100  $\mu\text{m}$  will be problematic at high control frequencies, especially for the power supply (as peak current is proportional to peak to peak voltage, and the peak power is proportional to nominal voltage times the peak to peak voltage.)

The cons of voice coil actuators could be considered that they generally provide a lower force than piezo based solutions, but the force is more than sufficient for the designed suspension.

The added mass to the system, of a voice coil, is negligible compared to the fact that the piezo solutions require a coupling to make sure the mechanism is not over constrained.

Regarding the construction volume whereas a typical piezo takes up a relatively large volume ( $\emptyset 12$  by 125mm), and an amplified piezo (22.5 by 80.10 by 60 mm) and a voice coil (12.7 by  $\emptyset 12.7$  mm).

As for the stiffness, while a combination of three amplified actuators would just suffice for the required  $10^6$  [N/m] (see figure 3.4), three piezo stacks would be more than sufficient in stiffness.

As for the stiffness of voice coils is entirely control loop dependant, implying that it is dependent on the noise (e.g. sensor and amplifier noise) and signal strength in the control loop.

### 3.3.2 The voice coil

#### Voice coil specifications

After comparing various suppliers, the LA05-05-000A voice coils from the manufacturer BEI-Kimco were chosen. For a detailed review of the actuator specifications the reader is referred to the suppliers (BEI Kimco's) website [40]. Table 3.7 gives a brief overview of the actuator and its specifications.

**Table 3.7: Actuator specifications**

Peak force	0.7 [N]
stroke	+/- 0.5 [mm]
Continuous stall force	0.31 [N]
Total stroke	1.02 [mm]
Actuator constant	$0.289 \left[ \frac{N}{\sqrt{W}} \right]$
Force sensitivity	$0.575 \left[ \frac{N}{A} \right]$
Electrical time constant	24.3[ $\mu$ s]
Mechanical time constant	11 [ms]
Inductance	97[mH]
Voltage @Fp	4.84[V]
Current @Fp	1.21[A]
Power @Fp	5.83[Watt]
Weight of the coil assembly	0.907[g]
Weight of the field assembly	8.50[g]
Max allowable coil temperature	155[ $^{\circ}$ C]
Thermal resistance of the coil	74[ $^{\circ}$ C/Watt]
Clearance on each side of the coil	0.381 [mm]

#### Voice Coil actuator range calculations

The voice call actuators can be directly connected to the flexures which simplifies the overall design. The direct connection between the actuators and the clamping body is nevertheless limited by the tolerances of the gap between the voice coil and the magnet yoke.

To evaluate the maximum possible angles, a model (implemented in Matlab) was made using the worst-case tolerances. The results of this model are shown in figure 3.11 & figure 3.12.

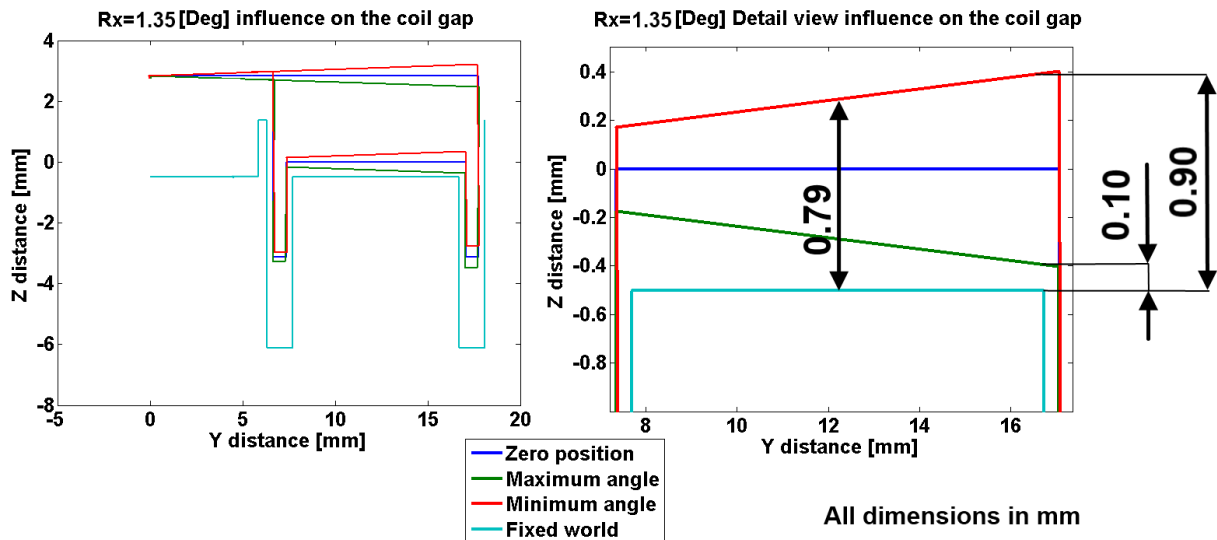


Figure 3.11: Coil gap size as function of rotation around the X axis, it can be observed that with a 1.35 deg rotation around X there is  $\pm 0.1$  mm of Z stroke available.

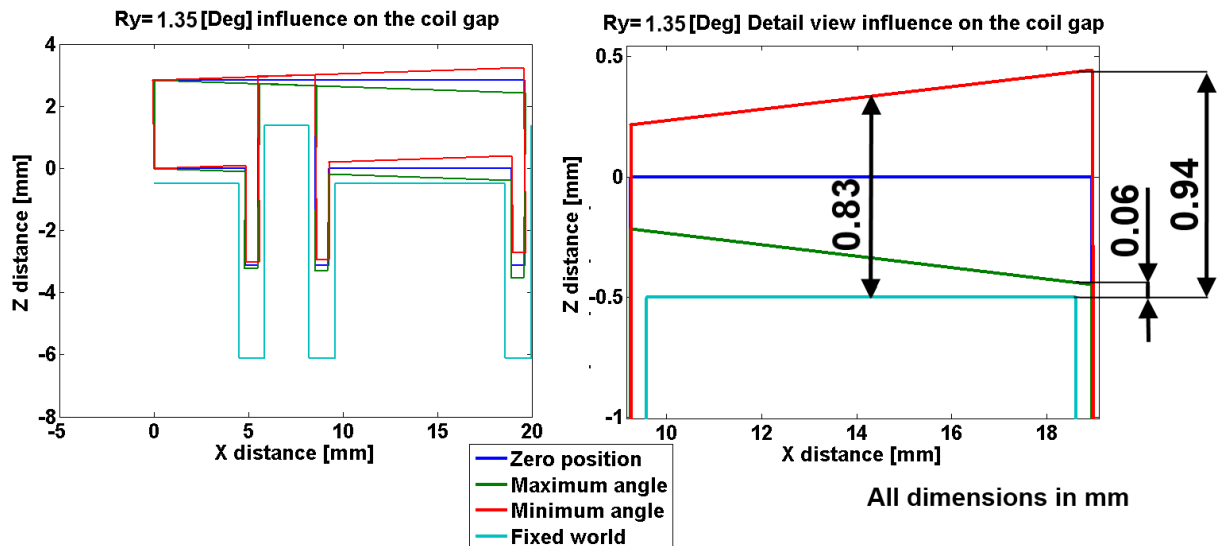


Figure 3.12: Coil gap size as function of rotation around the Y axis, it can be observed that with a 1.35 deg rotation around Y there is  $\pm 0.06$  mm of Z stroke available.

From these figures we can see that with the maximum required angle of 1.35 Degrees the gap sizes are still allowing the desired motions. Even with a maximum angle there is still  $\pm 0.06$  [mm] range, the difference between the axes is  $\pm 20\mu\text{m}$ . It should be noted that careful assembly and alignment are required to optimise the usage of this method, as both the travel distance and alignment have to be done within  $\pm 0.06$  [mm].

### 3.3.3 Sensors

For the sensor readily available D64-EQ Philtec fibreoptic sensors were used and calibrated. These sensors basically consist of a set of fibres of which half emits light and the other half receive the light after reflection on the target. The light back into the measurement device where the intensity is measured and analysed.

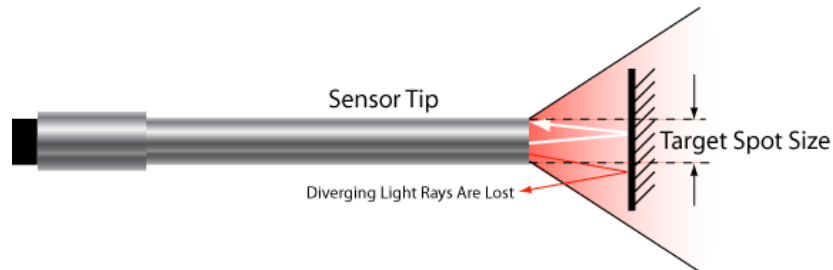


Figure 3.13: sensor measurement principle from [47]

The sensors measure three z displacements of three target areas at the back of the lens clamp (figure 3.14). These z-displacements are converted into the global  $Z$ ,  $R_x$  and  $R_y$  coordinates.

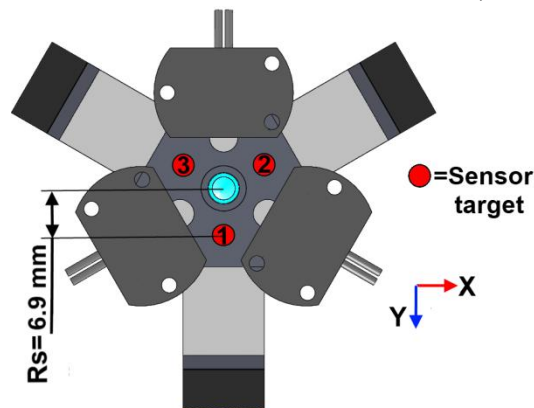


Figure 3.14: Sensor target locations on the lens clamp

The sensors (Philtec type D64-EQ) were used on their far side range, though the sensitivity is significantly less, the near side did not provide sufficient range ( $\approx 50 \mu\text{m}$  linear range,  $\approx 200 \mu\text{m}$  nonlinear range). The far side on the other hand has a linear range of  $\approx 1.5 \text{ mm}$  (as indicated in figure 3.15).

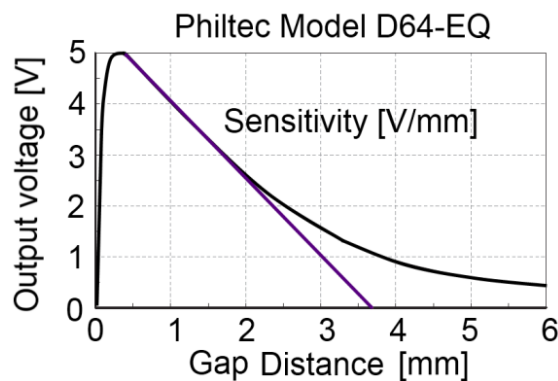


Figure 3.15: Typical sensor response over its far side, a larger movement range at the cost of sensitivity.

The measured sensitivities of the used sensors (1, 2 and 3) are respectively;  $-1.1832$ ,  $-1.1285$  and  $-1.1158 \text{ V/mm}$ .

## 3.4 Design synthesis, fabrication and assembly

### 3.4.1 Suspension design overview

After the dimensioning of the folded leaf springs the final leaf spring design looked as shown in figure 3.16. The aspheric focal lens is glued with UV curing glue into the upper membrane clamp. For a complete overview of the drawings of the setup the reader is referred to annex F. As for the rotational centre it is determined by the distance from the bottom side of the lower membrane clamp to the focal lens.

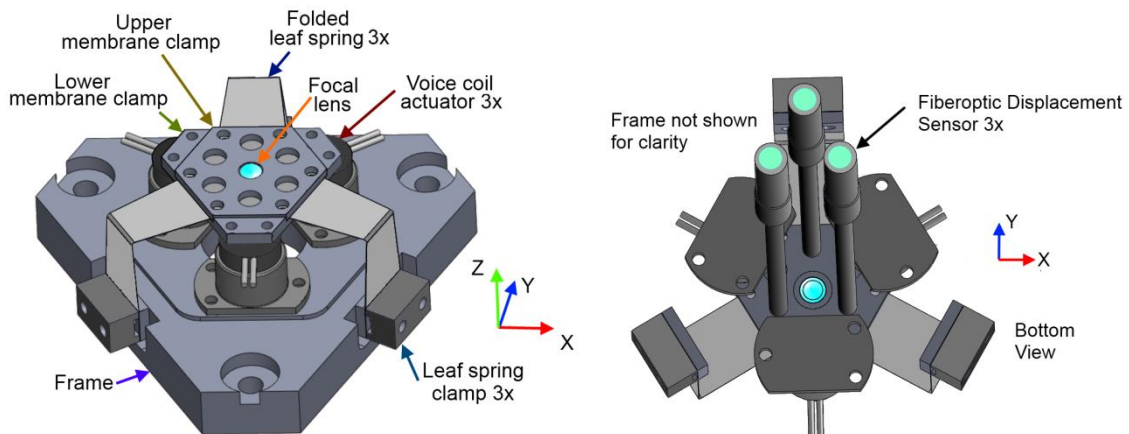


Figure 3.16: The miniature laser scanning head with all parts as indicated in the figure

The membrane was manufactured by laser cutting it from a steel plate of Hasberg 1.4310 stainless spring steel [36]. After lasercutting the membrane all three leaf springs were folded.



Figure 3.17: folding the leaf springs, left an unfolded and folded leaf spring membrane, right the bending machine.

After folding all the leaf springs, the suspension was assembled. The most tedious part of the assembly was the proper alignment of the voice coils.

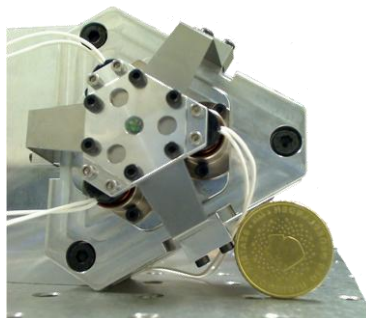


Figure 3.18: final assembled design





## **Chapter 4    Experimental design validation**

---

## 4.1 Experimental setup

After having the design realised, the goal was to validate the realised motion range, possible future motion range, evaluate the sensors, measure the stiffness, verify the eigenfrequencies and have an idea of their damping, start with the basis of decentralised control.

The setup (displayed in figure 4.1) is controlled using a computer operating Matlab simulink in a Linux environment. The computer is connected to two DAQs (microgiant TU/eDACS[48]) via usb 2.0 connections. On the ADC input ports the data from three fibre-optic (Philtec [47]) sensors is read, three DAC output ports are connected via three resistors to the three voice coil actuators (LA05-05-000A BEI Kimco [40]). The voice coil yokes are mounted on the frame and the coils on the suspension.

The setup further consists of a diode laser shining through a beam splitter and filtering plates to reduce the intensity, after which it goes through the focal lens, focusing the beam on the CCD chip that measures the displacement of the beam. The output of the CCD is only used to illustrate the movement of the spot for the proof of the principle.

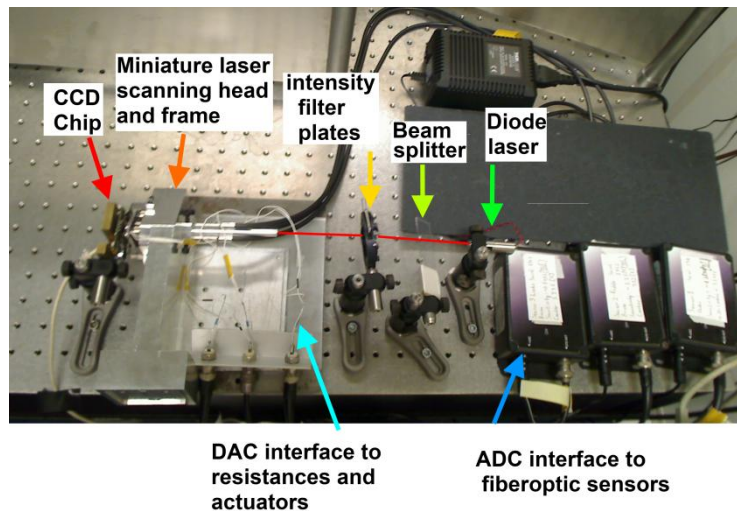


Figure 4.1: Picture of the experimental setup, the diode laser shines through a beam splitter and intensity filter plates in order to reduce the intensity for the CCD chip. After being filtered the diode laser shines through the lens in the miniature laser scanning head, steering the beam focus over the CCD chip.

The setup is controlled with an open-loop voltage-based control. The voltage limits are +/-10 Volt. The resistance of the system being  $104 \Omega$ , thus the current is limited to 0.096 A. The maximum applied force  $F_z$  is therefore 0.166[N] and the corresponding torques  $T_x$  and  $T_y$  are 1.170 Nmm and 1.351 Nmm, respectively. The signal outputs of the sensors are measured and converted to displacement at the sensor position. The latter is then converted into global position coordinates of the platform.

## 4.2 Sensors qualification

To qualify the performance of the sensors used in this setup, the signal to noise ratio (SNR) was measured to have an idea of attainable resolutions over the total motion range (as seen in table 4.1).

Table 4.1: Sensor evaluation

Movement	Sensor	$A_{signal\_rms}$	$A_{noise\_rms}$	$SNR = \left(\frac{A_{signal}}{A_{noise}}\right)^2$
<b>Z</b>	1	0.1484 [mm]	0.0048 [mm]	953.5134
	2	0.1414 [mm]	0.0049 [mm]	848.0560
	3	0.1499 [mm]	0.0060 [mm]	618.7882
	Global	0.1465 [mm]	0.0052 [mm]	793.7223
Movement	Sensor	$A_{signal\_rms}$	$A_{noise\_rms}$	$SNR = \left(\frac{A_{signal}}{A_{noise}}\right)^2$
<b>Rx</b>	1	0.0278 [mm]	0.0017 [mm]	271.2133
	2	0.0228 [mm]	0.0016 [mm]	213.3571
	3	0.0247 [mm]	0.0015 [mm]	273.8216
	Global	0.2828 [Deg]	0.0088 [Deg]	1044.7
Movement	Sensor	$A_{signal\_rms}$	$A_{noise\_rms}$	$SNR = \left(\frac{A_{signal}}{A_{noise}}\right)^2$
<b>Ry</b>	1	0.0090 [mm]	0.0017 [mm]	29.5932
	2	0.0283 [mm]	0.0016 [mm]	300.6857
	3	0.0290 [mm]	0.0016 [mm]	313.2499
	Global	0.2793 [Deg]	0.0110 [Deg]	643.4329

These measurements show that the signal to noise ratio of the sensors is relatively low. The root mean square (RMS) amplitude of the noise is for each axis ( $Z=5.2\mu\text{m}$ ,  $R_x=0.0088\text{ Deg}$ ,  $R_y=0.0110\text{ Deg}$ ) implying that the attainable accuracy in Z with these sensors is not sufficient for the final design (with the initial specifications). It is nevertheless sufficient for the purpose of demonstrating this first prototype.

## 4.3 Motion range measurements

### 4.3.1 Methodology

To measure the motion range, the procedure was to measure it using two different signal types.

- The first being nine voltage steps (over the voltage span), to analyse the realised stiffness.
- The second a sinus over the entire voltage span, to analyse sensor performance with the Signal to Noise Ratio.

### 4.3.2 Z movement range

The Z movement range of the final suspension without additional amplifiers is  $\pm 0.2$  [mm], as can be seen in figure 4.2. This is more than sufficient because the desired range was  $\pm 0.05$  [mm]. Due to the system being controlled in openloop every step included an overshoot as large as the step itself, with about 0.25 sec of settling time, i.e. the time it takes till the final value is reached.

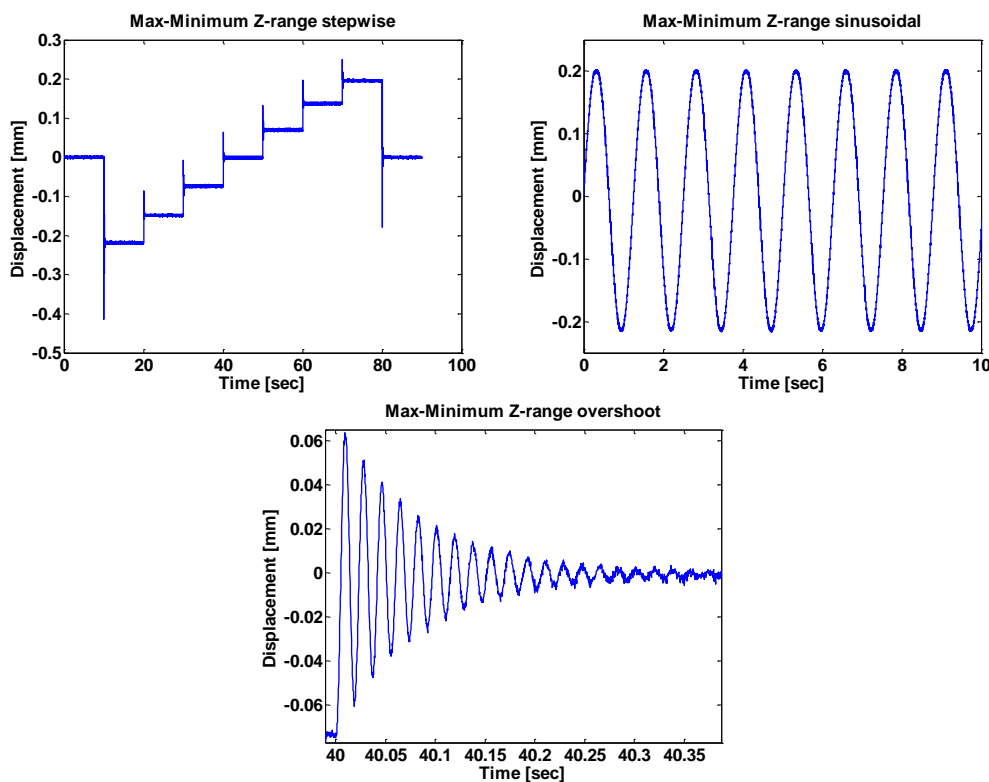


Figure 4.2: Z movement range in global coordinates, it can be seen that the total achieved movement range is  $\pm 0.2$  mm, besides that we can see that it takes about 0.25 sec to drop to the final value and the overshoot is about equal to the stepsize.

### 4.3.3 Angular motion range

The  $R_x$  and  $R_y$  range is +/- 0.4 [Deg] as can be seen in figure 4.3. This is less than desired, but is only caused by insufficient current in the coils in the present setup.

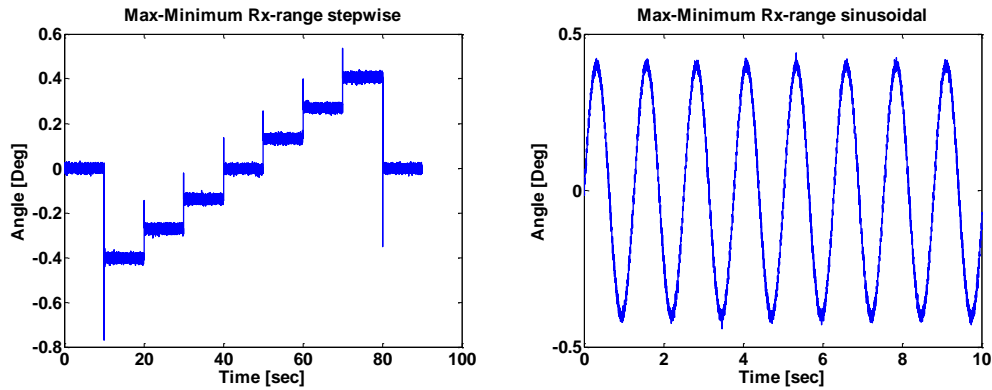


Figure 4.3:  $R_x$  angular motion range as a function of global coordinates for two types of signal inputs (step and sinusoidal inputs). (Side note: the  $R_y$  motion range showed identical plots and thus is not shown.)

### 4.3.4 Expected setup motion range

Though the total motion spans were not yet achieved, with the present setup they were approximated based on the measured stiffness (of which the derivation is discussed in §4.4). To calculate the motion spans related to the maximum voice-coil force equation 4.2 can be used together with the measured stiffness matrix (equation 4.1). The results are summarised in table 4.2.

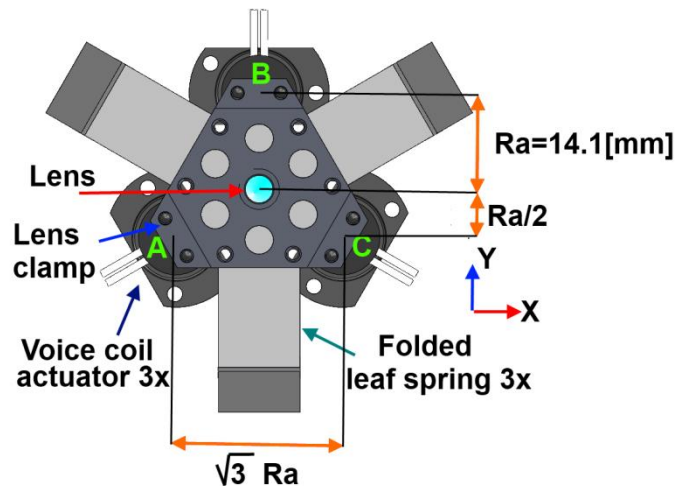


Figure 4.4: actuator layout, the 3 voice coils (indicated with A, B and C) are oriented as shown in this picture, the coils (Black part), are directly attached to the lens clamp, which is fixed to the lens. By actuating the lens clamp the folded leaf springs, allow the clamp and lens to move.

$$K_m \begin{bmatrix} 0.7856 & -0.4125 & -0.9221 \\ -0.0184 & 2.8915 & -0.0778 \\ 0.0110 & -0.5178 & 3.4225 \end{bmatrix} \quad 4.1$$

$$\begin{bmatrix} 1 & 1 & 1 \\ -\frac{R_a}{2} & R_a & -\frac{R_a}{2} \\ \frac{\sqrt{3}}{2}R_a & & -\frac{\sqrt{3}}{2}R_a \end{bmatrix} \begin{bmatrix} F_a \\ F_b \\ F_c \end{bmatrix} = \begin{bmatrix} F_z \\ T_{Rx} \\ T_{Ry} \end{bmatrix} = \begin{bmatrix} K_{zz} & K_{RxxZ} & K_{RyyZ} \\ K_{zRx} & K_{RxxRx} & K_{RyRx} \\ K_{zRy} & K_{RxxRy} & K_{RyRy} \end{bmatrix} \begin{bmatrix} Z \\ R_x \\ R_y \end{bmatrix} \quad 4.2$$

$R_a$ = Distance from the actuator to the centre of the lens (14.1 mm).

$F_a, F_b, F_c$ =Individual actuator force N in Z direction.

$F_z$  = Force in Newton, in the Z direction.

$T_{Rx}$  = Torque in Nmm, around the X axis.

$T_{Ry}$  = Torque in Nmm, around the Y axis.

$Z$  = Displacement of the lens in mm.

$K_{ij}$ =Components of the stiffness matrix.

$R_x$  = Rotation of the lens in Deg.

$R_y$  = Rotation of the lens in Deg.

From table 4.2 we can see that there might be problems with achieving larger ranges of motion. For the measured results, though the forces of the individual actuators which saturate are still below the peak force (0.7 N), they cannot be maintained continuously, i.e. these would limit the duty cycle for these cases.

This result is caused by the relatively large off centre terms in the stiffness matrix, causing the actuators to use a significant stroke on correcting the geometrical imperfections. If we look at the data in figure 4.5, which is the basis for the stiffness matrix (equation 4.1), we can see that though the assumption of linearity seem valid over the small investigated range ( $\pm 0.2$  mm  $\pm 0.4$  Deg  $\pm 0.4$  Deg); for the off centre stiffness terms (causing these effects), especially the {3,1} and {1,2} of figure 4.5, might have non linear effects for larger ranges, thus allowing larger motion.

**Table 4.2: Desired displacements limits related to individual actuator forces, the light red marked entries indicate the motions which are larger than the stall force (>0.31 N) can only be realised with the peak force (0.7 N).**

Displacement	Measured		
	$F_a$ [N]	$F_b$ [N]	$F_c$ [N]
$Z=0.05$ mm	0.013	0.013	0.013
$R_x= 1.35$ Deg	-0.307	-0.011	-0.249
$R_y= 1.35$ Deg	0.607	0.410	0.228
$Z=0.05$ mm $R_x=1.35$ Deg $R_y=1.35$ Deg	0.313	0.422	-0.001

## 4.4 Stiffness measurement

### Assumptions

The following assumptions are made to calculate the stiffness from the stepped motion ranges.

- Measured stiffnesses (figure 4.5) are assumed to be linear.
- An inherent assumption for the measurement data from equation 4.1, is that the sensors are located at equal radius ( $R_s=6.9$  mm) from the centre of the lens and have angles of  $120^\circ$  from each other.
- For equation 4.2, we assume that the actuators are located at equal radius ( $R_a= 14.1$  mm) from the centre of the lens and have angles of  $120^\circ$  from each other.
- The angle between an actuator to a nearest sensor is  $60^\circ$
- The sensors are calibrated perfectly, i.e. their sensitivities are valid over the range.
- The actuators all have the same force sensitivity.
- The actuators all have the same maximum stall (0.31 N) and peak force (0.7 N).

### 4.4.1 Methodology

Using the previous stepwise experiments (figure 4.2 and figure 4.3), the applied force is known for given displacements and because the distances from the centre of the lens to the centre of the actuator ( $r_a=14.1$  mm as indicated in figure 4.4) and the centre of the sensors ( $r_s=6.9$  m as indicated in figure 3.14) are also known, the stiffness can be calculated for each actuated axis.

$$\begin{aligned}
 F_{zmax} &= 3 \frac{10[V]}{104[\Omega]} 0.575 \left[ \frac{N}{A} \right] = 0.1659[N] \\
 T_{xmax} &= \frac{3}{2} 14.1 \frac{10[V]}{104[\Omega]} 0.575 \left[ \frac{N}{A} \right] = 1.1694[Nmm] \\
 T_{ymax} &= \sqrt{3} 14.1 \frac{10[V]}{104[\Omega]} 0.575 \left[ \frac{N}{A} \right] = 1.3503[Nmm]
 \end{aligned}
 \tag{4.3}$$

After knowing the forces applied per average displacement we can calculate the angles and displacement for each applied force (as shown in figure 4.5). By fitting a tangent to these results we can have a first order indication of the compliance matrix (equation 4.4).

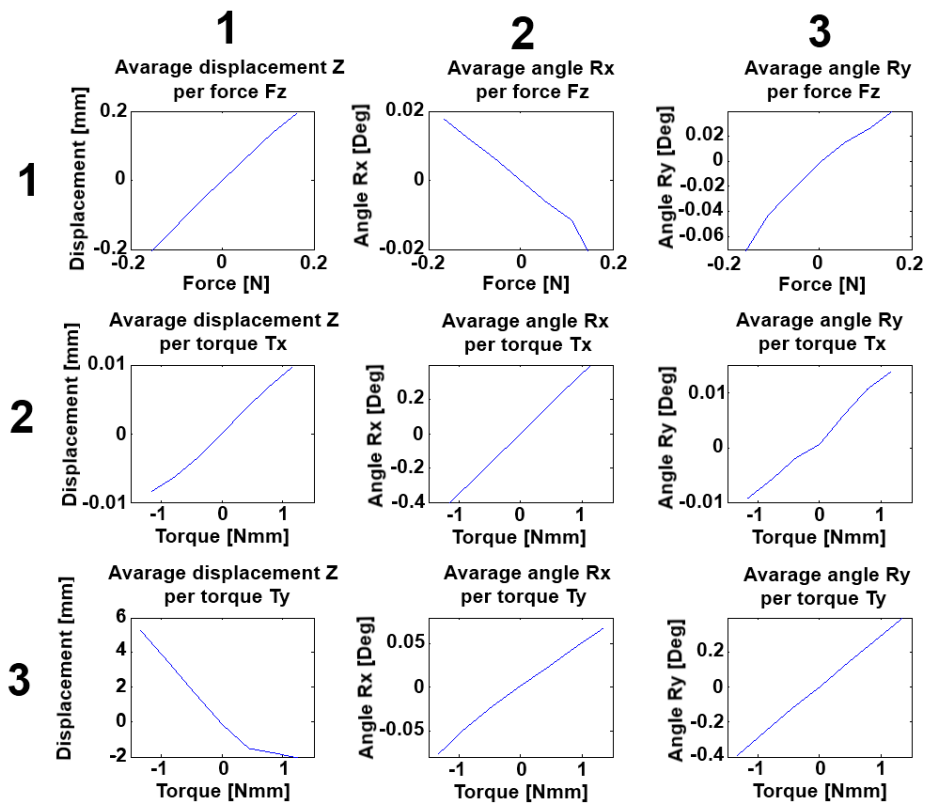


Figure 4.5: plots used for the derivation of the compliance and stiffness, each plot represents the respective matrix element of the compliance matrix.

$$C = \begin{bmatrix} 1.2653 \left[ \frac{\text{mm}}{\text{N}} \right] & -0.11995 \left[ \frac{\text{Deg}}{\text{N}} \right] & 0.33816 \left[ \frac{\text{Deg}}{\text{N}} \right] \\ 0.0079762 \left[ \frac{\text{mm}}{\text{Nmm}} \right] & 0.3465 \left[ \frac{\text{Deg}}{\text{Nmm}} \right] & 0.010028 \left[ \frac{\text{Deg}}{\text{Nmm}} \right] \\ -0.0028605 \left[ \frac{\text{mm}}{\text{Nmm}} \right] & 0.052809 \left[ \frac{\text{Deg}}{\text{Nmm}} \right] & 0.29261 \left[ \frac{\text{Deg}}{\text{Nmm}} \right] \end{bmatrix} \quad 4.4$$

Now taking the inverse of the compliance matrix results in the stiffness matrix (4.5). The off diagonal terms stiffness terms are relatively large. These off diagonal terms are not present in the analytic and FEM calculation and are most likely related to some of the previously stated assumptions not being valid, for instance imperfect alignment caused by geometrical tolerances

$$K = C^{-1} = \begin{bmatrix} 0.7856 \left[ \frac{\text{N}}{\text{mm}} \right] & -0.4125 \left[ \frac{\text{N}}{\text{Deg}} \right] & -0.9221 \left[ \frac{\text{N}}{\text{Deg}} \right] \\ -0.0184 \left[ \frac{\text{Nmm}}{\text{mm}} \right] & 2.8915 \left[ \frac{\text{Nmm}}{\text{Deg}} \right] & -0.0778 \left[ \frac{\text{Nmm}}{\text{Deg}} \right] \\ 0.0110 \left[ \frac{\text{Nmm}}{\text{mm}} \right] & -0.5178 \left[ \frac{\text{Nmm}}{\text{Deg}} \right] & 3.4225 \left[ \frac{\text{Nmm}}{\text{Deg}} \right] \end{bmatrix} \quad 4.5$$



### Stiffness comparison

The differences between the measured and the FEM stiffness is not that large ( $K_{Rx}$  0.91,  $K_{Ry}$  0.73 and  $K_{Rz}$  0.6), The results match well for the rotations however the Z stiffness discrepancy is larger, this is probably related to the various discrepancies between practice and FEM.

One of these discrepancies is that the change in stiffness due to the bending of leaf springs was not taken into account in the FEM, this effect will most likely only be localised in the fold, and thus is expected not to be critical for the stiffness calculations.

More likely imperfections are geometrical tolerances a brief investigation was already done with respect to the fold angle and radius (seen in annex H). From these we saw that the fold radius has a larger effect on the lowest eigenfrequency and will influence the stiffness quadratically.

A more thorough investigation of geometric tolerances and the FEM model would be in order to have a better understanding of the differences, but are beyond the scope of this report.

Because the FEM predicted stiffness's are higher than the ones measured, we expect the von Mises stress to be lower in reality than the one predicted in subchapter 3.2.4.

Table 4.3: Stiffness comparison

	Stiffness			Measured /FEM	Measured /Theory	FEM /Theory
	FEM	Theory	Measured			
$K_{Rx}$	3.168[Nmm/Deg]	15.6[Nmm/Deg]	2.892[Nmm/Deg]	0.91	0.19	0.20
$K_{Ry}$	4.695 [Nmm/Deg]	15.6[Nmm/Deg]	3.423[Nmm/Deg]	0.73	0.22	0.30
$K_{Rz}$	$2.493 \cdot 10^7$ [Nmm/Deg]	900 [Nmm/Deg]	-	-	-	27700
$K_x$	1017 [N/mm]	280 [N/mm]	-	-	-	3.63
$K_y$	1085 [N/mm]	280 [N/mm]	-	-	-	3.87
$K_z$	1.309 [N/mm]	0.653[N/mm]	0.786[N/mm]	0.60	1.1229	0.53

Comparing the measured results to the results from theory shows relatively larger deviations in the rotational stiffnesses ( $\approx 1/5^{\text{th}}$ ), this is expected to occur because the theoretical model does not take into account the bending radius. The z stiffness proves to be a relatively good estimate of the measurement.

All in all the rotational stiffnesses which are measured are lower than both the FEM and theory, implying that geometric tolerances are playing a role, most probably the bending radius is either larger than expected, or inconsistent between the various folded leaf springs. The measured z stiffness on the other hand is located in between FEM and theory.

If we compare the FEM and theory, we see that the  $K_{Rx}$  and  $K_{Ry}$  stiffness of the Theory are about 5 times higher; this is most likely caused by not taking into account the bending radius and the tapers in the folded leaf springs. As for the large difference in  $K_{Rz}$ , though the  $K_{Rz}$  stiffness is expected to be much larger than the  $K_{Rx}$  and  $K_{Ry}$ , it is the opinion of the author that the theoretical estimate will be more accurate, this because the  $10^7$  larger stiffness seems out of proportion to the rest of the system. Regardless of this result both theory and FEM, gave sufficient  $K_{Rz}$  to continue the design.

As for the  $K_x$  and  $K_y$ , these differ by proportional factors (3.63 and 3.87); this result is also expected to be caused by not taking into account the fold radius.

## 4.5 Frequency response measurement

From the system the bode plots were obtained displaying the systems eigenfrequencies. To have an indication of the fundamental frequencies, only the magnitudes are plotted here. For more details about the Phase, and coherence of the measurement, the reader is referred to appendix I.

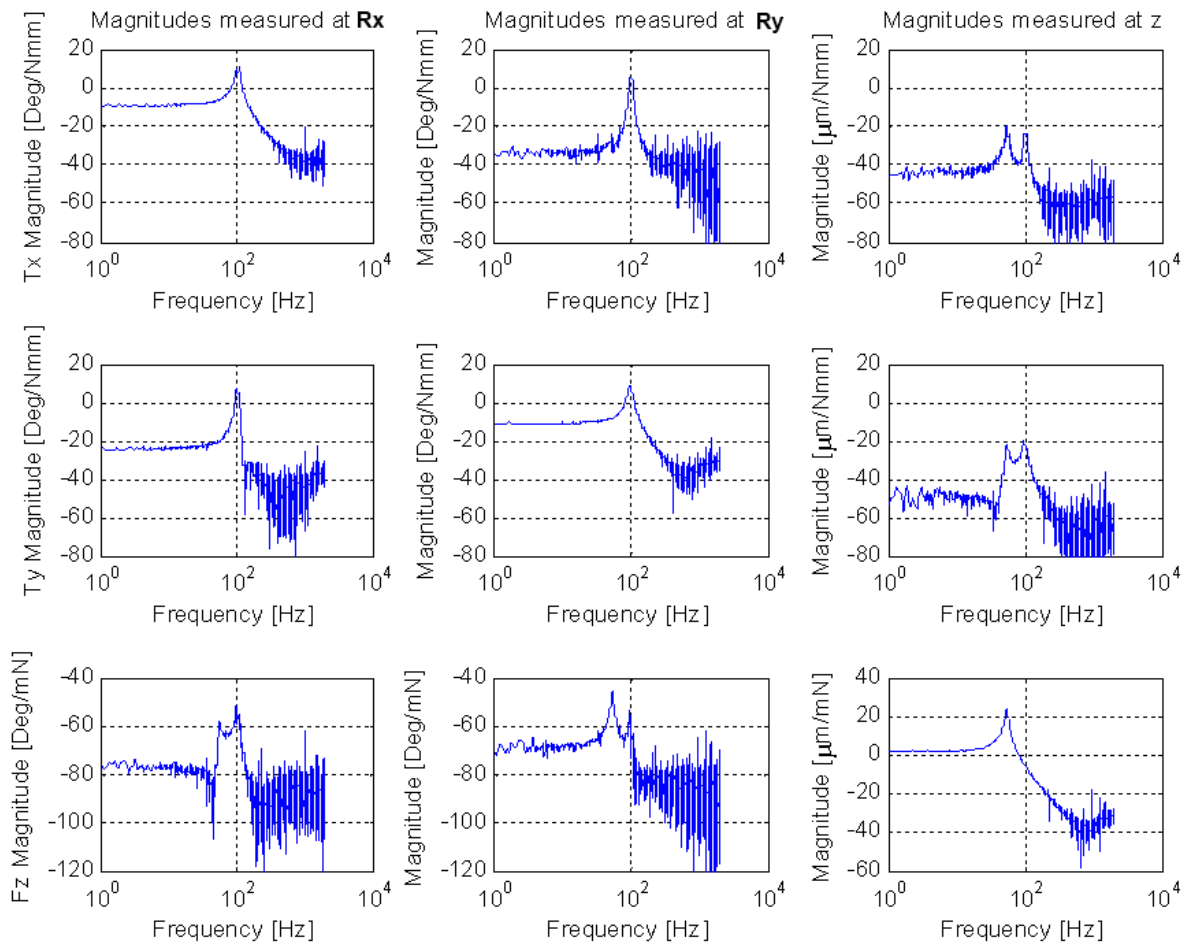


Figure 4.6: magnitude part of the bode plots of the system on a dB scale.

To obtain the eigenfrequencies and their quality factors we zoom in (figure 4.7) on the diagonal plots from Figure 4.6 .

The quality factor (also called Q-factor) provides an indication of the quality of the resonance and is inversely related to the damping ratio. A high Q-factor ( $Q > 0.5$ ) indicates that the system is under-damped and oscillates over a long period with a slowly decreasing amplitude. On the other hand, a low Q-factor ( $Q < 0.5$ ) implies an over-damped system that results in slower system response. For a system which has to follow an ideal trajectory (like in our case), the Q should be ideally critically damped, i.e. the Q-factor that would yield the fastest possible system response without having overshoot. Although in some applications overshoot is not critical, in this application it could be since it determines the accuracy with which we machine a pattern

The Q factor for underdamped systems can be determined by equation 4.6.

$$Q \approx \frac{f_n}{\Delta f} \quad 4.6$$

$f_n$  is the natural frequency of the system.

$\Delta f$  is the bandwidth of the peak defined by the  $-3$  [dB] points around the peak.

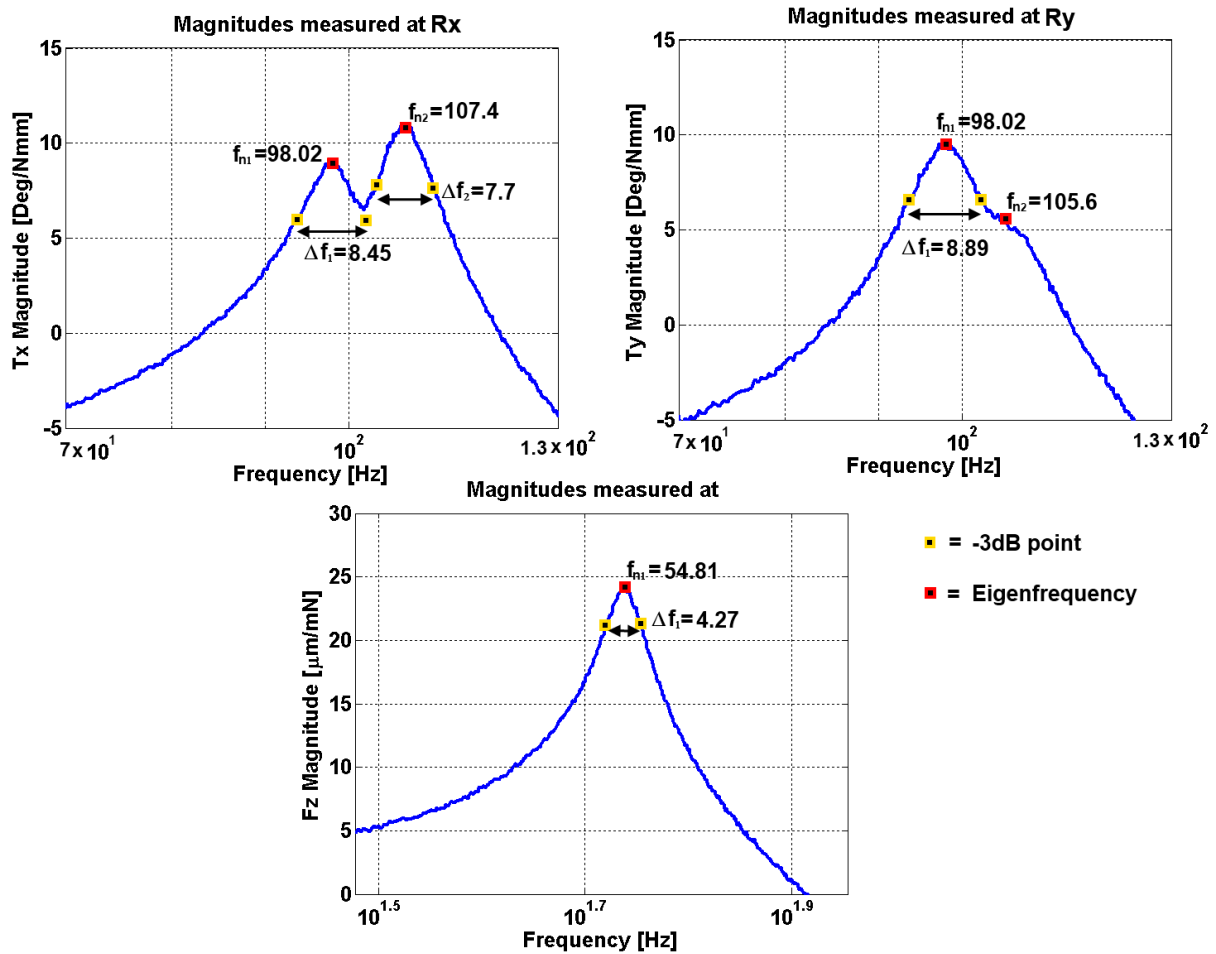


Figure 4.7: Zoomed in resonance peaks of the diagonal bode plots from figure 4.6 with magnitudes on a dB scale.

Table 4.4: Force limits related to displacement

	Frequency		Measured/ FEM		frequency	
	FEM	Measured			1	2
$f_{Rx}$	103.85[Hz]	107.4 [Hz]	0.9408	$Q_{Rx}$	11.6	13.9
$f_{Ry}$	103.90[Hz]	97.7 [Hz]	1.0337	$Q_{Ry}$	11.0	
$f_z$	64.76 [Hz]	54.81 [Hz]	0.8464	$Q_z$	12.86	

The differences in the frequencies between predicted and measured are indicated in table 4.4. The discrepancies with the Rotations are minor and the differences between Rx and Ry will mostly be due to the differences in folding of the leaf springs and geometrical tolerances.

Unfortunately due to the quality of the sensors, and the limited amplification capabilities for the actuators, higher frequencies could not be tested. , Based on the difference in stiffness and eigenfrequencies several conclusions can be drawn.

The Q values of the system indicate that the system is underdamped, which means that control most likely has to be utilised to damp these peaks sufficiently to operate the system at higher control bandwidths.

## 4.6 The relative gain array

The first step toward the implementation of a controller for the system is to investigate the relative gain array of the system. The relative gain array is defined by taking the element wise product ( $\times$ ) of plant ( $G$ ) with its own inverse transposed.

$$RGA(G) = G \times (G^{-1})^T$$

4.7

The relative gain array provides a measure of interactions between variables in a multivariable system. In an ideal case the control of each global coordinate should not influence the control of the other coordinates regardless of the control bandwidth. In this case the relative gain array would exist of all diagonal terms being one for all frequencies, while all off diagonal terms should be zero. The measured relative gain array is displayed in figure 4.8.

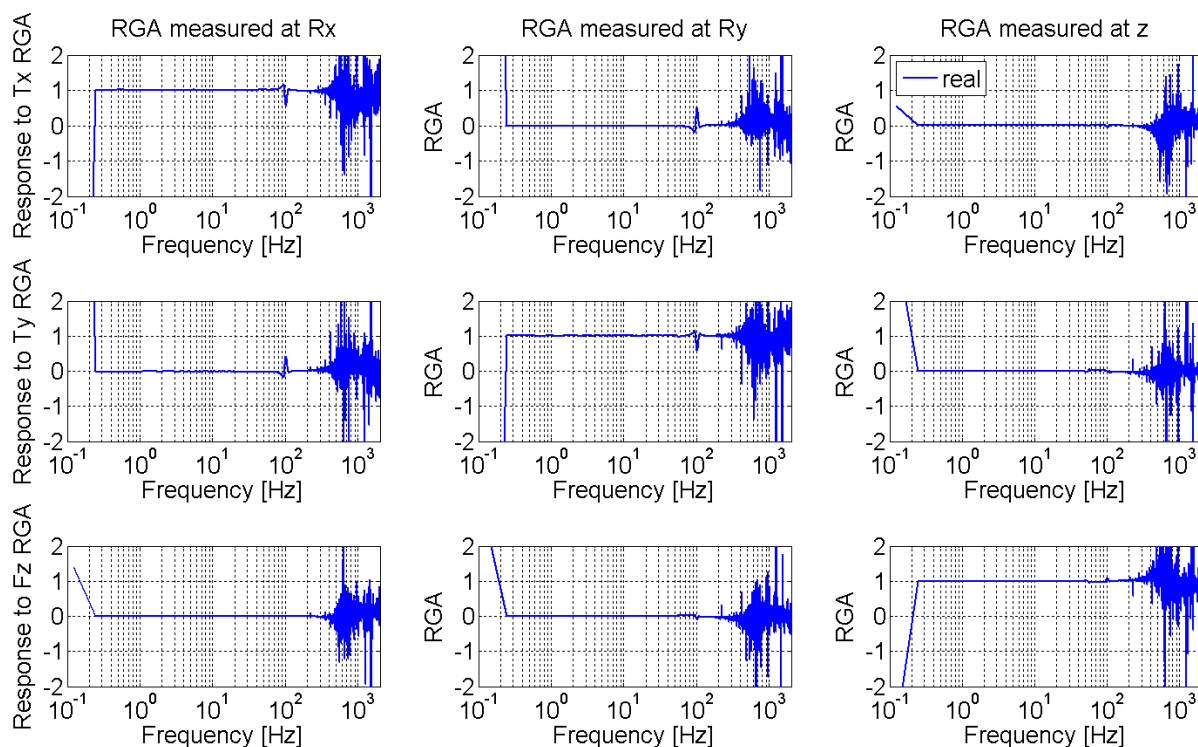


Figure 4.8: relative gain array of the setup over the measured frequency range.

Around the resonance frequency one can see in figure 4.9 that the rotational frequencies are having significant coupling. However for frequencies lower and higher there are possibilities for decentralised control (discussed further in [49]). For the higher frequencies however, the bode plot requires that the voice coils to be amplified and/or the sensors to have a better resolution for high control frequencies, so that higher control bandwidths can be investigated, without being limited by high frequency noise.

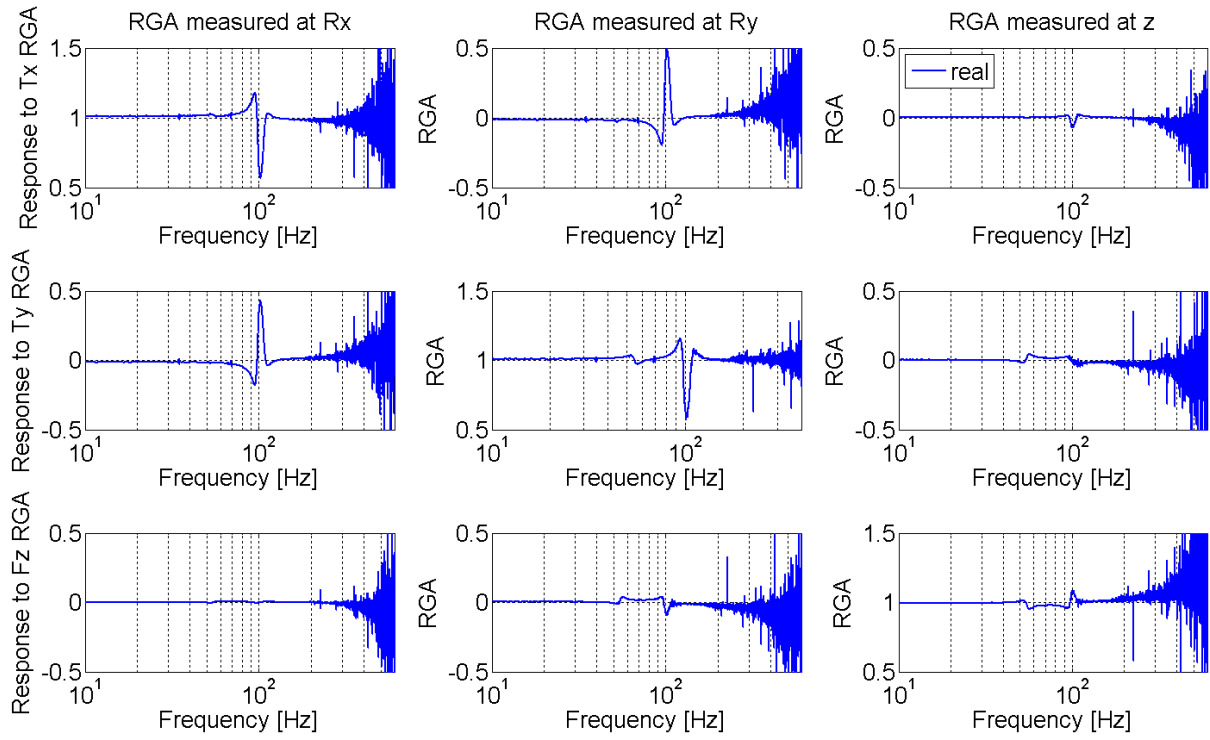


Figure 4.9: zoomed in RGA plot around the resonances of the system.



## **Chapter 5    Conclusions & Recommendations**

---

## 5.1 Conclusions

In the context of a manufacturing process, serving to manufacture integrated microstructures in transparent materials, a novel miniature laser scanning head was designed for this thesis. As a large part of the manufacturing process consists of femtosecond laser exposure, the scanning head serves to cope with the challenge of having sufficient printing speed for fabricating complex microstructures in a reasonable amount of time.

During the course of this thesis various focal optics were investigated, and eventually the focussing objective was replaced by an aspheric focussing lens. This aspheric lens reduced the moving mass and volume significantly, respectively by a factor 240 and 250.

Two methods of beamsteering the focal lens, namely off-axis and tilted beam steering, were analysed by ray-tracing. The results from these models were verified with experiments, showing that both beamsteering methods were feasible over at least a  $\pm 61 \mu\text{m}$  range.

After considering various alternatives a pan/tilt z kinematics, i.e. a kinematics allowing a translation in the direction of the optical axis and rotations around the two axes perpendicular to the optical axis, was selected. In the design this was realised by using three folded leaf springs connected in parallel to the moving body with the focal lens. The miniature laser scanning head stiffnesses, eigenfrequencies and occurring stresses were analysed.

Eventually the design was realised in the form of a prototype. In this prototype the actuation was realised by three linear voice coil actuators. The displacement was measured by a set of three fibre-optic displacement sensors. This prototype showed a good match with the theory, though some small discrepancies in the stiffness were found, these are most likely attributable to geometric tolerances.

All in all the realised prototype is a proof of concept for a pan/tilt z miniature laser scanning head.

## 5.2 Recommendations

The system could not be fully characterized for the higher frequencies. We would recommend using stronger amplifiers sufficient for further characterisation for the system at higher frequencies. Sensors with a higher resolution with a control bandwidth of 400 Hz should be added

From a control point of view, a decentralised controller or even more complex multivariable controller could be used for realising the final system.

For future designs, of folded leaf springs, the discrepancies between theory FEM, and the realised suspension could be further characterised, in order to understand how geometric tolerances influence the design process. This will allow the design to be further optimised.

Furthermore it is expected that a part of the discrepancies can be reduced by designing a folding tool, allowing the folding of the leaf springs to be done simultaneously to reduce differences between the folded leaf springs.

Also to make assembly of the system easier a tool to align the voice coils with respect to the lens clamp could be designed.





# Appendices

---

## A. Other considered optics

---

### A.1. Reflecting objective

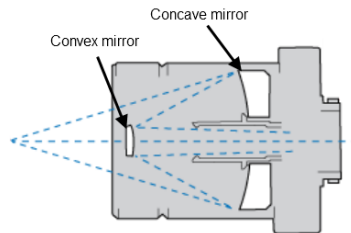


Figure 5.1: reflecting objective, the rays first hit the convex mirror and then reflect on the concave mirror, after which they focus.

The principle of a reflecting objective consists of a concave and a convex mirror. The light passes through a hole in the first concave mirror and afterwards reflects on the convex mirror, after which it reflects on the concave mirror and focuses on a spot outside the objective. The main advantage of such objective is that the light does not travel inside material and thus, retains its temporal characteristics. This option could be advantageous for very short pulses.

This option was rejected, due to the fact that it has a relatively large mass (100 grams). The extension of the femtoprinter towards shorter pulses is not foreseen in an immediate future.

### A.2. Gimbal concave mirror setup

By adding a concave mirror in an optical trajectory under an angle it is possible to create a focused point. A gimbal mechanism could be used to allow the rotation around two perpendicular axes. One of the main issues of this setup is the beam incident angle on the material to be processed. This angle would lead to non-symmetric laser affected zones and would create significant aberrations and losses.

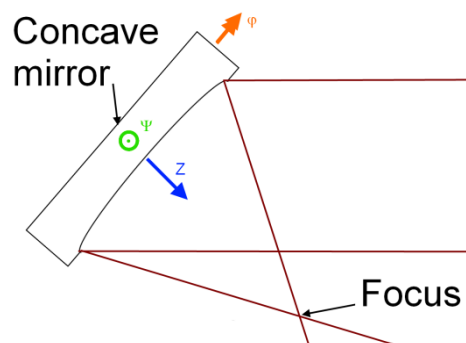


Figure 5.2: Gimbal mirror setup, the mirror can be tilted in  $R_x$  and  $R_y$  to steer the beam across the sample.

### A.3. Concave mirror through material setup

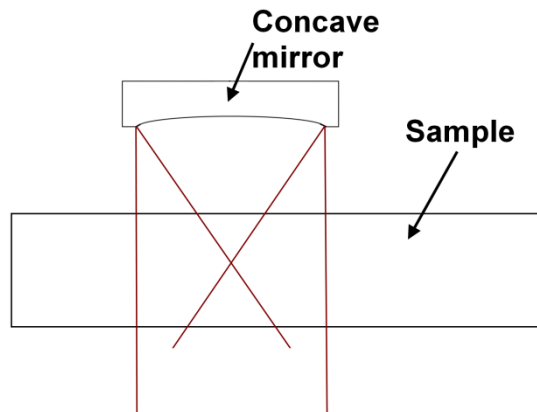


Figure 5.3: concave through material, the beam goes through the sample then hitting the mirror and focussing in the sample.

Another setup is by focusing the laser light through the material. However the beam now still has to pass through another medium than air. Also the beam will be distorted by the locations where the manufacturing process already happened. Also it might be severely harder to implement the optical pathway through the x and y stage, which is below the sample.

#### *Conclusion on concave mirror based solutions*

One of the main problems with all concave mirror-based solution is that there were no commercial aspheric mirrors found of small enough dimensions, to be a viable solution.

### A.4. GRIN lens

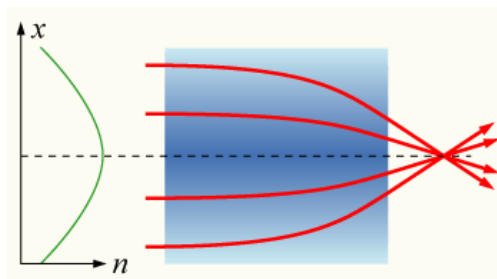


Figure 5.4: GRIN lens, the graph on the left side illustrates the change of refractive index as function of the diameter. Due to a higher index of refraction at the centre of the material the rays focus.

Unlike classical lenses that bend the light wavefronts using geometrical surfaces, GRIN lenses are based on refractive index variation to curve the rays. They are typically very small and have cylindrical shapes. With diameters ranging from 1.8 down to 0.1 mm, they provide a low mass alternative for the current setup. Unfortunately, standard radial grin lenses are not compensated against spherical aberration.

## B. Definitions of optical radii

---

These definitions were based on information from [50], [51] & [52].

### B.1. Airy disk radius

When a perfect lens is irradiated at its aperture with a planar wavefront with uniform intensity distribution, a diffraction pattern forms at its focus point. The pattern consists of a bright central spot surrounded by rings of rapidly diminishing intensity. The diameter of the central spot is known as the Airy disc which radius is defined by:

$$R_{airy} = 1.22\lambda F/\# \quad \text{B.1}$$

The Airy disk corresponds to the ideal case where only diffraction determines the size of the spot. If all the rays are well within the Airy disk, then the system is said to be "diffraction limited".

### B.2. GEO Radius

The GEO spot radius is the distance from the reference point (which is either the chief ray, the centroid of all the rays traced, or the middle of the spot cluster) to the ray which is farthest away from the reference point. In other words, the GEO spot radius is the radius of the circle centred at the reference point which encloses all the rays.

### B.3. RMS Radius

The RMS spot radius is the root-mean-square radial size. The distance between each ray and the reference point is squared, and averaged over all the rays, and then the square root is taken. The RMS spot radius gives a rough idea of the spread of the rays, since it depends upon every ray. The GEO spot radius only gives information about the one ray which is farthest from the reference point.

## C. Derivation of $Z_r(Y_r)$

For the derivation of the rotated lens height ( $Z_r$ ) as function of the rotated Y position ( $Y_r$ ). We start off by rewriting the rotation matrix so that the two unknown variables ( $Y$  and  $Z_r$ ) are on the left hand side and the two known variables ( $Y_r$  and  $Z(Y)$ ) are on the right hand side, as seen in equation C.1.

$$\begin{bmatrix} Y_r - Y_{rc} \\ Z_r - Z_{rc} \end{bmatrix} = \begin{bmatrix} \cos(\alpha) & -\sin(\alpha) \\ \sin(\alpha) & \cos(\alpha) \end{bmatrix} \begin{bmatrix} Y - Y_{rc} \\ Z(Y) - Z_{rc} \end{bmatrix} \rightarrow \begin{bmatrix} Y - Y_{rc} \\ Z_r - Z_{rc} \end{bmatrix} = \begin{bmatrix} \frac{1}{\cos(\alpha)} & \tan(\alpha) \\ \tan(\alpha) & \frac{1}{\cos(\alpha)} \end{bmatrix} \begin{bmatrix} Y_r - Y_{rc} \\ Z - Z_{rc} \end{bmatrix} \quad \text{C.1}$$

From equation C.1., we can write the equation of the Y coordinate as in equation C.2.

$$Y = \frac{Y_r - Y_{rc}}{\cos(\alpha)} + (Z - Z_{rc})\tan(\alpha) + Y_{rc} \quad \text{C.2}$$

If we now go to the definition of the Z profile height and substitute equation C.2, as in equation C.3,

$$Z = -\frac{Y^2}{R_2 \left( 1 + \sqrt{1 - \left( \frac{Y}{R_2} \right)^2} \right)} \rightarrow Z = -\frac{\left( \frac{Y_r - Y_{rc}}{\cos(\alpha)} + (Z - Z_{rc})\tan(\alpha) + Y_{rc} \right)^2}{R_2 \left( 1 + \sqrt{1 - \left( \frac{\frac{Y_r - Y_{rc}}{\cos(\alpha)} + (Z - Z_{rc})\tan(\alpha) + Y_{rc}}{R_2} \right)^2} \right)} \quad \text{C.3}$$

Now solving the equation for Z using Matlab results in equation C.4.

$$\begin{aligned} Z = & \left( -R_2 \cos(\alpha) - Z_{rc} 2 \cos(\alpha) - Y_{rc} \sin(\alpha) - \tan(Y_r - Y_{rc}) \left( \cos(\alpha) (2Y_{rc}(Y_{rc} - Y_r) + \right. \right. \\ & \dots \cos(\alpha) (R_2 + Z_{rc})^2) - Z_{rc} (2R_2 + Z_{rc}) + Y_{rc}^2 \sin(\alpha)^2 + 2Y_{rc} Y_r - 2Y_{rc}^2 - Y_r^2 + \\ & \left. \left. \dots 2 \sin(\alpha) (R_2 + Z_{rc}) (Y_r - Y_{rc} + Y_{rc} \cos(\alpha)) \right)^{\frac{1}{2}} \right) \cos(\alpha) - Z_{rc} \end{aligned} \quad \text{C.4}$$

$$Z_r = \tan(\alpha) (Y_r - Y_{rc}) + \frac{Z - Z_{rc}}{\cos(\alpha)} + Z_{rc} \quad \text{C.5}$$

Equation C.4. is then combined with equation C.5 into equation C.6, creating the desired function  $Z_r(Y_r)$ . Equation C.6 was also verified with the use of a completely defined example.

$$\begin{aligned} Z_r = & Z_{rc} - R_2 \cos(\alpha) - Z_{rc} 2 \cos(\alpha) - Y_{rc} \sin(\alpha) - \left( \cos(\alpha) (2Y_{rc}(Y_{rc} - Y_r) + \right. \\ & \dots \cos(\alpha) (R_2 + Z_{rc})^2) - Z_{rc} (2R_2 + Z_{rc}) + Y_{rc}^2 \sin(\alpha)^2 + 2Y_{rc} Y_r - 2Y_{rc}^2 - Y_r^2 + \\ & \left. \left. \dots 2 \sin(\alpha) (R_2 + Z_{rc}) (Y_r - Y_{rc} + Y_{rc} \cos(\alpha)) \right)^{\frac{1}{2}} \right) \cos(\alpha) - Z_{rc} \end{aligned} \quad \text{C.6}$$

## D. Measurement results

### D.1. Translational tests with smaller NA

This appendix discusses the results obtained from the CMOS measurements in Lausanne.

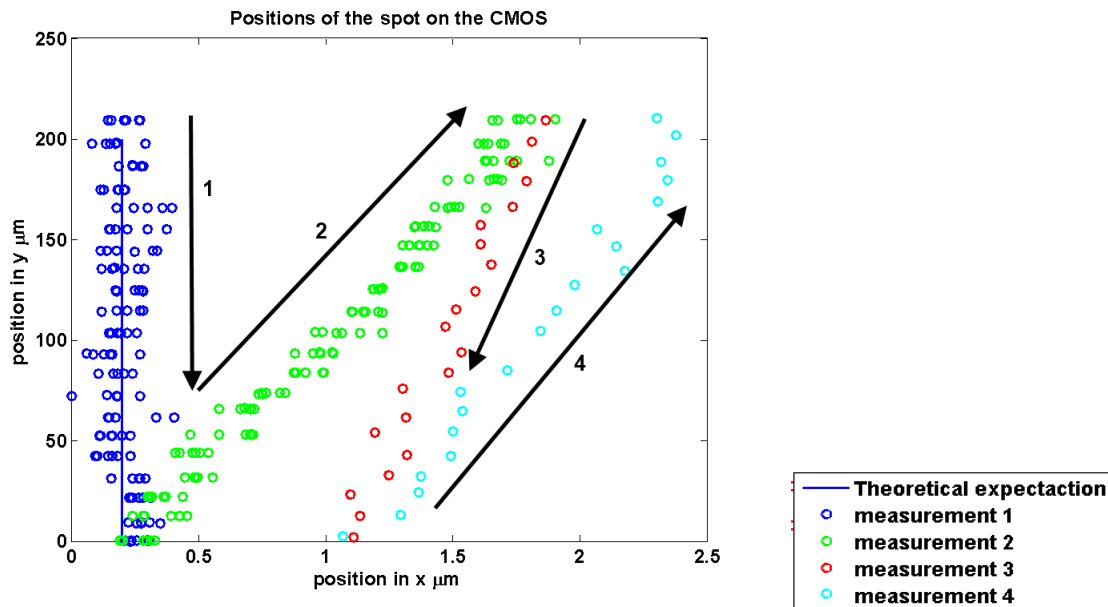


Figure 5.5: The translational tests, the test consisted of four consecutive measurements (indicated by direction and measurement no. in the figure), of which the first two took 6 measurements per interval. From this figure one can see that an applied displacement of 200  $\mu\text{m}$  to the lens roughly equals the expected translation of 200  $\mu\text{m}$  of the spot.

From figure 5.8 we observe that the system roughly travels the expected prescribed displacement with only a small discrepancy of 10  $\mu\text{m}$ . The parasitic translation in x is attributed to hysteresis caused between the ball bearings and the moving stage.

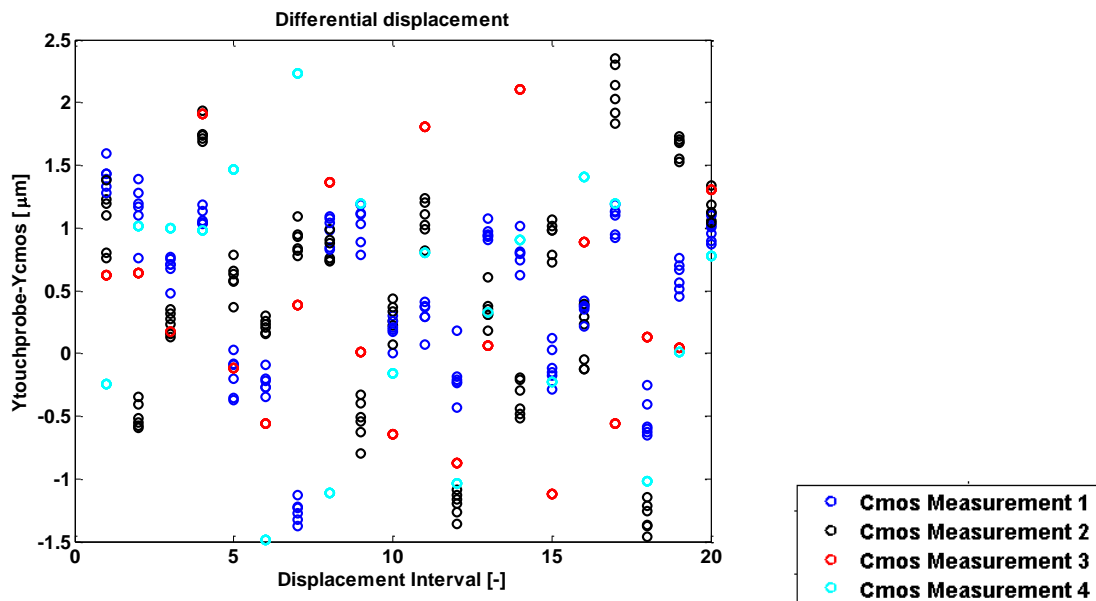


Figure 5.6: differential displacement of the and CMOS touchprobe

When looking at the differential displacement between the CMOS and the touch probe in Y direction, we can see roughly a volley of shots with  $\pm 2 \mu\text{m}$ . This indicates even further that the applied displacement is the translation per spot as the uncertainty of the touchprobe is also  $\pm 2 \mu\text{m}$ .

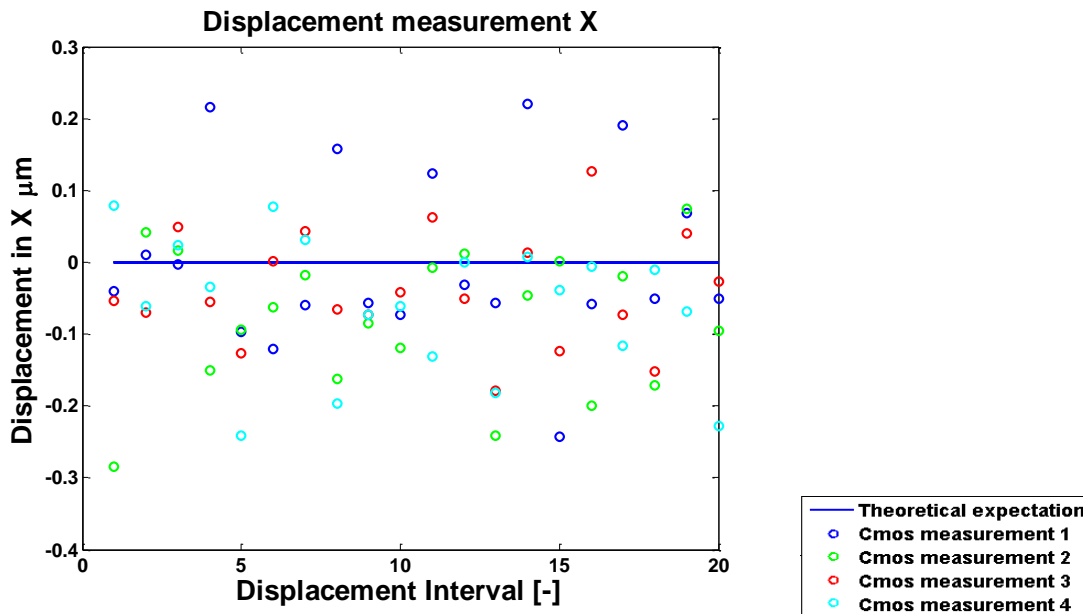


Figure 5.7: relative displacement in X direction

The relative displacement in x is a volley of shots where especially for the 2<sup>nd</sup> and 4<sup>th</sup> measurement these have an average around  $-0.1 \mu\text{m}$ . Indicative for the expected hysteresis loop.

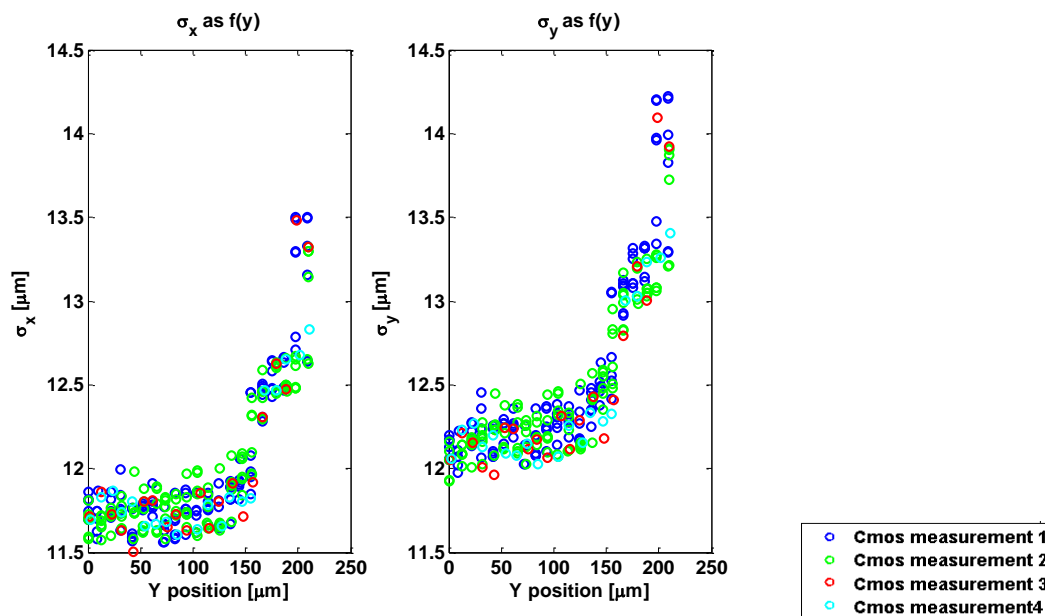


Figure 5.8: Standard deviation in x and y direction

The standard deviation of the beam diameter is plotted in figure 5.8, it shows that the further of axis the spot goes, the larger the spot becomes.



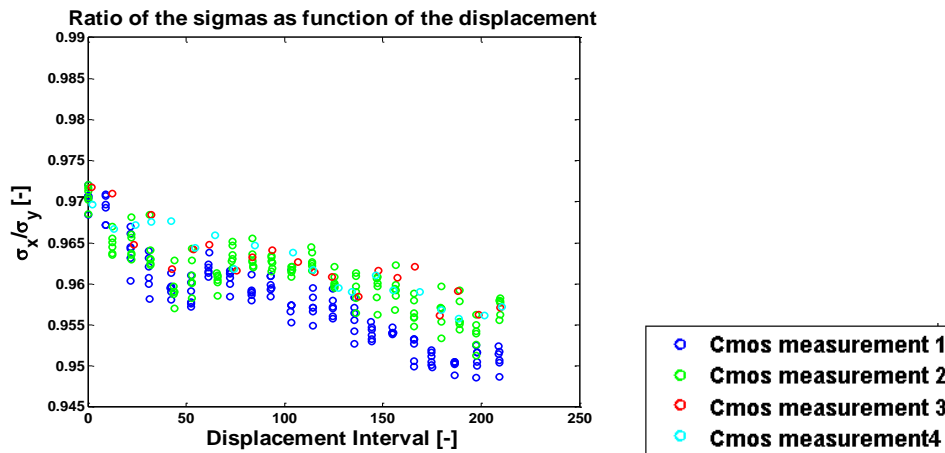


Figure 5.9: Beam elipsoidicity

As for the beam elipsoidicity it is observed that the further off axis the measurements are done the more elipsoidal the gaussian profile becomes.

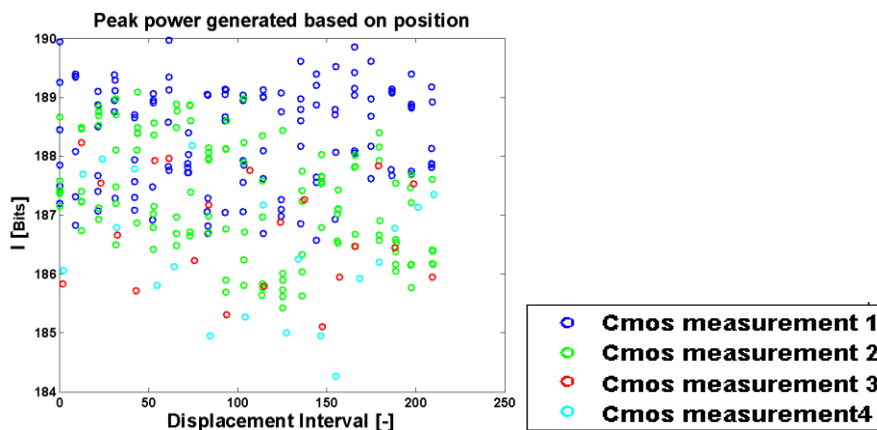


Figure 5.10: Peak power generated based on position

The peak power showed a decrease in each significant measurement round, but still the averages of the measurement rounds are very close to each other.

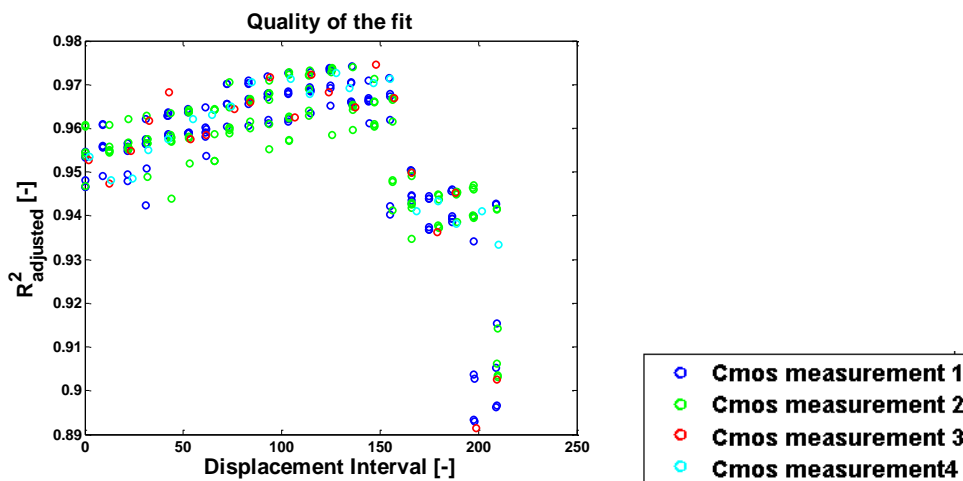


Figure 5.11: R2 adjusted

The quality of the fit showed a relatively good fit over a large part of the range, but the larger the displacement the worse the fit became, indicating what one would expect namely the Gaussian beam becoming more distorted.

## D.2. Translation With larger NA

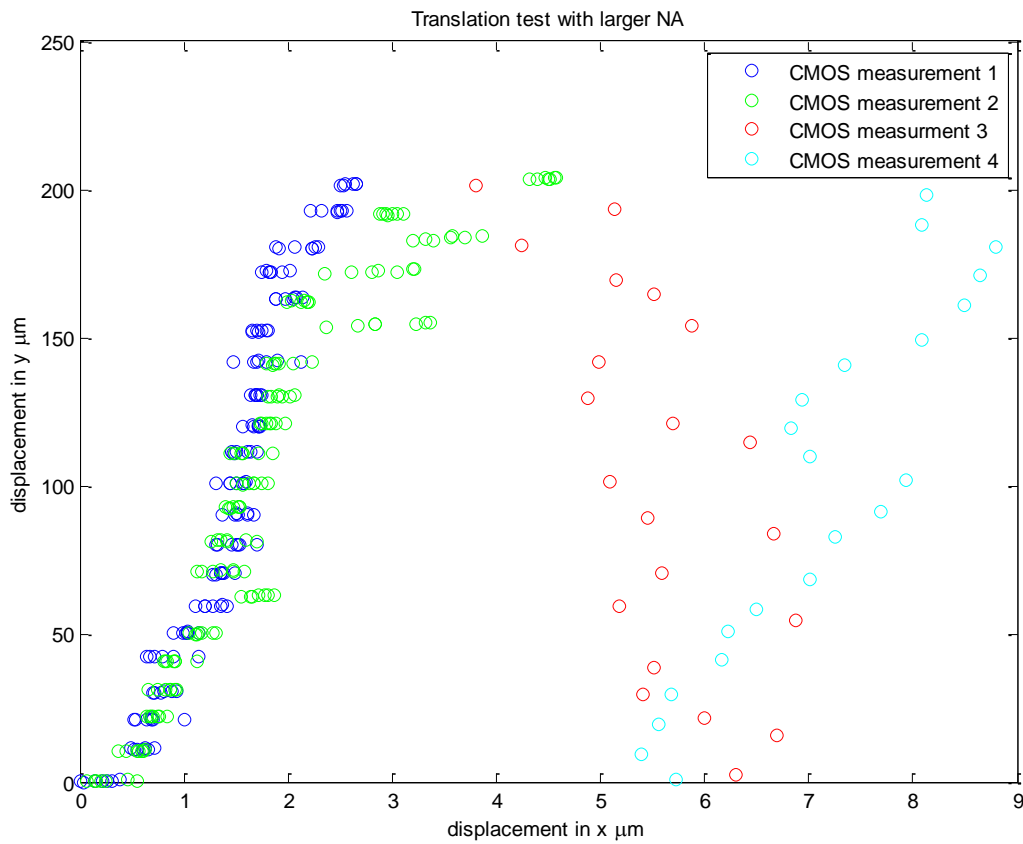


Figure 5.12: spot displacement as function of translation.

With the larger NA, it could be seen that the movement roughly equalled the applied 200  $\mu\text{m}$ , though the displacements in x are slightly larger than with the lower NA this will most likely be caused by alignment with respect to the CMOS.

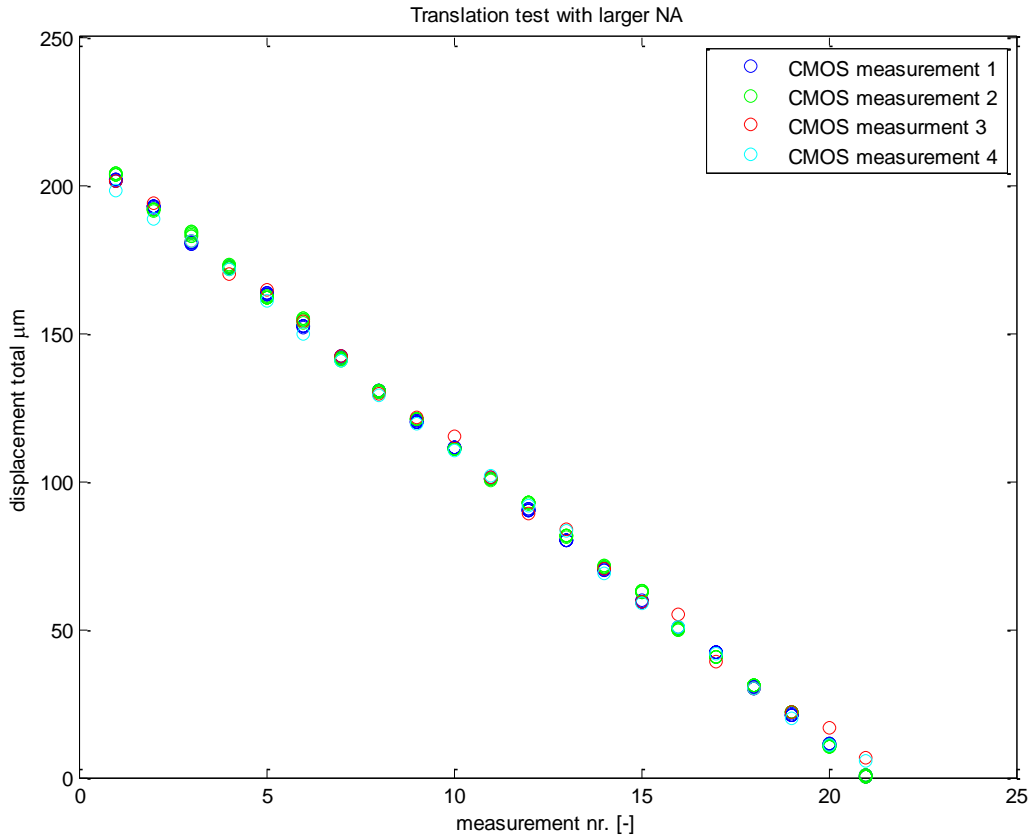


Figure 5.13: total displacement as function of the measurement nr.

When examining the displacement we still see that the total travelled displacement is still about 200µm, this indicates even more that the predicted models equal the practical measurements.

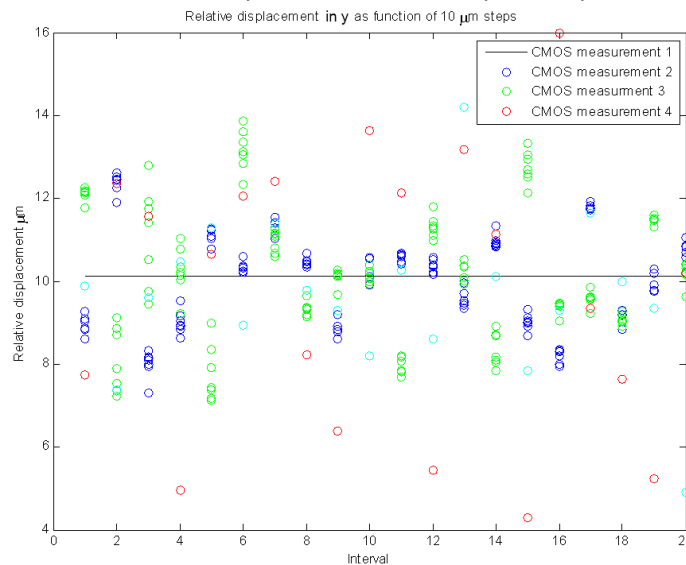


Figure 5.14: relative displacement in Y as function of 10 µm

When looking at the relative displacement which occurs in the Y the average of the expected displacement, is what one would expect the 10 µm, though the deviations seem larger they were still within a ±2µm range from the touch probe measurements.

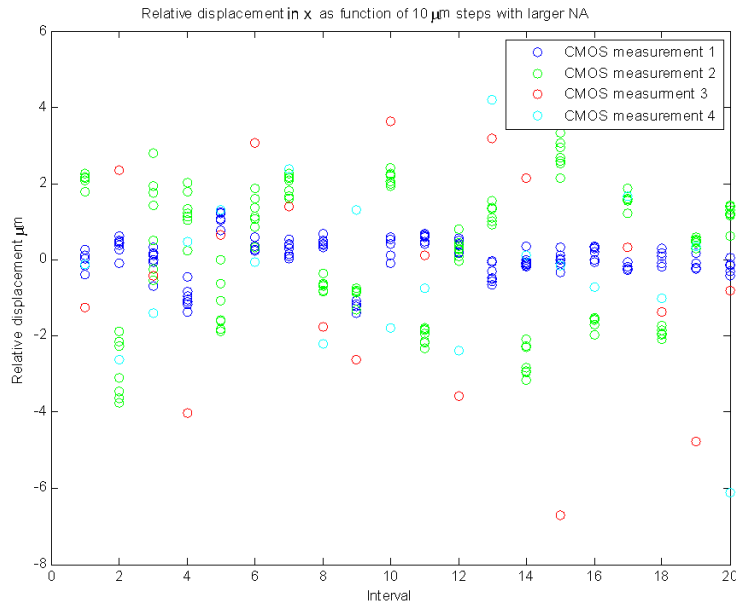


Figure 5.15 Relative displacement in X as function of 10 μm steps

The x displacements seem to be a volley of shots around 0 μm, as for the large displacement in the third measurement these correlate with the larger peak intensity variations, indicating less trustworthy measurement results.

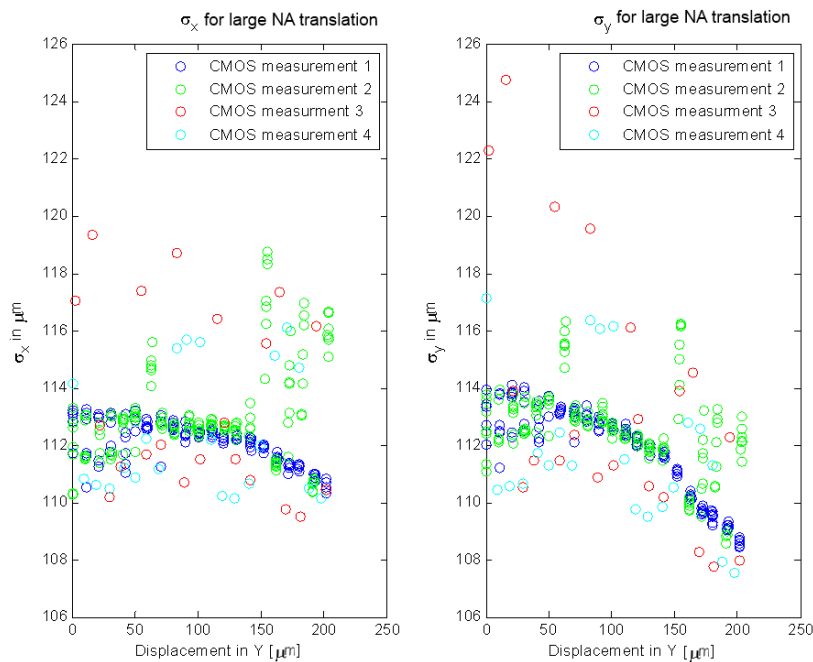


Figure 5.16: Standard deviations of the spot as function of displacement

What we observe in the standard deviations is a steady decline with increased travel distance. As for the larger variations these correlate directly with larger peak intensities of the laser.

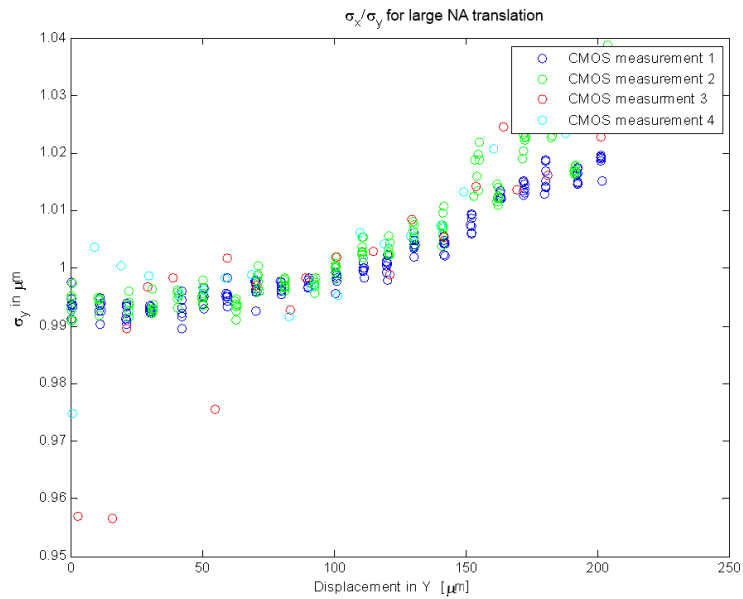


Figure 5.17: Beam ellipsoidicity as function of translation

We observe that the further we translate the more ellipsoidal the beam becomes, but the ellipsoidicity over the 200µm is still not a critical disturbance for the Gaussian beam profile

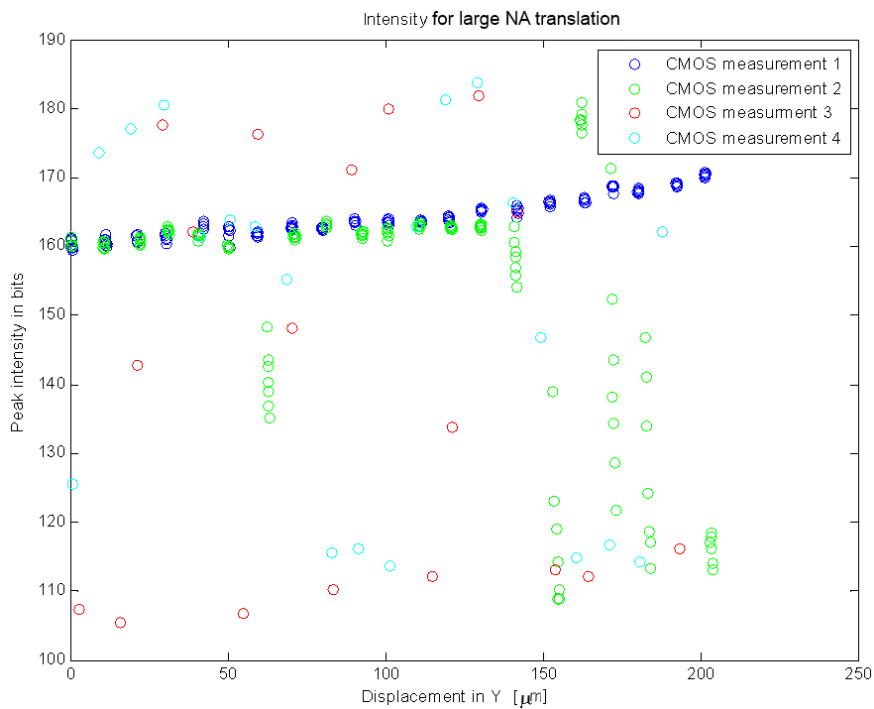


Figure 5.18: the peak intensity for large NA translation.

Basically we see from the figure above that starting from the last half of the 2<sup>nd</sup> measurement the laser started to fluctuate in intensity, this had its results on the other measurement data, as previously stated.

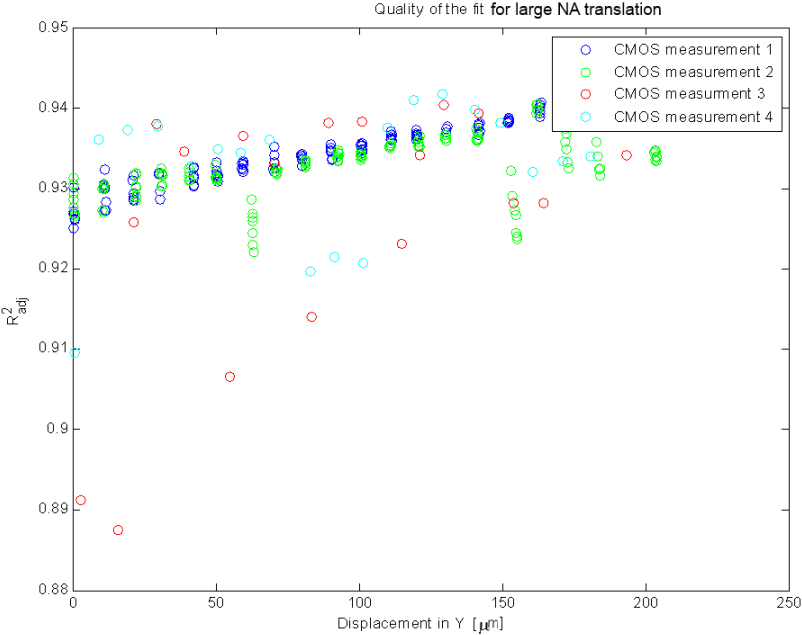


Figure 5.19: Quality of the fit as function of translation in Y

The  $R^2_{adjusted}$  for a large NA translation are still relatively good, indicating that the Gaussian beam is not distorted that much by applying a translation with the lens. Summarizing everything the lens translations are feasible over 200  $\mu\text{m}$  range.

### D.3. Rotation with smaller NA

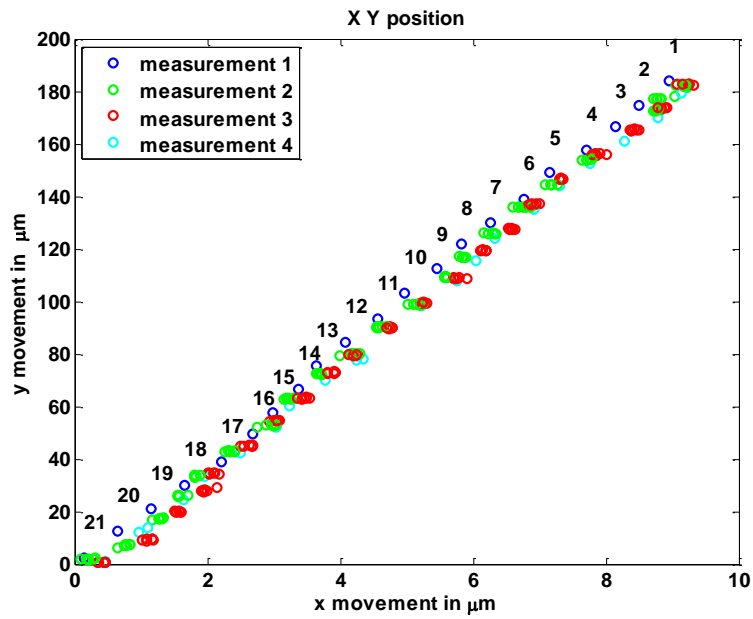


Figure 5.20: X and y position as function of rotation

The total Y displacement for a small NA is about 180  $\mu$ m and the x is about 9  $\mu$ m. The exact rotation axis is not aligned with the CMOS chip.

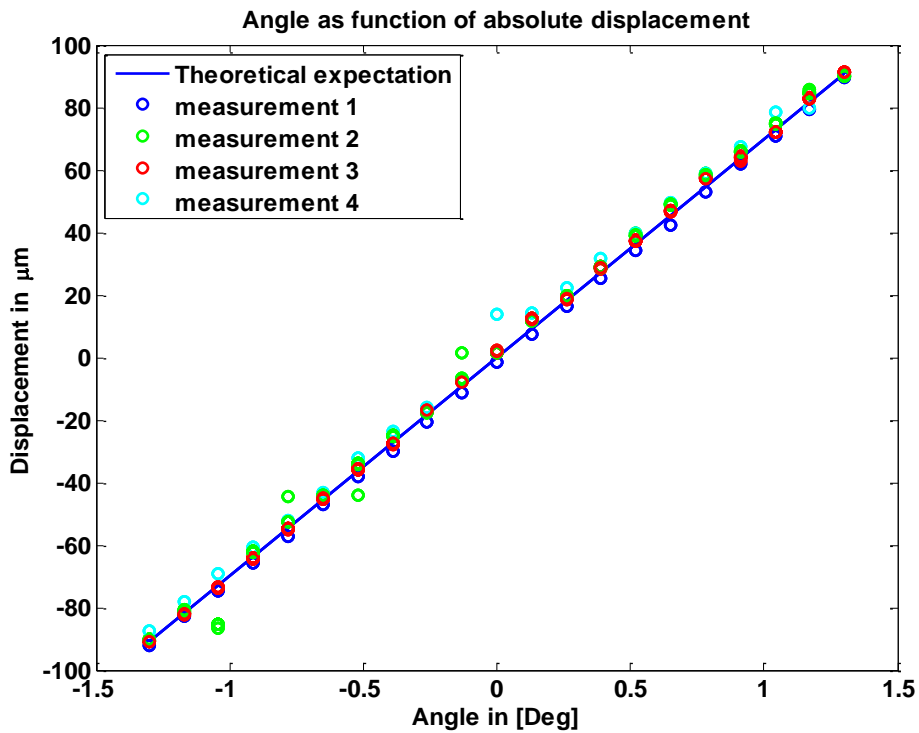


Figure 5.21: the displacement plotted against the applied angle

We can clearly see a correlation between the angle and displacement; also we can see that a  $\pm 90 \mu$ m movement is feasible with the present lens at Low NA.

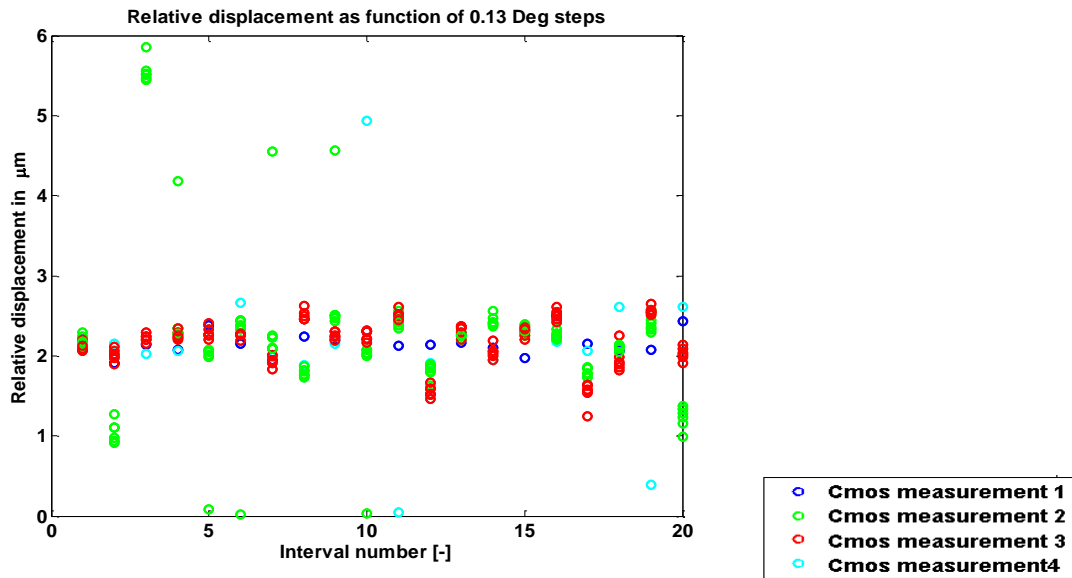


Figure 5.22: the relative displacement per 0.13 Deg step

The relative displacement per 0.13 Deg step is about 2μm this seems to be relatively and has less variation then with the y displacements.

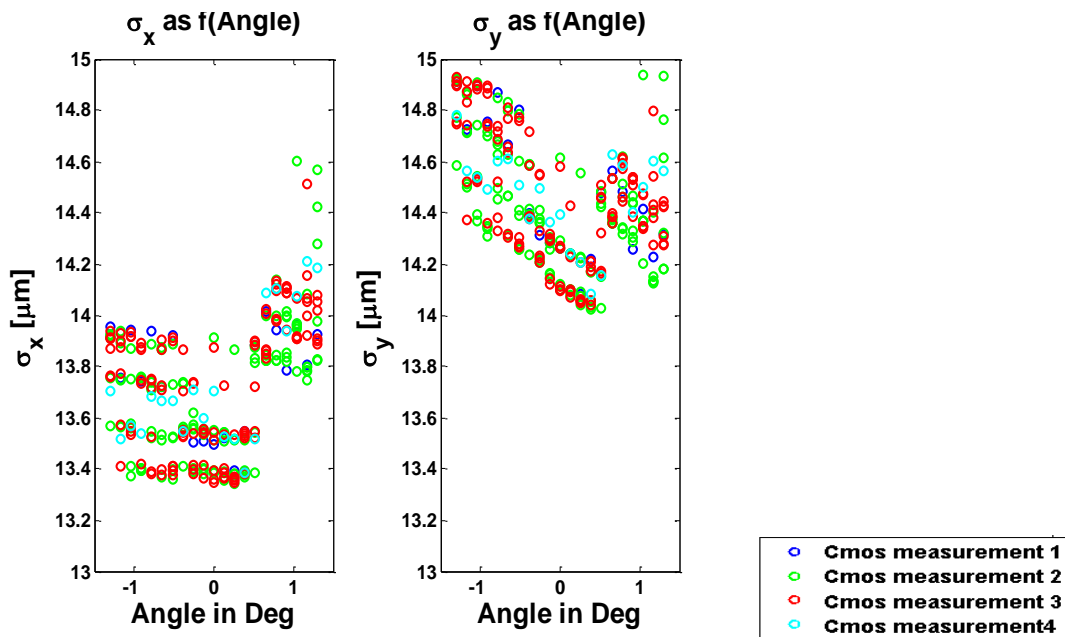


Figure 5.23: the standard deviations of the beam.

Looking at the standard deviations of the beam we can see that they are within relatively the same band gap, and the difference between the two becomes less for the higher angle.



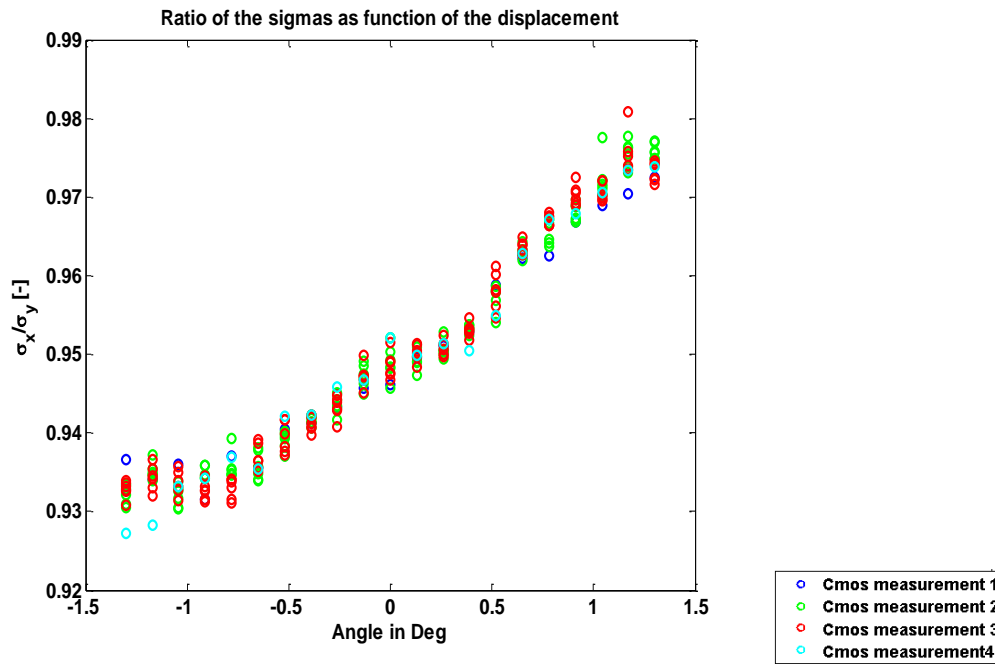


Figure 5.24: Beam elipsoidicty as a function of movement.

As already visible for the standard deviations the elipsoidicty became less for larger angles, this can be explained by the beam not being aligned with the perfect centre of the lens at the 0 Deg angle.

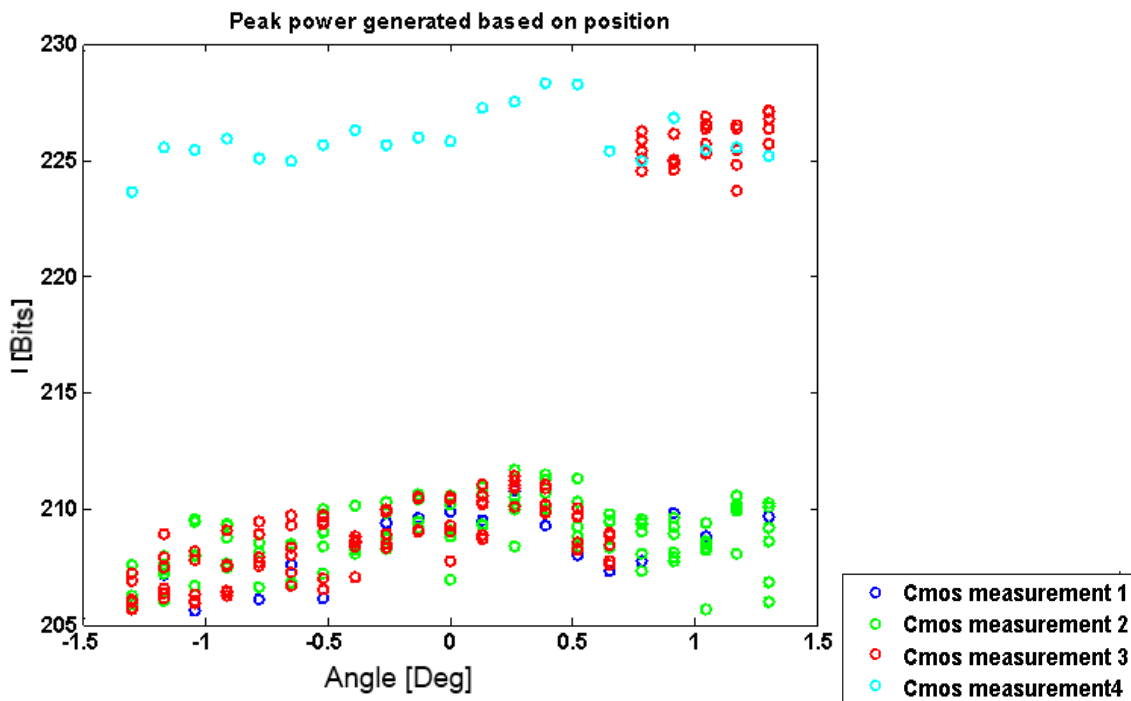


Figure 5.25: Peak power per angle

What we can see is that during the 3<sup>th</sup> and 4<sup>th</sup> measurement there was a relatively large discrepancy, which was most likely caused by laser instability. However, the separate measurements are relatively stable.

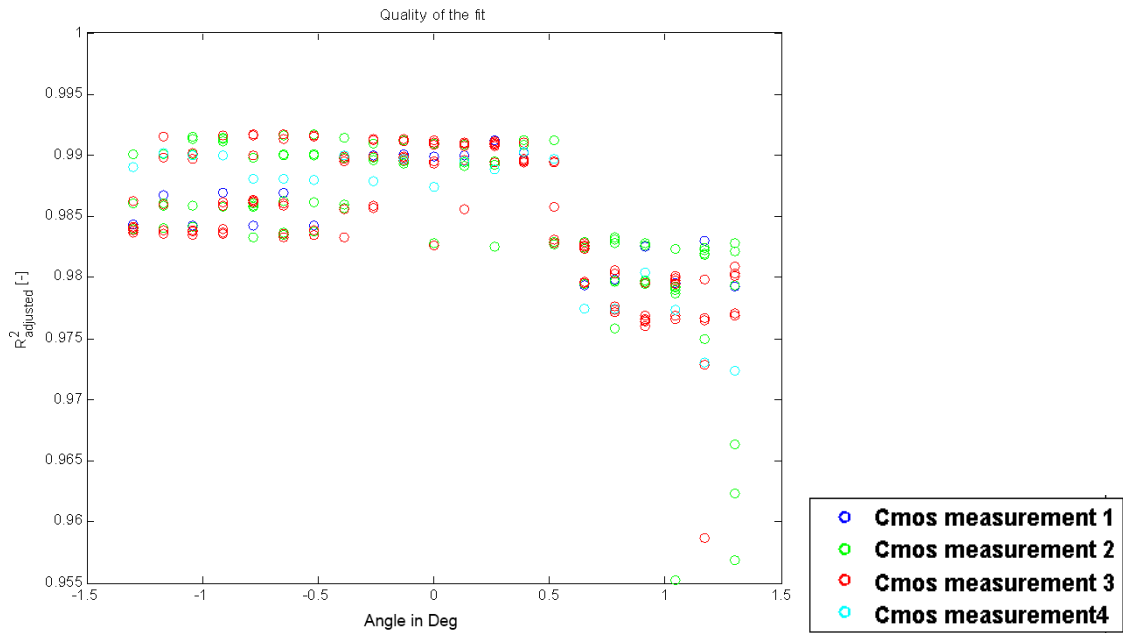


Figure 5.26: The  $R^2_{\text{adjusted}}$  as function of the angle

We can see that over the entire range the  $R^2_{\text{adjusted}}$  has a relatively good fit over the data, implying that rotation can be done without distorting the Gaussian beam shape.

#### D.4. Rotation With larger NA

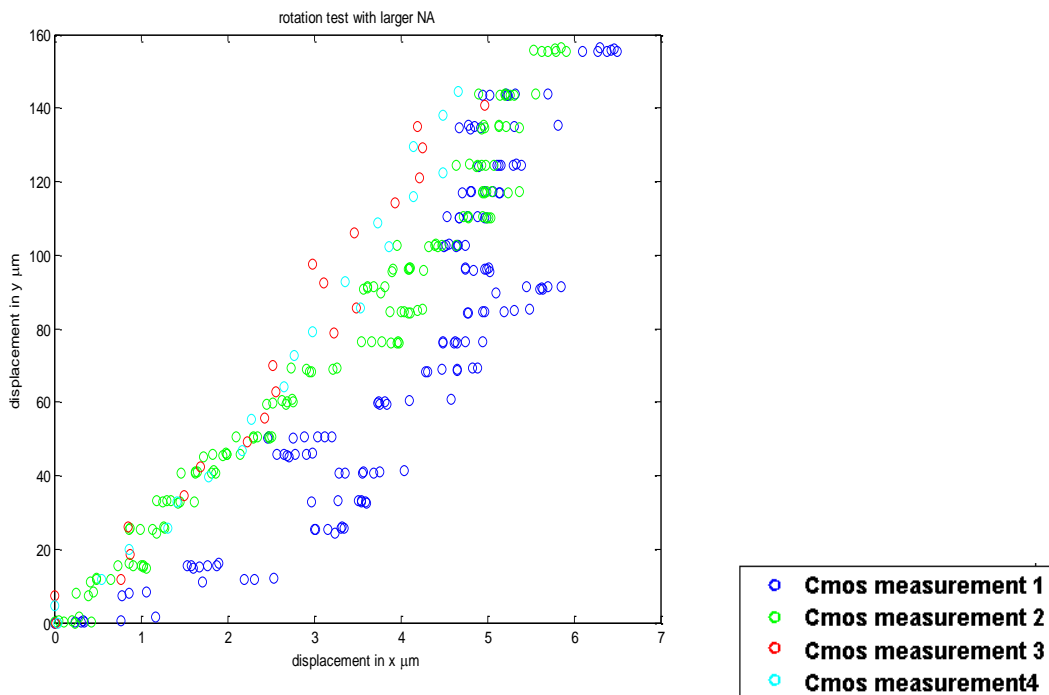


Figure 5.27: the realised x and Y displacement realised with a rotation

With the larger rotation we see that we achieve a displacement of about 140  $\mu\text{m}$  over the entire range and a displacement of 6  $\mu\text{m}$  in x.

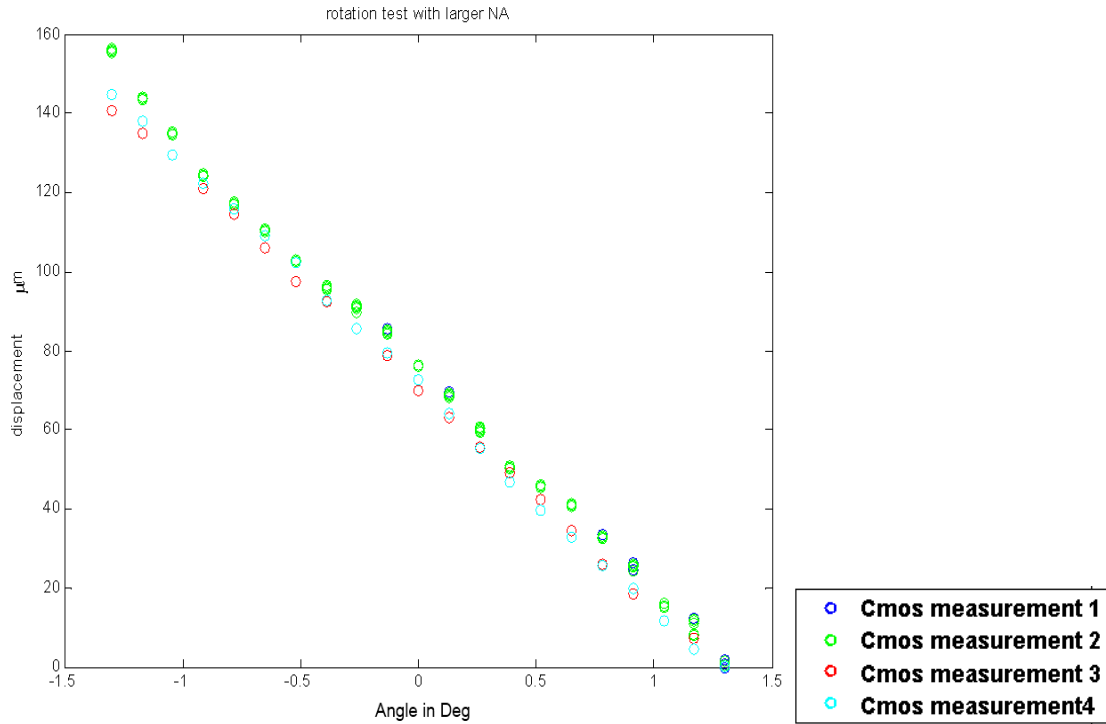


Figure 5.28: displacement as function of angle

We can see that the achieved displacement is about 140  $\mu\text{m}$  over the entire range.

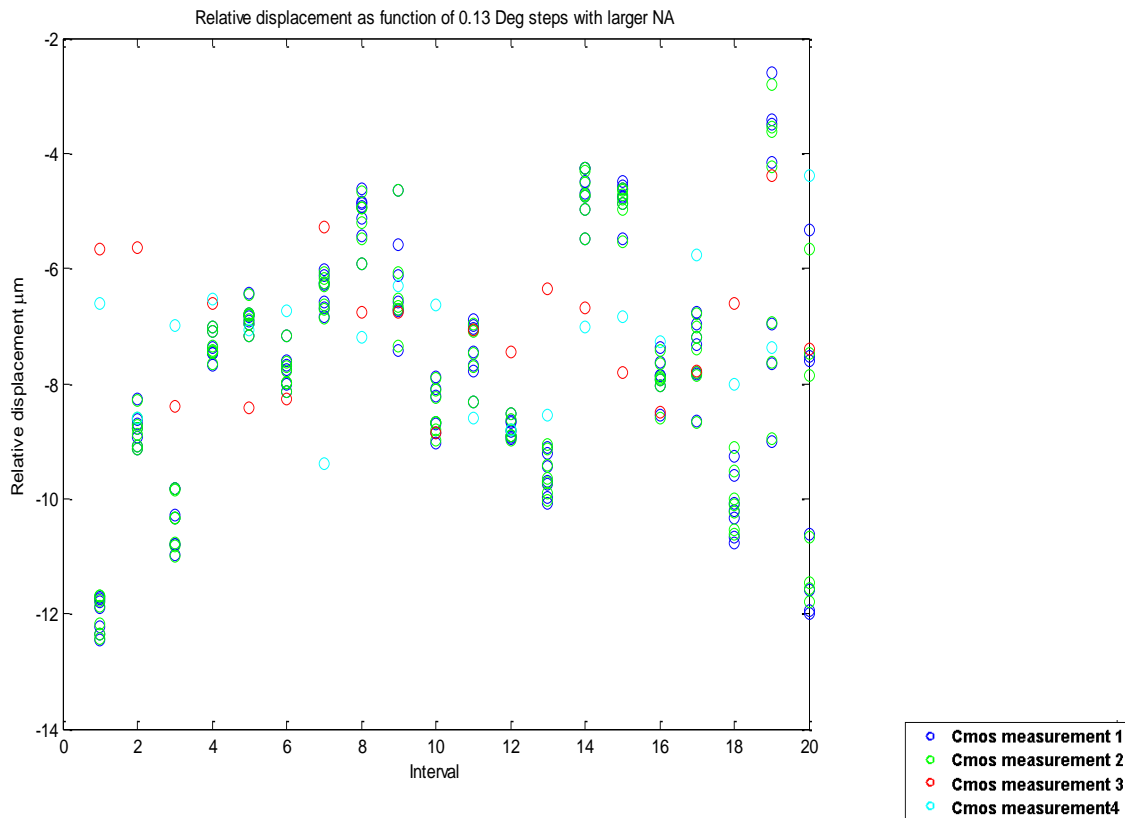


Figure 5.29: displacement of the spot in  $\mu$  as function for the interval

The average displacement for the angular steps is about -7  $\mu\text{m}$ .

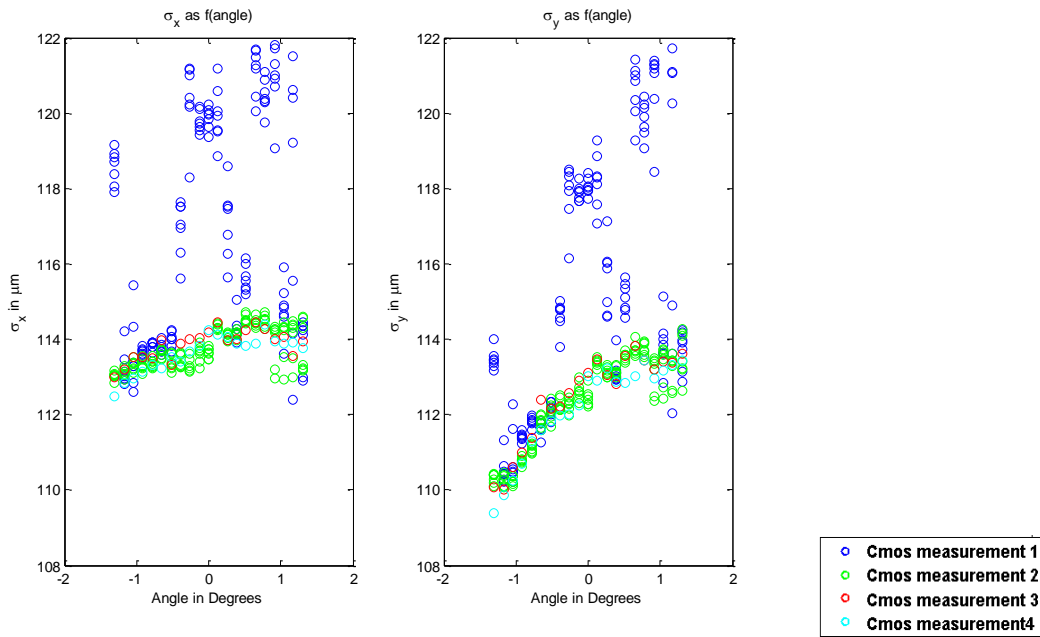


Figure 5.30: the standard deviation as function of the angle

We basically see that the spot size is about 112 μm.

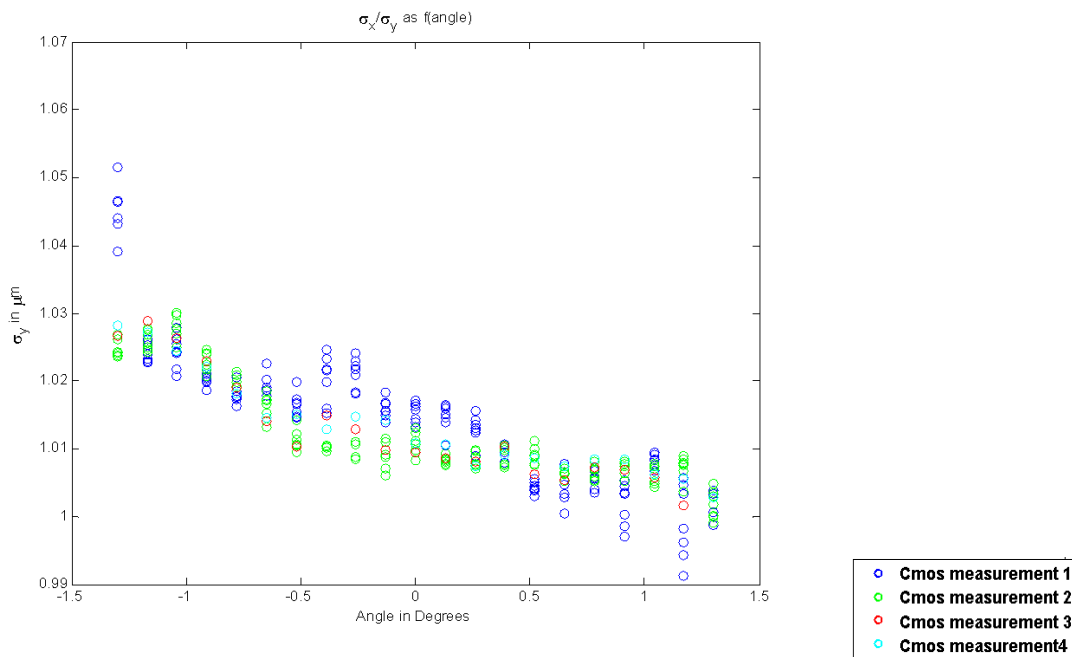
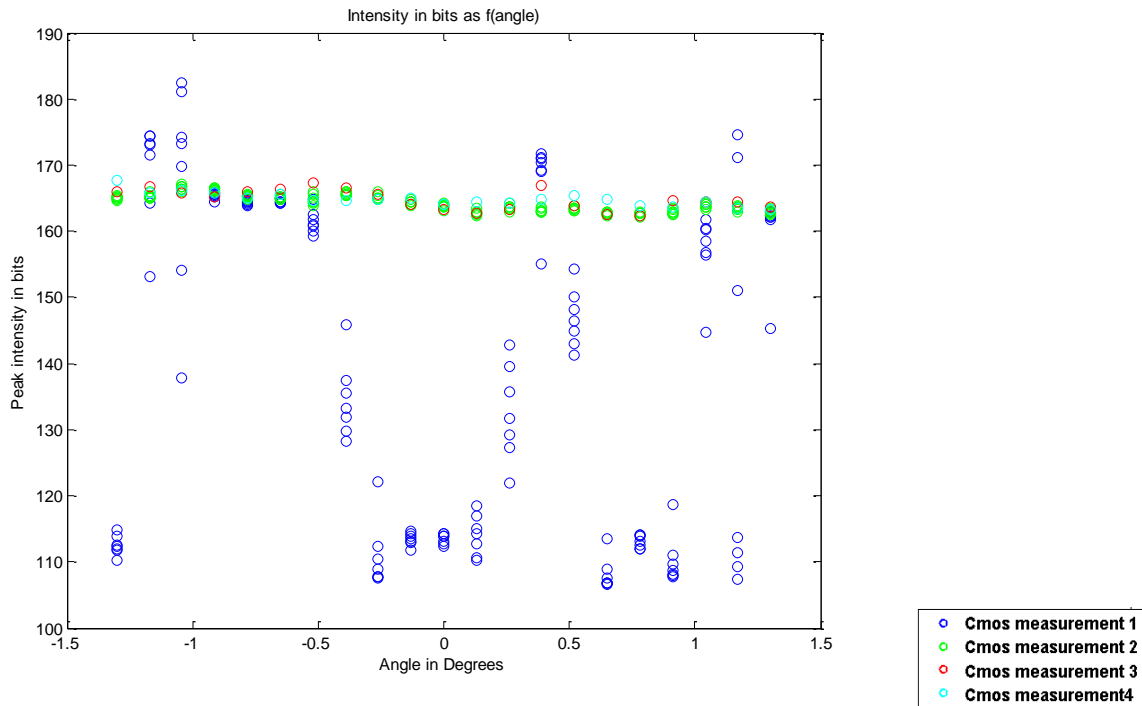


Figure 5.31: Beam ellipsoidicity as a function of the angle

We can see that over the applied angular range the ellipsoidicity improves the larger the angle becomes.



From the intensity plot we can see that especially the 1<sup>st</sup> measurement set had large variations in the intensity, after this set the intensity stabilised on one level. These larger variations are also observed in the other parameters.

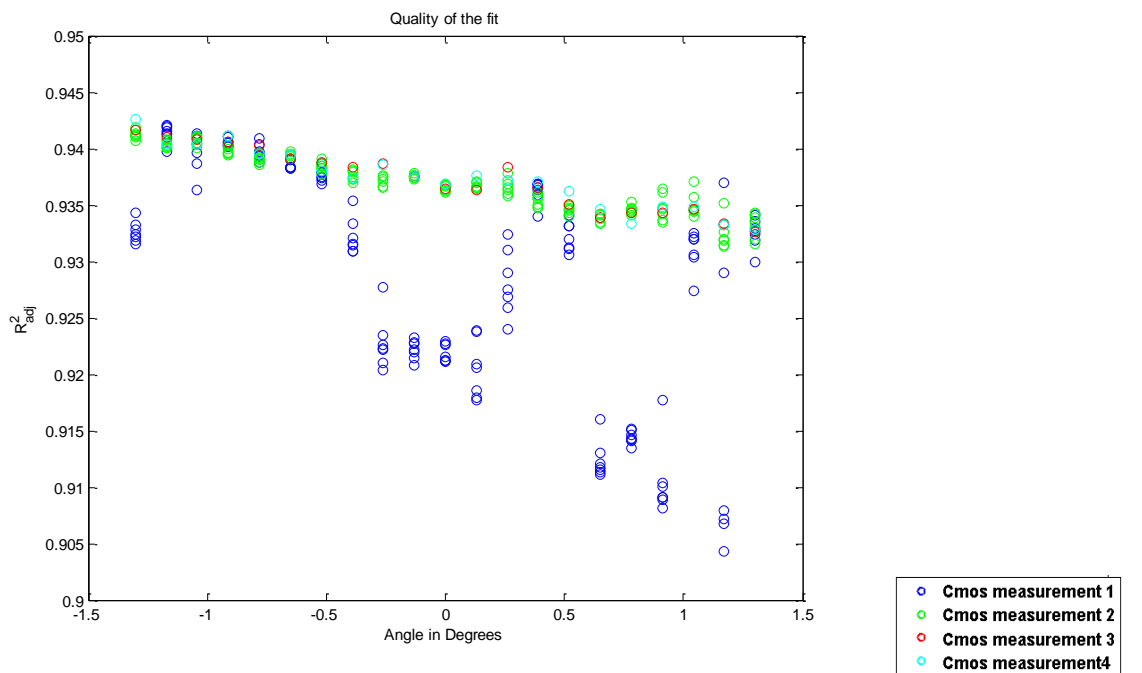


Figure 5.32: the R<sup>2</sup> adjusted as a function of the angle in Degrees

From the R<sup>2</sup><sub>adj</sub> we can see that over the entire range we have a relatively good behaviour, the fluctuations in the intensity are noticeable in the first measurements quality of fit. But besides that all values seem higher than 0.93, which implies that rotation is a feasible option over ±1.35 Deg range

## E. Additional kinematics concepts

### E.1. Concept1: Rotational bar mechanisms

A rotational concept which was thought off, displayed in figure 5.33, was a set off bars coupled in parallel to a body which is in the centres has a lens, by either translating the bars over a distance a tilt would be applied to the centre of the lens. Though this solution was parallel, it was considered relatively complex.

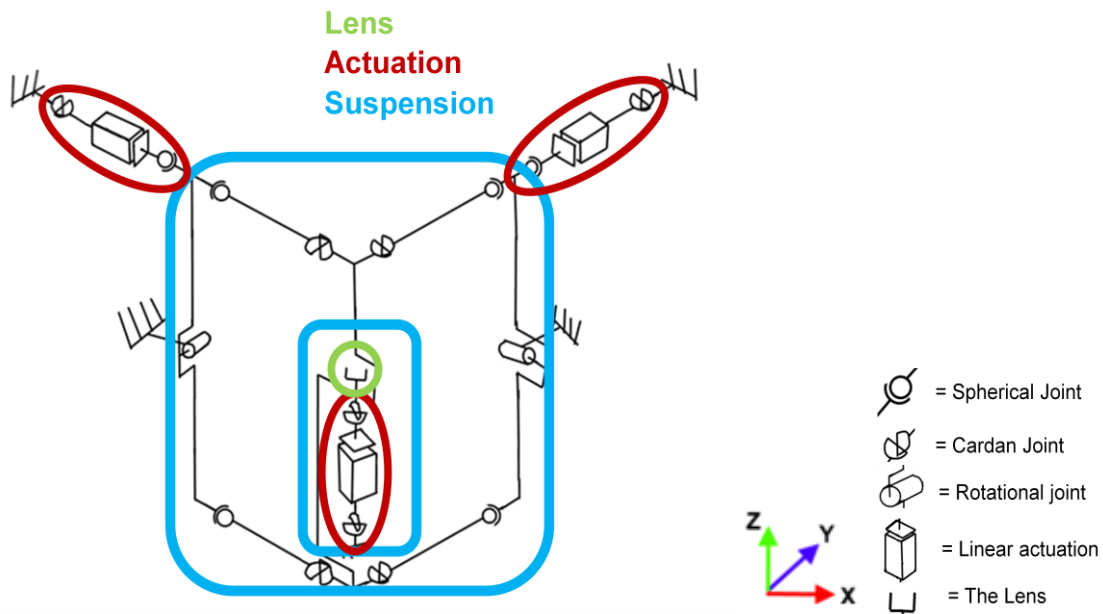


Figure 5.33: Rotational bar mechanism

### E.2. Concept 2: cardan mechanism with z-drive

Another option which was considered was a cardan with a Z drive as displayed in the figure below. Though the concept is relatively simple, it is a chain of serial stiffnesses which will be less optimal for high eigenfrequencies.

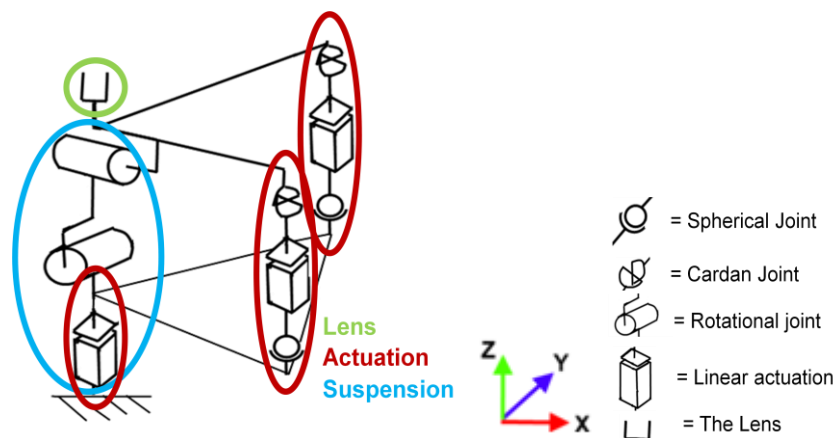


Figure 5.34: Cardan with z mechanism

### E.3. Concept3: Hybrid suspension, parasitic rotation and translation.

Concept 3 consisted of a translational mechanism with parasitic rotation, though this concept does not have a Z mechanism in it, it would combine a tilt and displacement in a parallel matter. Due to not having parallel Lens Z drive option this option was considered less useful.

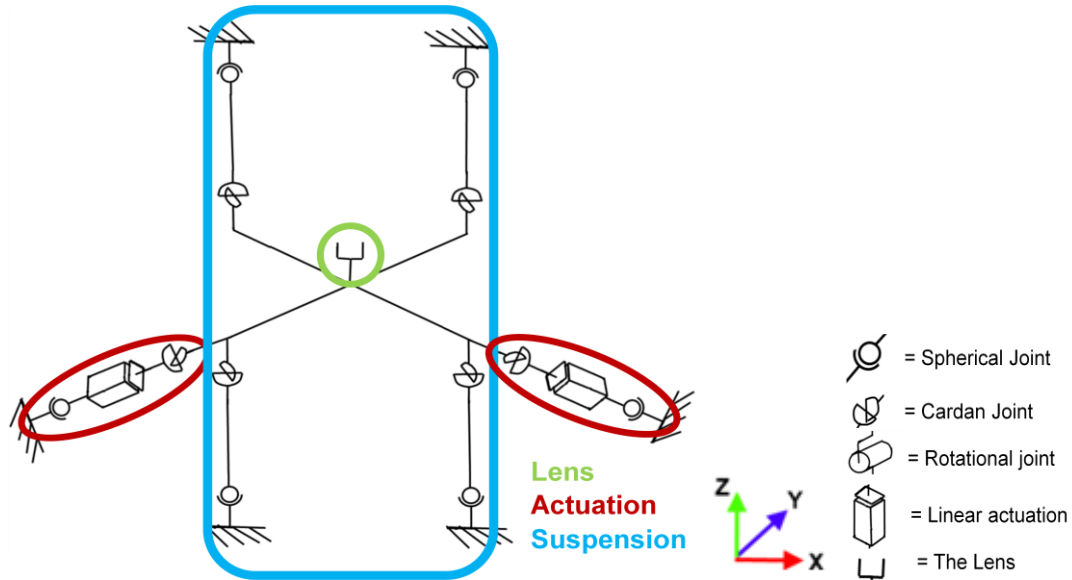


Figure 5.35 translation with parasitic rotation

### E.4. Concept4: Double Roberts mechanism.

The last option which was considered was a double Roberts mechanism, having a rotational centre outside of the mechanism. This structure was relatively complex, and having a rotational centre outside the mechanism, did not serve any purpose. Also this option did not yet have a parallel Z actuation.

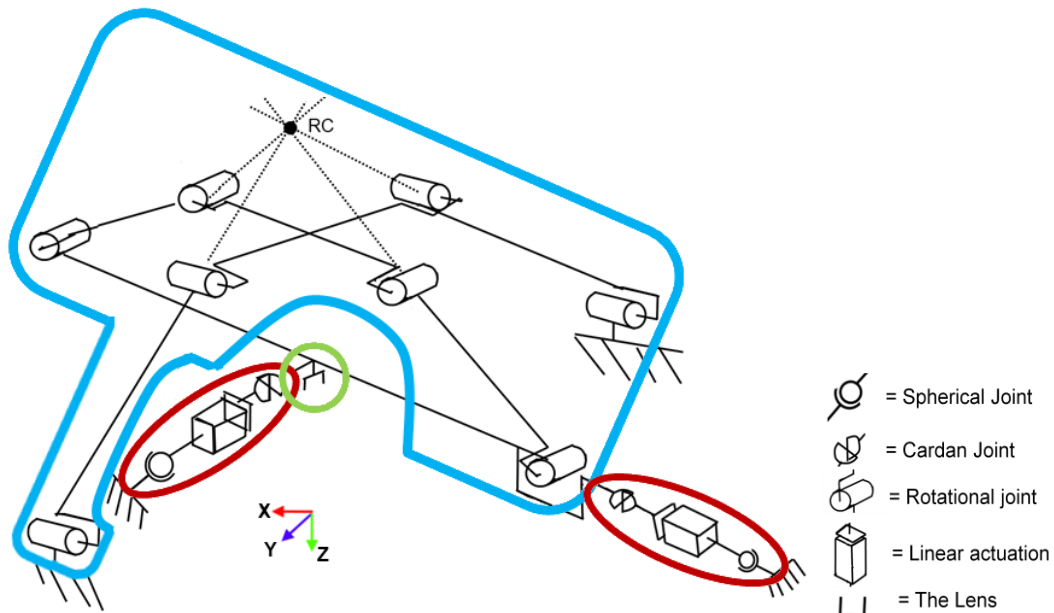


Figure 5.36: Double Roberts mechanism

## F. Mechanical Drawings

### F.1. Parts list

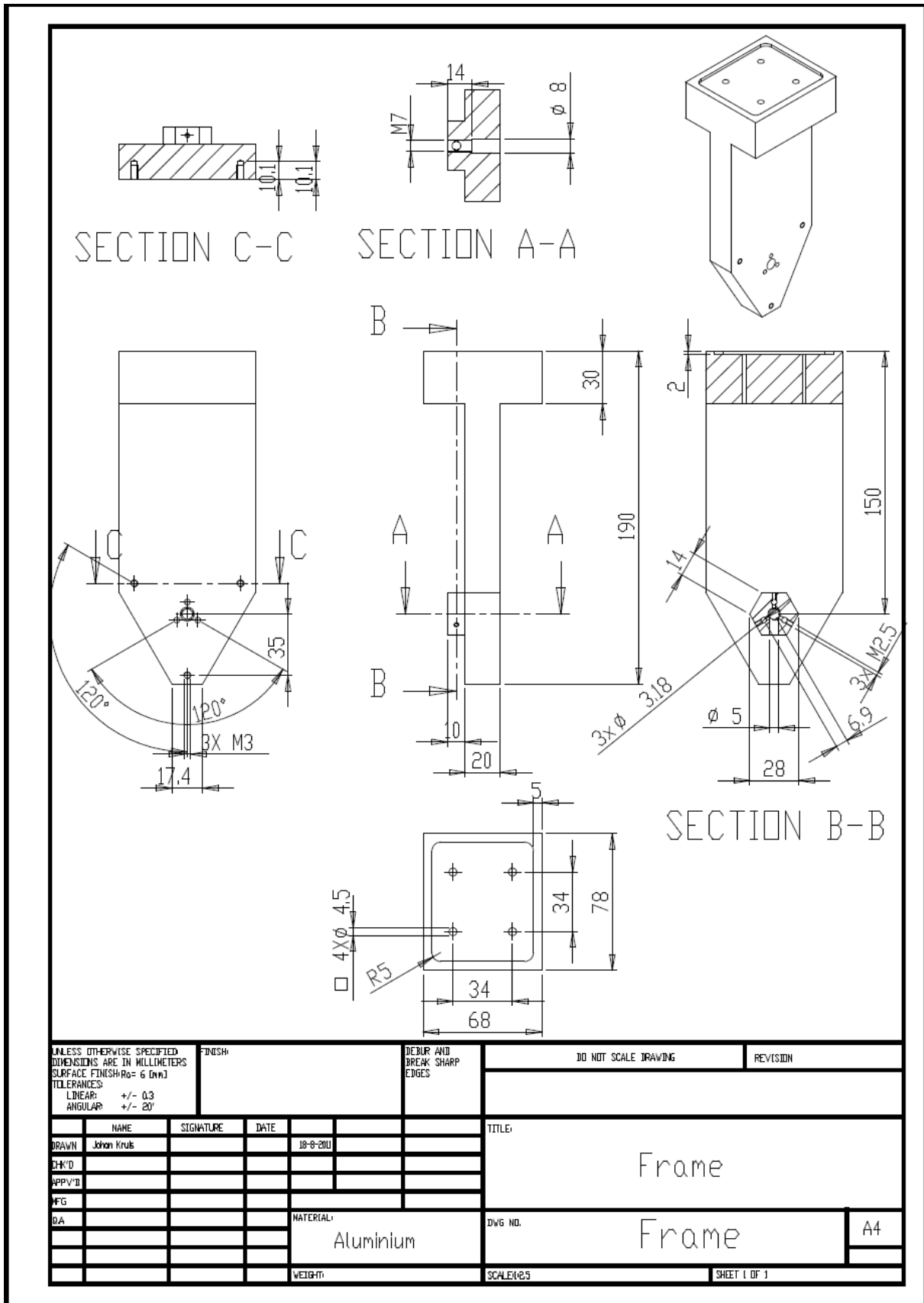
Part name	Function(s)	Produced by	Required No.
Frame	Z-stage connection. (4x M4) Clamping of the sensors. (3x M2.5 of M3 (Polymer)) Actuator&leafspring Mount connection.(3x M4)	GTD	1x
Actuator&leafspring Mount (A/L Mount)	Fastening the actuators or the actuator filling plate (9x M2) Fastening the leaf springs or their filling plates (6x M2)	GTD	1x
Leaf spring filling plates (L filling)	2mm filling plates for usage of the 15 by 15 folded, for the folded leaf springs	GTD	3x
Actuator filling plate (A filling)	2mm filling plates for usage of the 15 by 15 folded, for the actuators	GTD	1x
Folded leaf spring Membranes	Stiffness of the suspension	Novateck	21x
Leaf spring clamps (L clamp)	Clamping the leafspring	GTD	3x
Membraneclamp_down (M clamp d)	Connecting the actuators to the membrane (6x 1#-72)	GTD	1x
Membraneclamp_up (M clamp u)	Clamping the membrane to the membraneclamp_down (6x M2) Holding the lens with UV cured glue	GTD	1x
Lens	352350-C asphere	Thorlabs	1x
Shielding tube	Shielding the sensor cables from the laser light	GTD	1x
Filling Block	Filling up on the x/y stage so that the sample can be manufactured in the focal range. 40 mm	GTD	1x
Sensors	Philtec displacement sensors D64-EQ	Philtec	3x
Actuators	La05-05-000A	BEI Kimco	3x
DAQs	TUEDacs, borrowed from control engineering group.	TUEDACs	2x

#### List of bolts

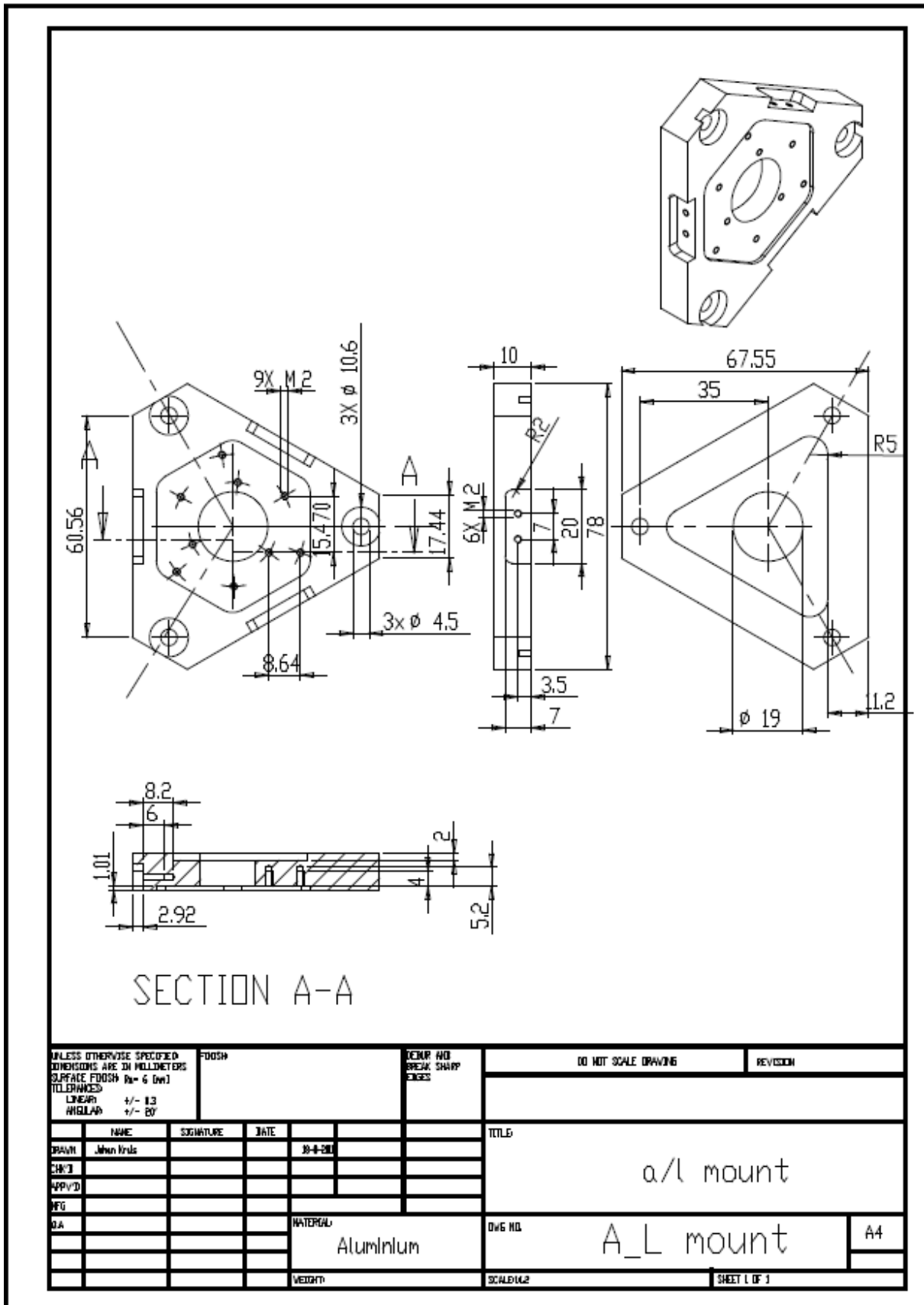
Bolt type	Length	Locations	Number
M4	35- 40 mm	Frame to Z-stage	4x+2x
	10 -14 mm	Frame to l/a mount	3x+2x
M2.5	5 mm	Frame to sensors	3x+2x
M2	12-15 mm	l/a stage to leaf springs	6x+ 2x
	5-7 mm	l/a stage to actuators	9x+2x
	3-5 mm	Membraneclamp_u to Membranclamp_d	6x+2x
1#-72	0.25 inch	Actuator to Membraneclamp_d	6x+2x



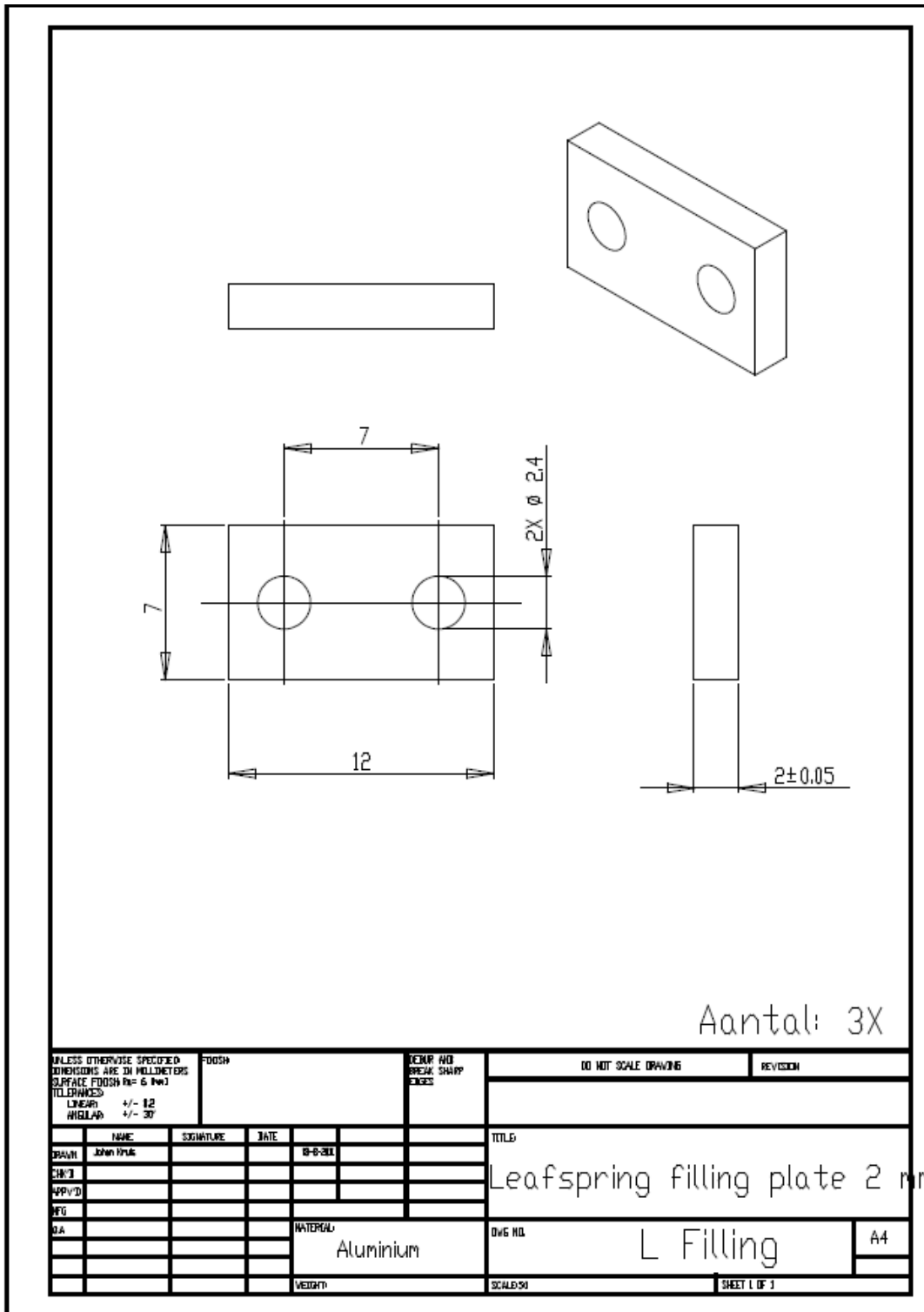
F.2. Frame



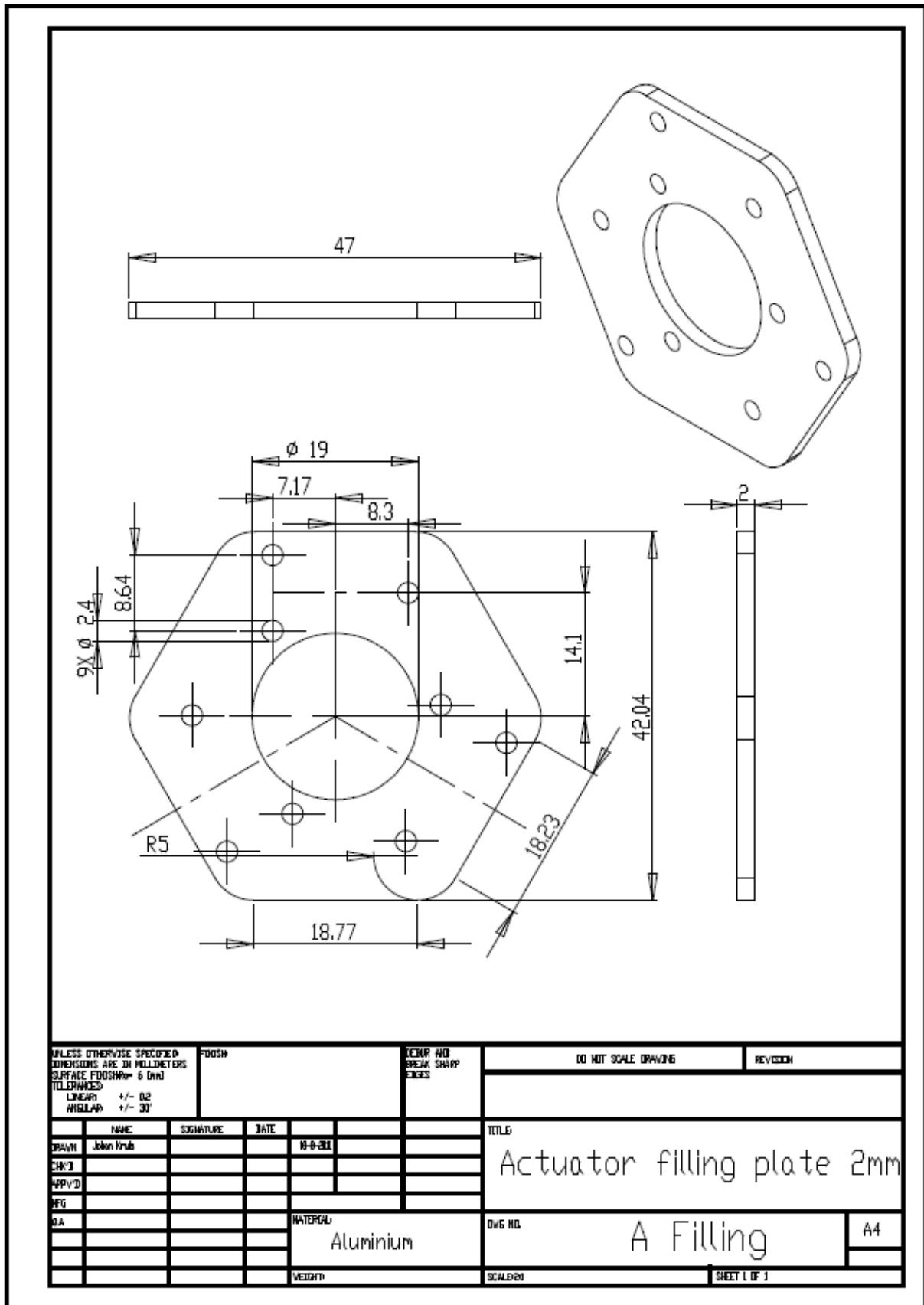
F.3. Actuator leaf spring mount



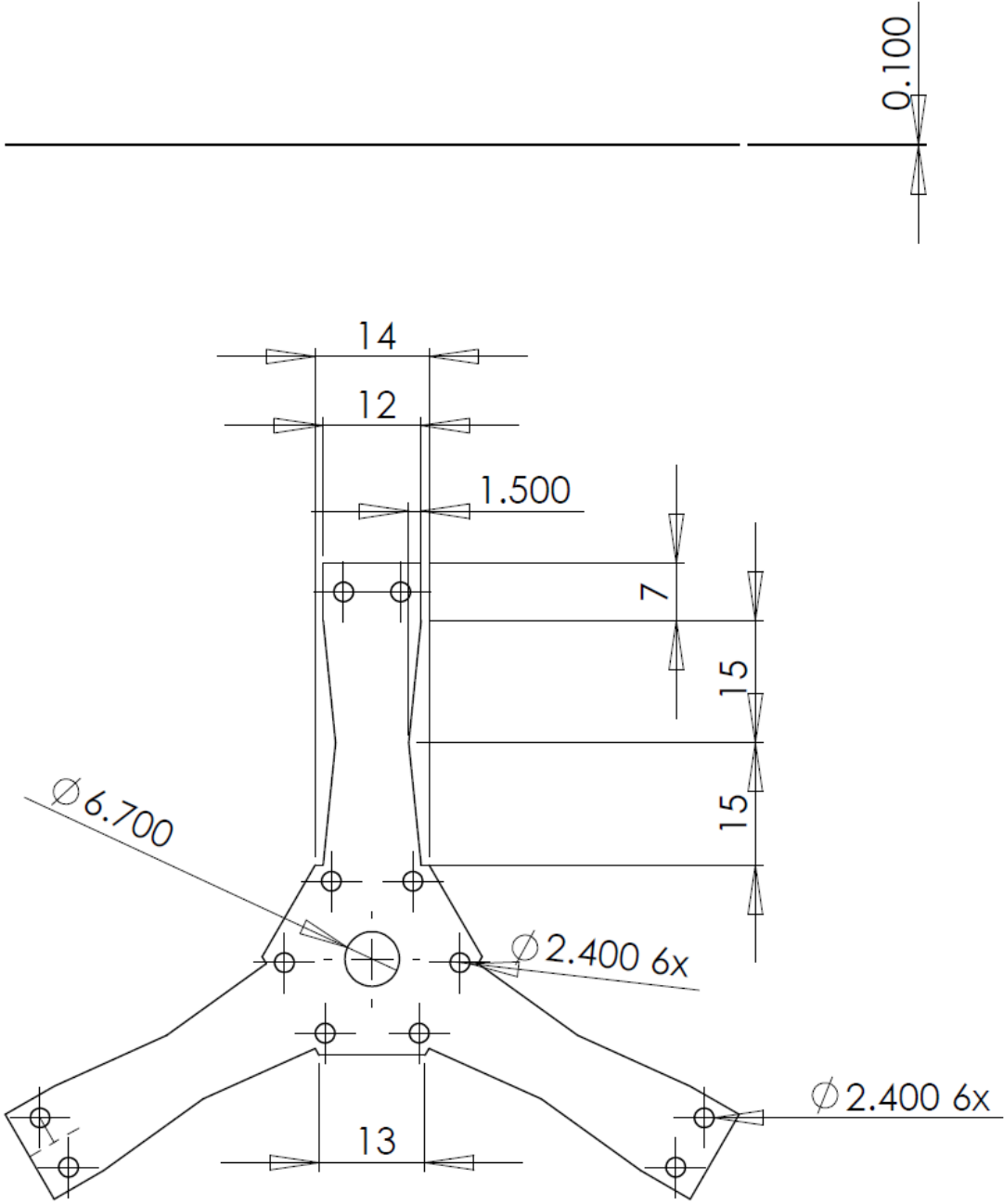
F.4. Leaf spring filling plate



F.5. Actuator filling plate

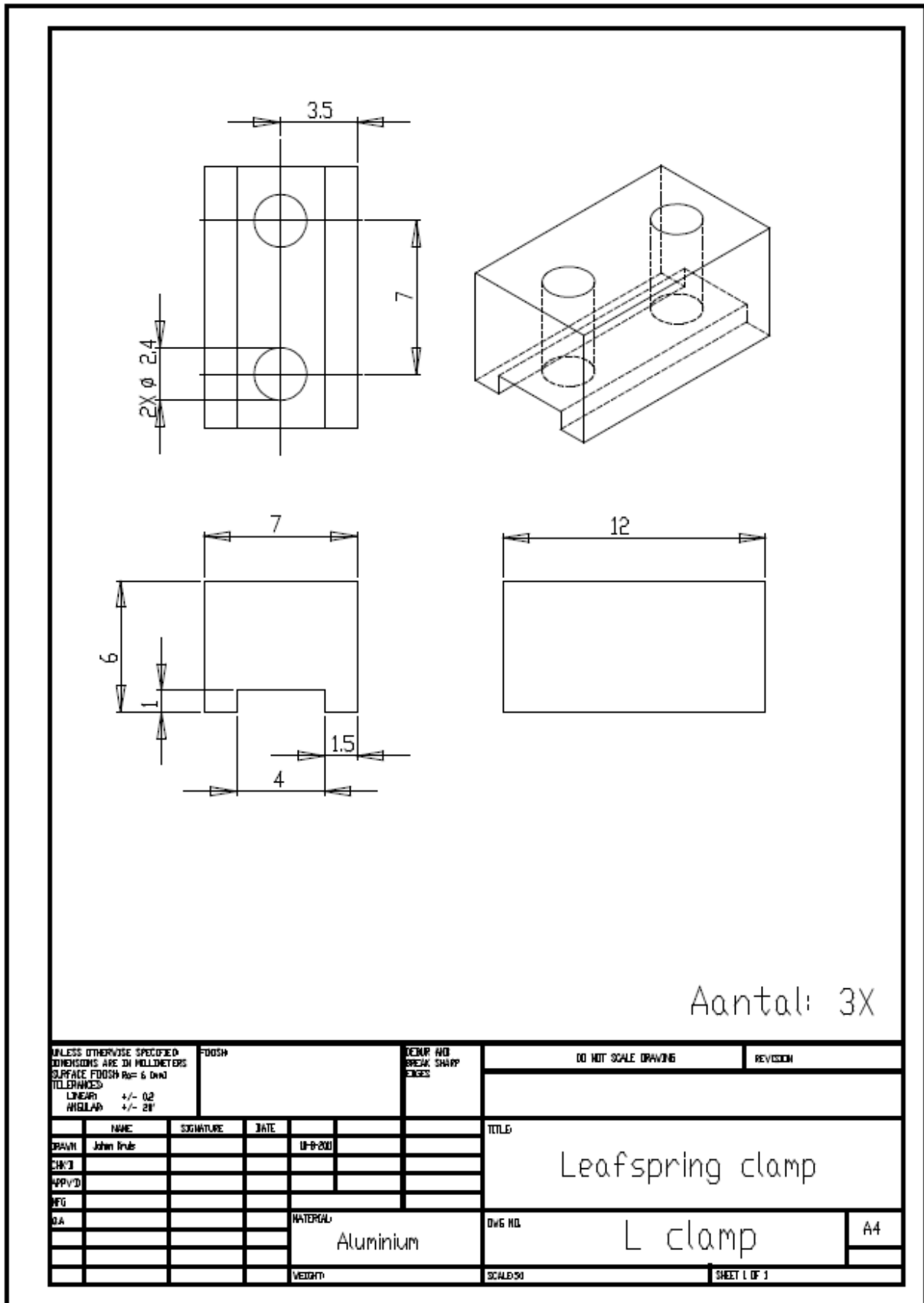


F.6. Folded leaf spring Membrane

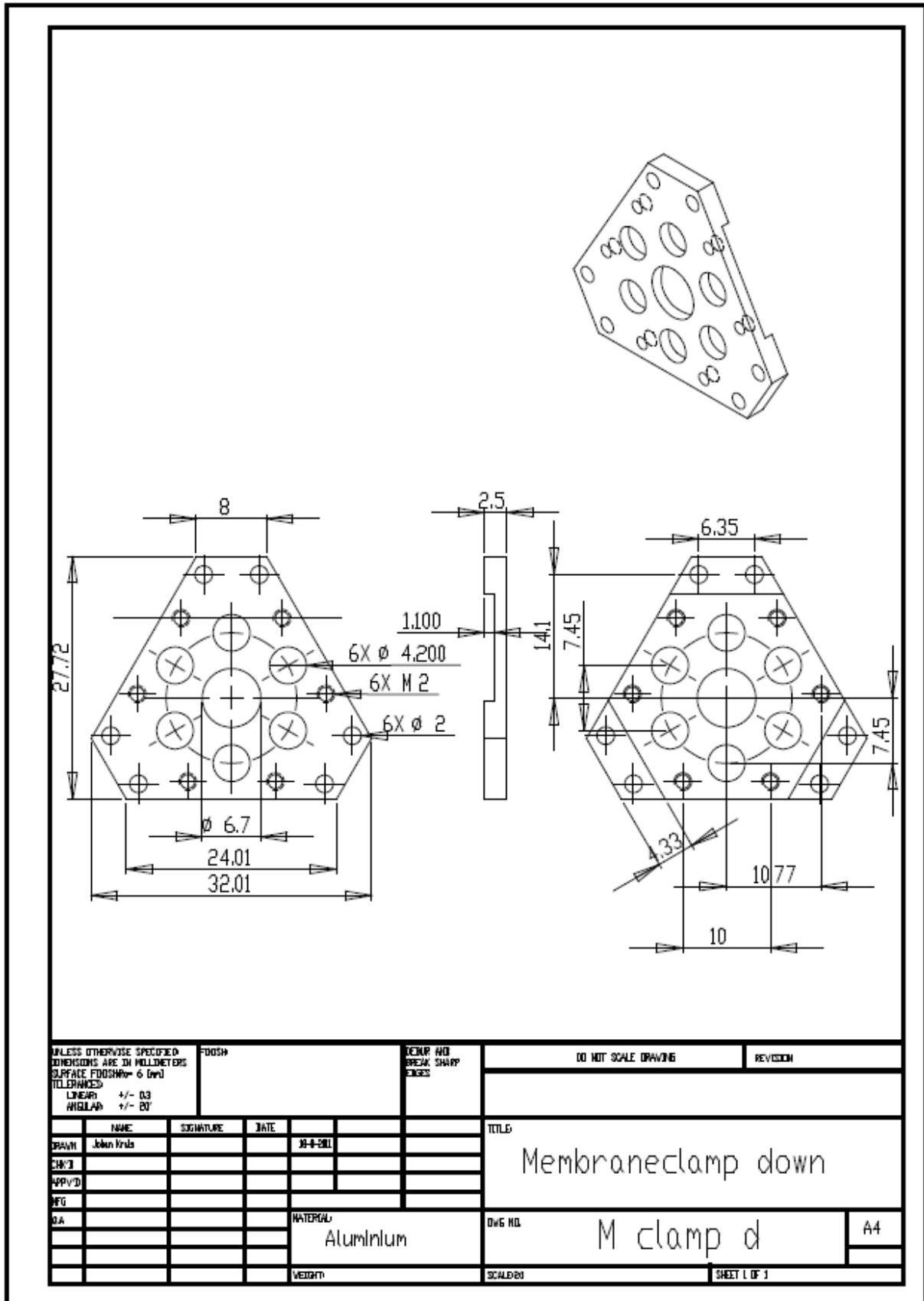


Material Hasberg 1.4310 Precision steel sheet

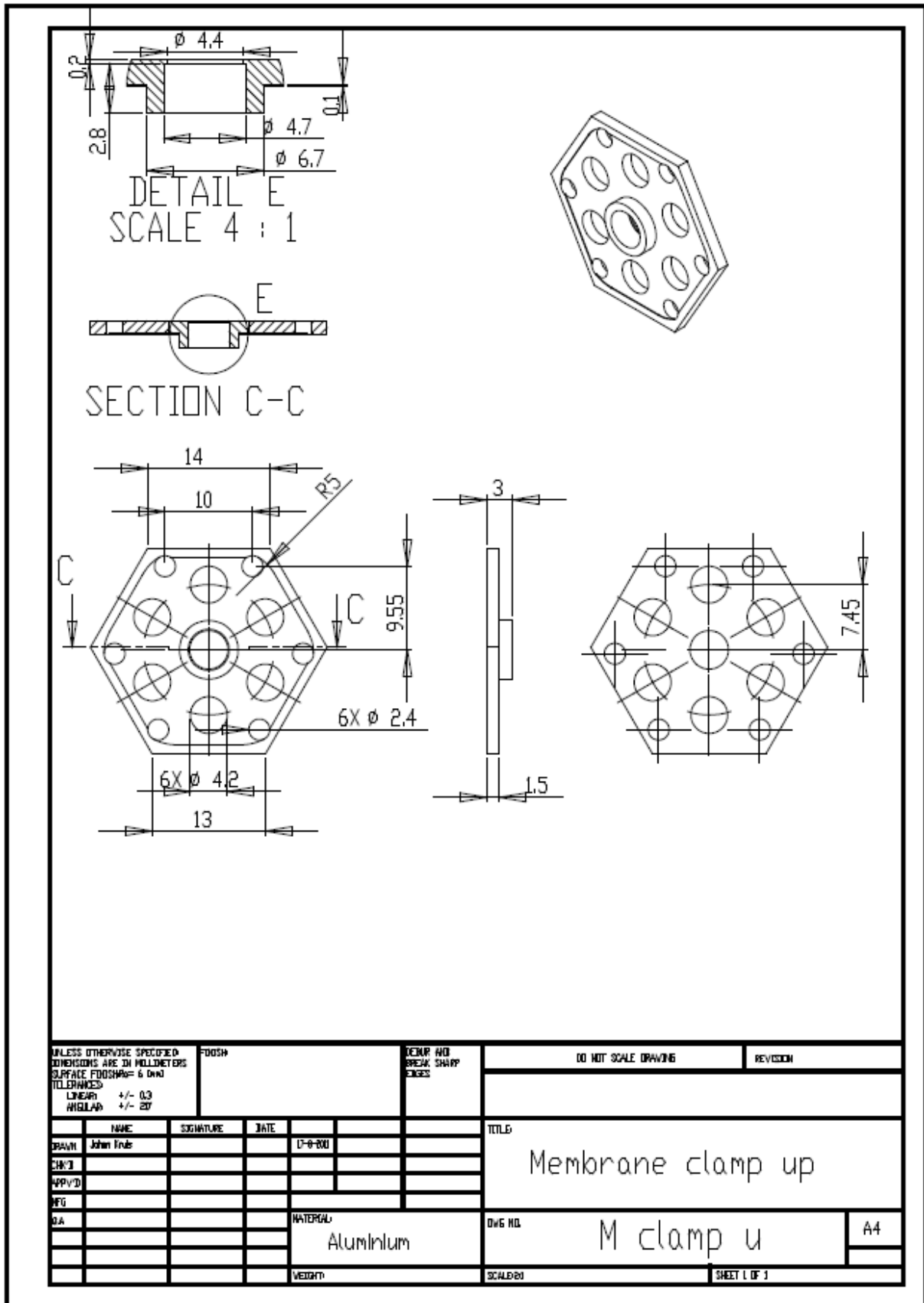
F.7. Leaf spring clamps (L clamp)



F.8. Membrane clamp (down)

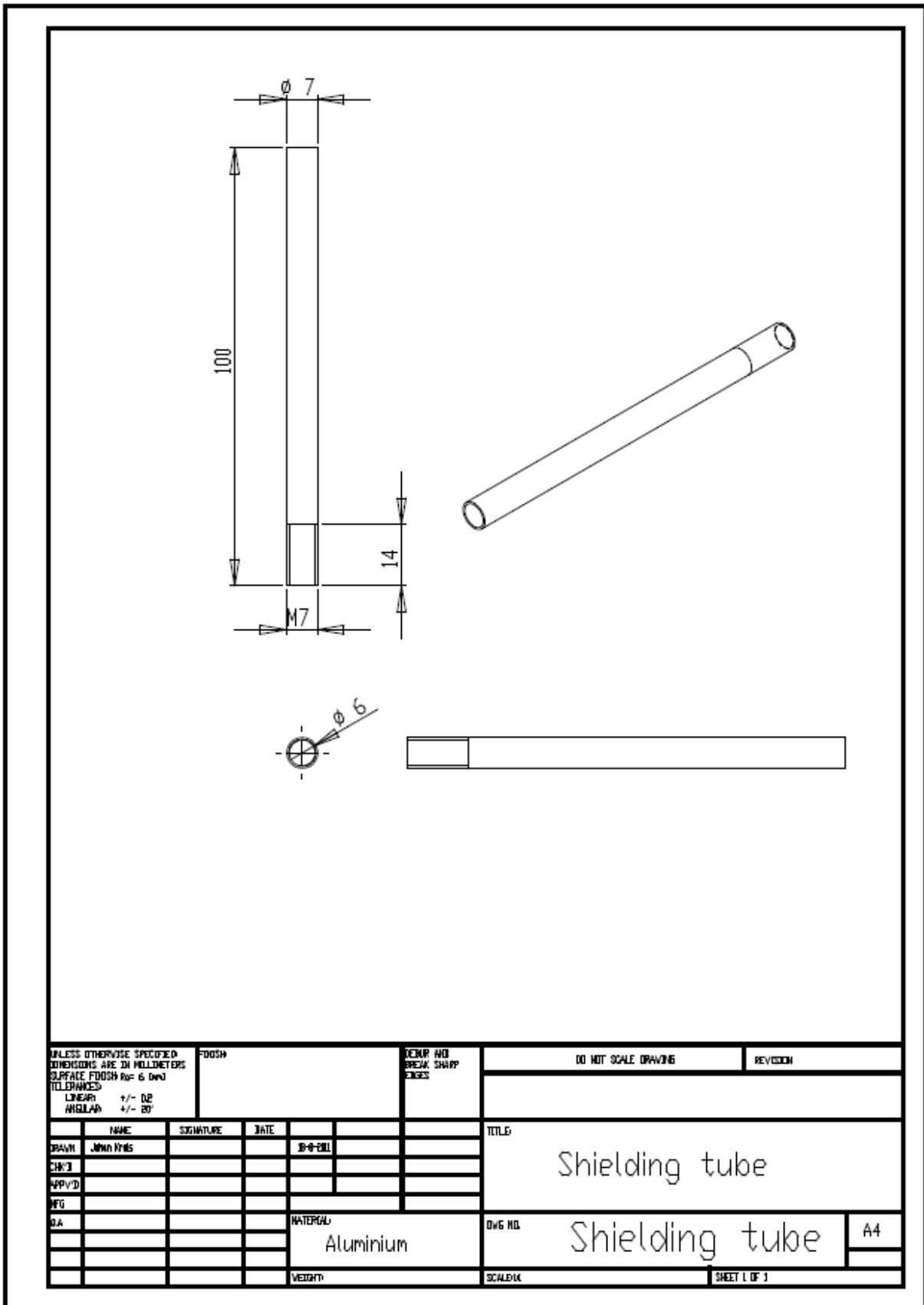


F.9. Membrane clamp (up)

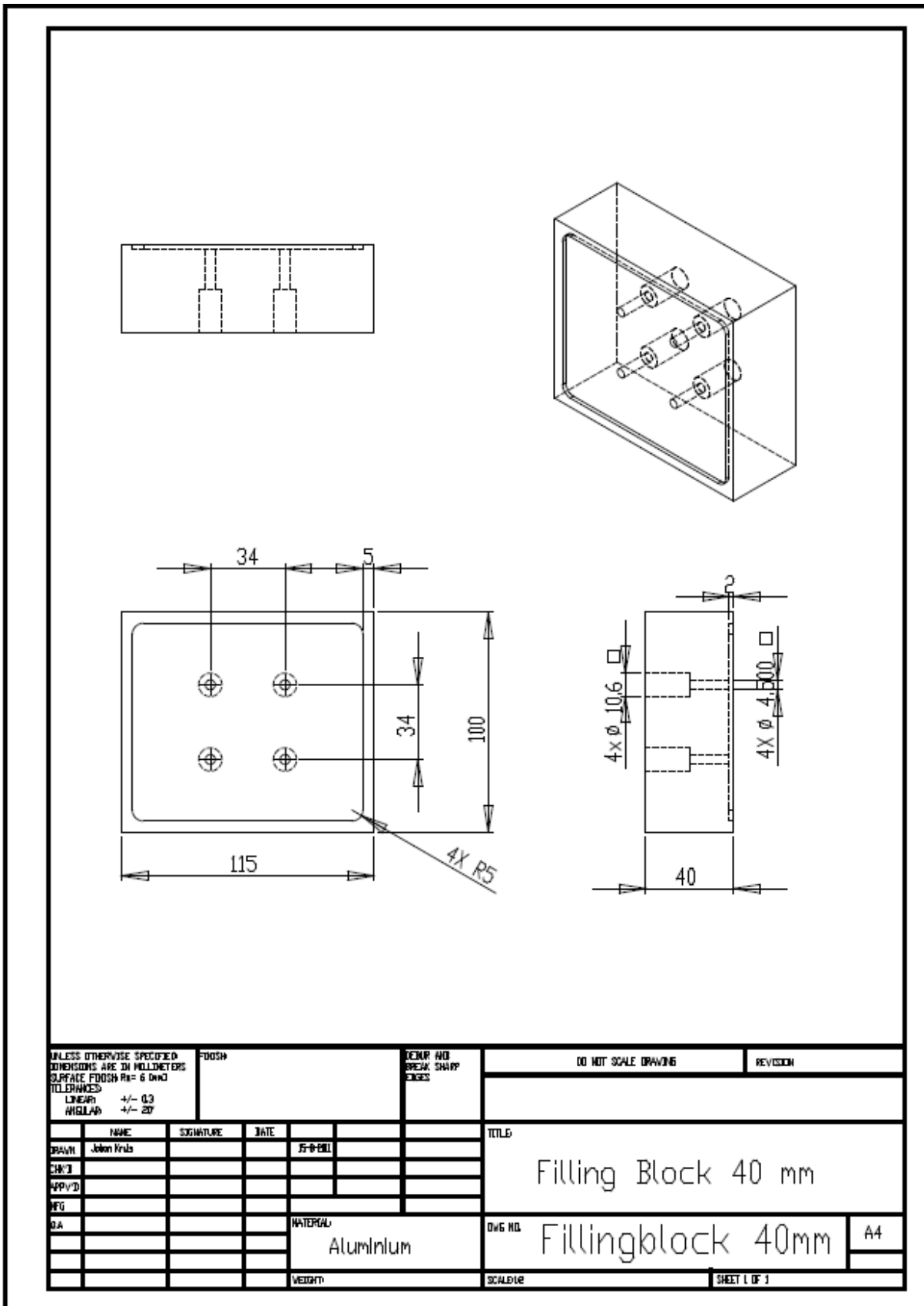




F.10. Shielding tube



F.11. Filling block



## G. Gravity and its effect on the laser scanning head

### Gravity and effective mass effects

One of the interests was the movement of the body due to gravity itself. In figure 5.37 the effect of the gravity vector is indicated. The suspension sags up to a maximum of 78.5 [ $\mu\text{m}$ ] due to gravity.

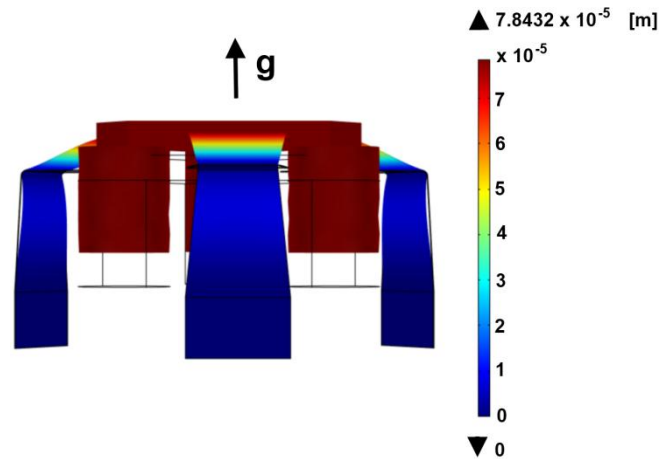


Figure 5.37: Displacement due to gravity

### Effect of orienting the gravity differently

Because during the measurements the setup was oriented differently with respect to gravity, therefore a brief analysis was made of the effect of orienting the mechanism differently with respect to gravity; the result can be seen in figure 5.38.

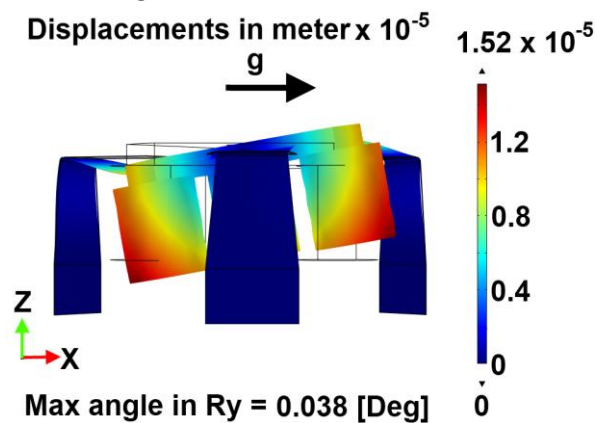


Figure 5.38: effect of orienting gravity along the X axis.

The effects of orienting the suspension with the gravity in the X direction are relatively negligible, the translations are nearly non-existent, and the angle is about 4% of the maximum range. This shows that the experiments conducted in chapter 4 can be trusted regardless of the different orientation with respect to gravity.

## H. Tolerance calculations

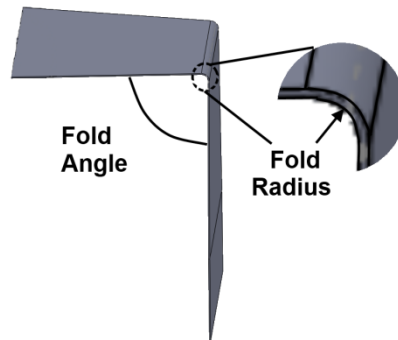


Figure 5.39: The folding angle and radius of a folded leaf spring

Two main concerns for the fabrication of the folded leaf spring membrane were the influence of the fold angle and the fold radius on the eigenfrequencies. Because the folding would be done manually and separate per folded leaf spring a first indication of imperfect folds was desired.

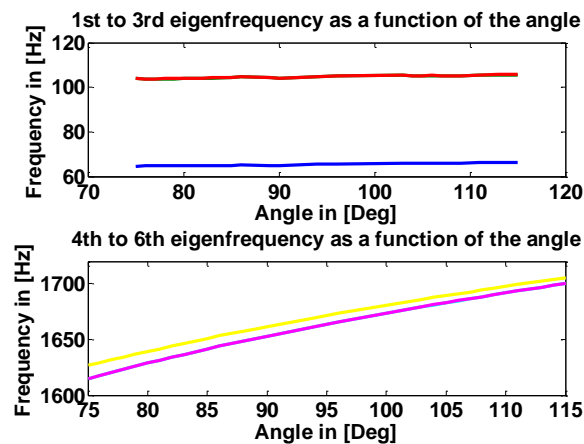


Figure 5.40: influence of the folding angle on eigenfrequency, the effect is most prominent in the 4<sup>th</sup> till 6<sup>th</sup> eigenfrequencies. It is roughly  $\pm 10$  Hz per  $\pm 5$  Degrees.

The variations of folding angle (see figure 5.40), show that the larger the folding angle, the stiffer, the construction for the higher resonant modes. This differs at most of 10 Hz per 5 Degrees for the high frequencies. For the lower three frequencies the effect is also present but even less pronounced. Thus having a constant deviation in fold angle has a negligible effect on the system performance. (Note that in the figure, the 2<sup>nd</sup> and 3<sup>rd</sup> frequencies almost overlap as do the 5<sup>th</sup> and the 6<sup>th</sup>, that is why the figure seems to show a total of 4 lines.)

The stiffening itself can be explained from the more the angle approaches 180 degrees the closer the concept is to an over constrained three leaf spring design (three leaf springs constrain a total of 9 DOFs whereas three folded leaf springs constrain only 3). The frequency drop of the torsional and bending modes of the leaf springs is related to the smaller the angle the higher the distance from the clamping to the outer volume is, resulting in larger effective inertias and reducing the effective tensile stiffness of the bottom leaf spring (the clamped part of the folded leaf spring).

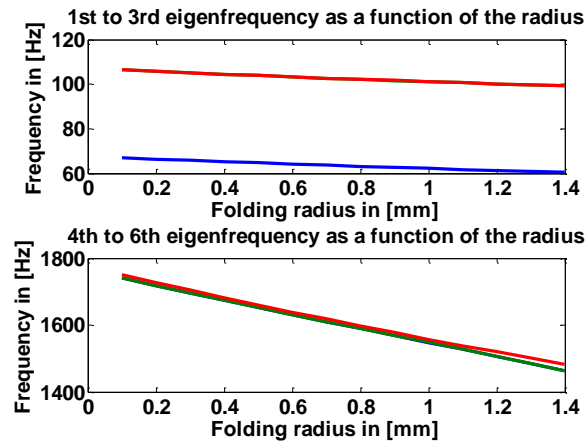


Figure 5.41: effect of the fold radius on the eigenfrequencies, the effect is most prominent in the 4<sup>th</sup> till 6<sup>th</sup> eigenfrequencies. It is roughly  $\pm 110$  Hz per  $\pm 0.4$  m.

As for the folding radius, it proved to have a much more dramatic effect on eigenfrequencies. The larger the folding radius the lower all eigenfrequencies are. Most notably the 4<sup>th</sup> until the 6<sup>th</sup> eigenfrequency. The trend is a decrease of roughly 110 Hz per 0.4 mm of radius increase. On the other hand, a too small folding radius would weaken the leaf spring, due to stress accumulation. So a trade off for the leaf springs is found for a folding radius of about 0.5 mm.

## I. System characterisation bode plots

In this appendix chapter the diagonal bode plots are supplied with their phase and coherence information. From figure 5.42 we can see that coherence is relatively good up to 200 Hz, with higher frequencies the high frequency noise starts to ruin the quality of the measurement. In figure 5.43 we can see an almost anti-resonance and second resonance, this is most likely caused by geometric misalignments not taken into account for the calculations of the bode plots.

In figure 5.44 we see the same allowable frequencies of the coherence (~200 Hz) and in figure 5.45 the effect of a 2<sup>nd</sup> resonance and anti-resonance is almost unnoticeable, indicating that this rotational axis is better measured. This could be caused by the fact that for a rotation around Y only data from two sensors is used whereas for a rotation around X data from three sensors is used to calculate the angle. In figure 5.46 the results for the coherence are similar (~200 Hz), where as in figure 5.47 We see slightly less phase drop until the resonance frequency of the rotational frequencies. It should be noted that for the Z displacement also the data from three sensors is used, however the magnitudes of these parasitic effects are significantly less visible.

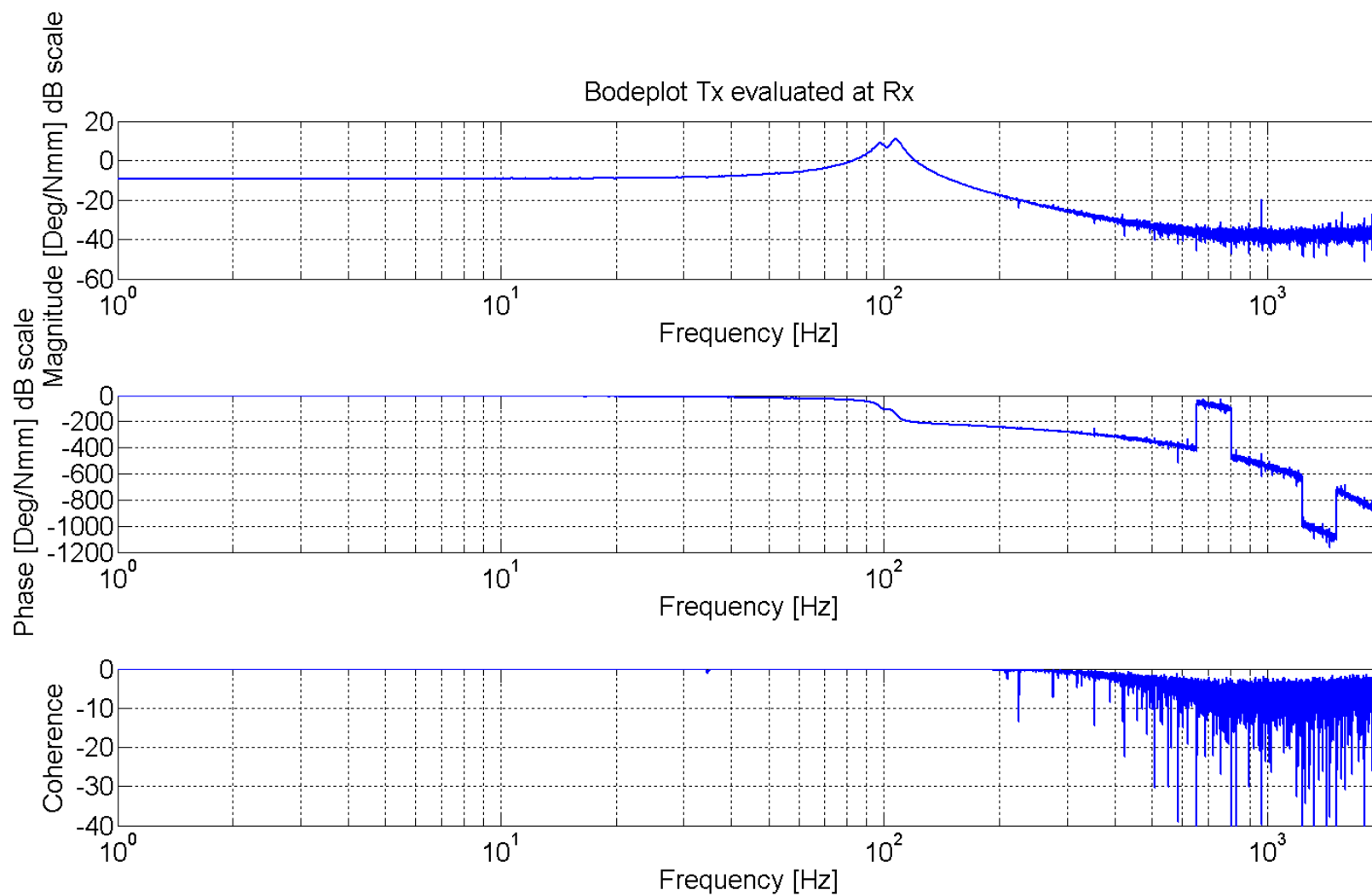


Figure 5.42: bode plot of Tx evaluated at Rx, with the added phase and coherence information.

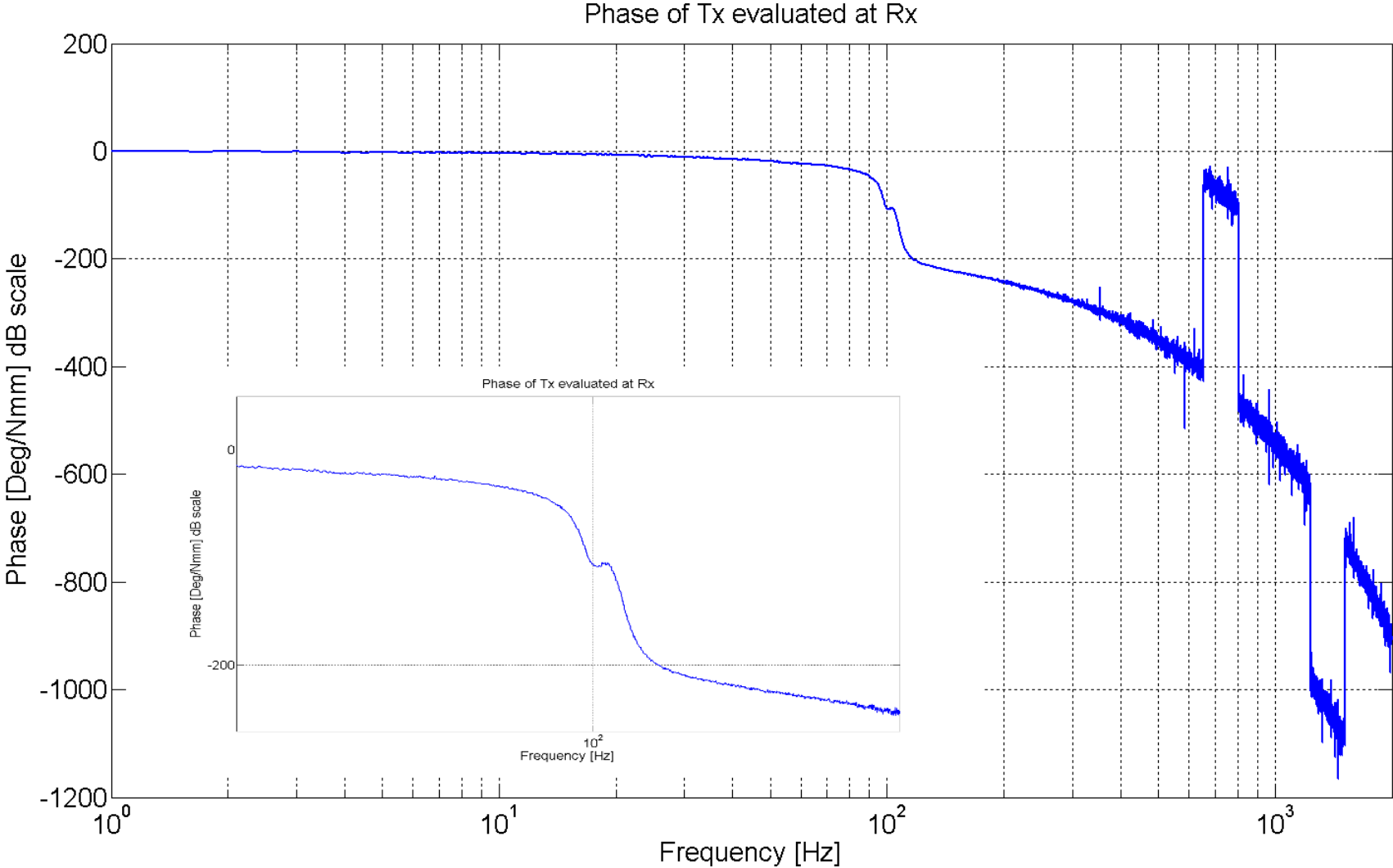


Figure 5.43: Detailed view of the Phase of Tx evaluated at Rx, we can even see an anti-resonance like effect, most likely related to geometric misalignment, and a second resonance causing the phase to drop to expected value



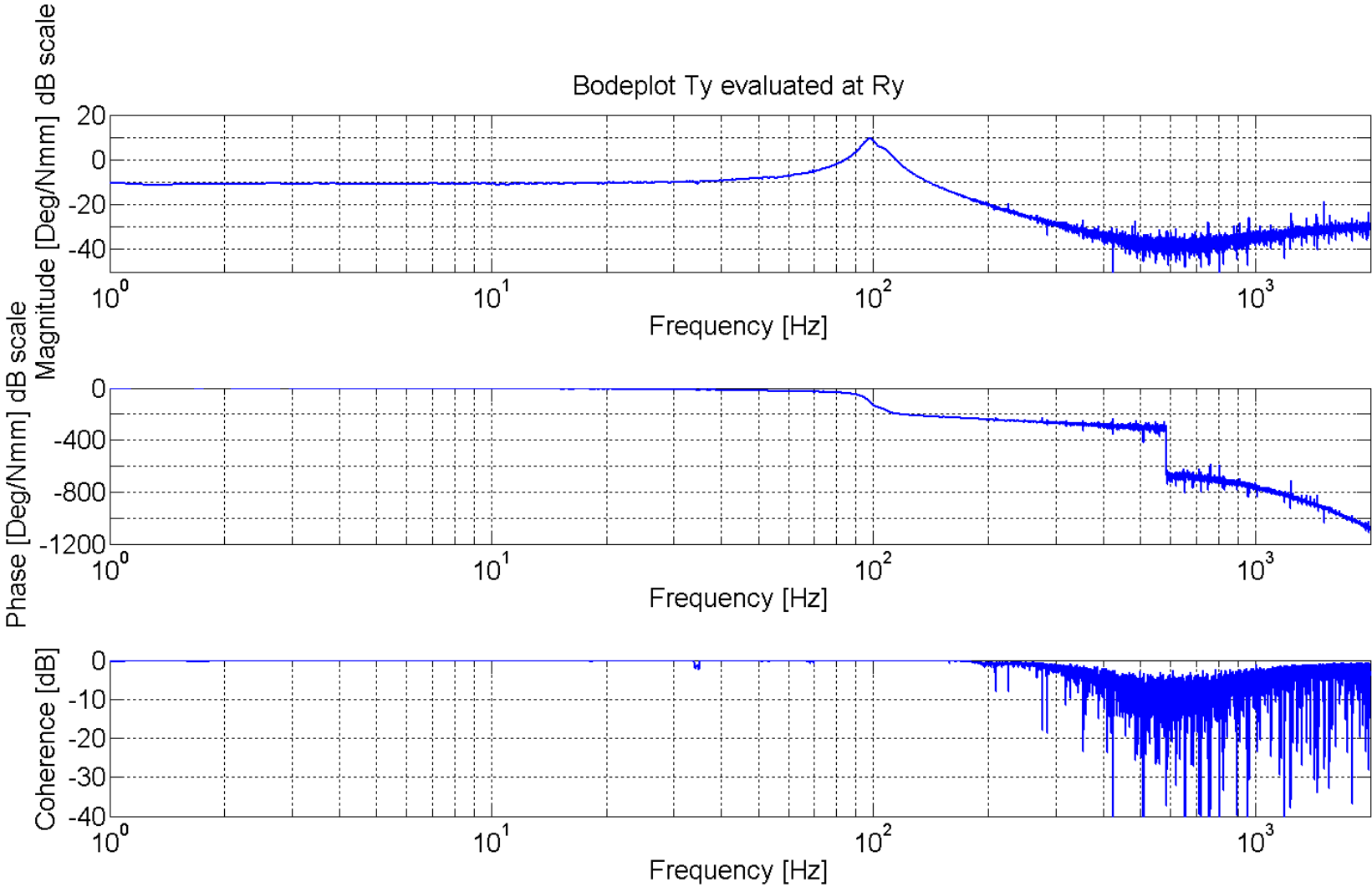


Figure 5.44: bode plot of Ty evaluated at Ry, with the added phase and coherence information.

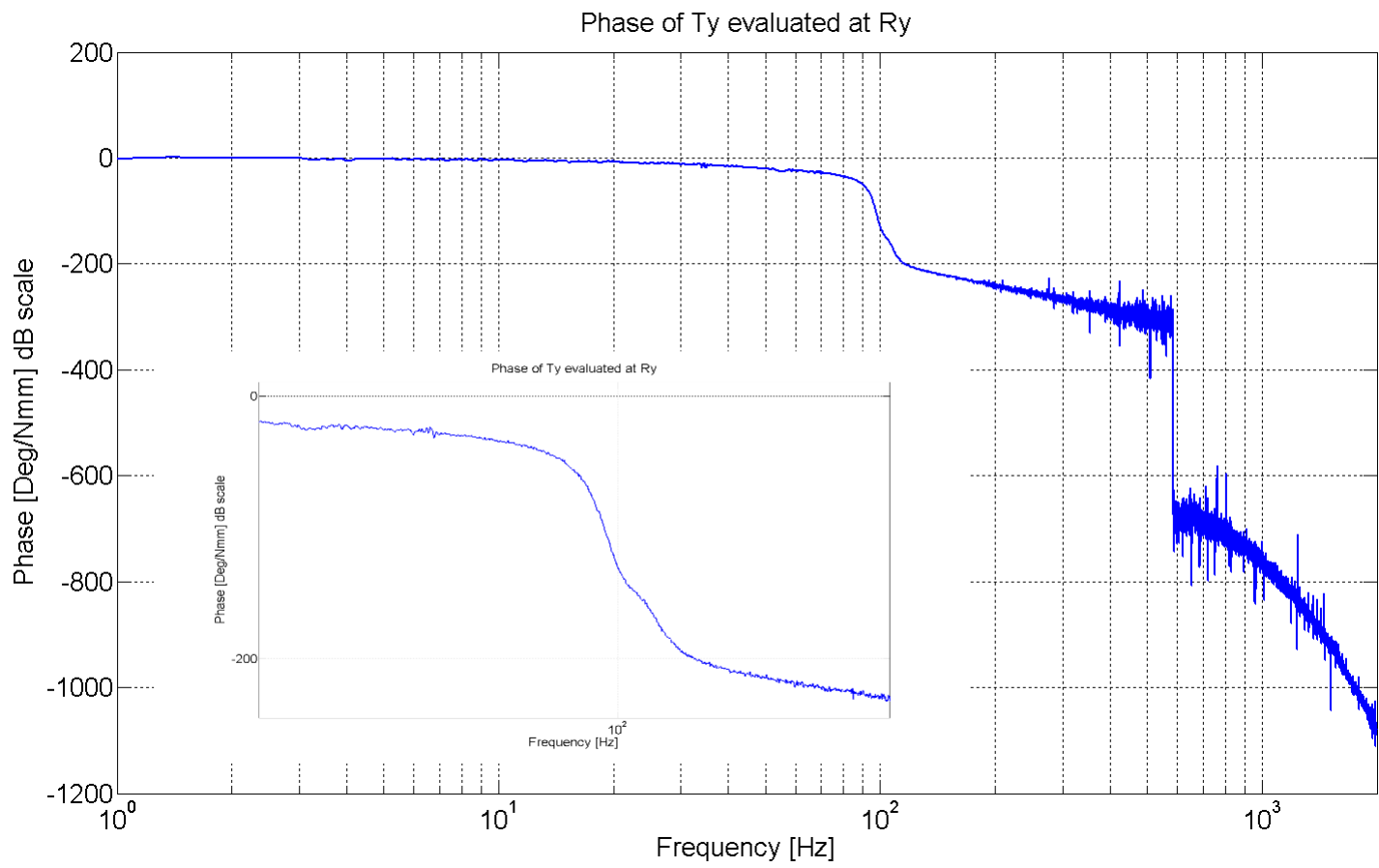


Figure 5.45: Detailed view of Ty evaluated at Ry, the parasitic effect to slightly present is much less significant as with the Tx at Rx.

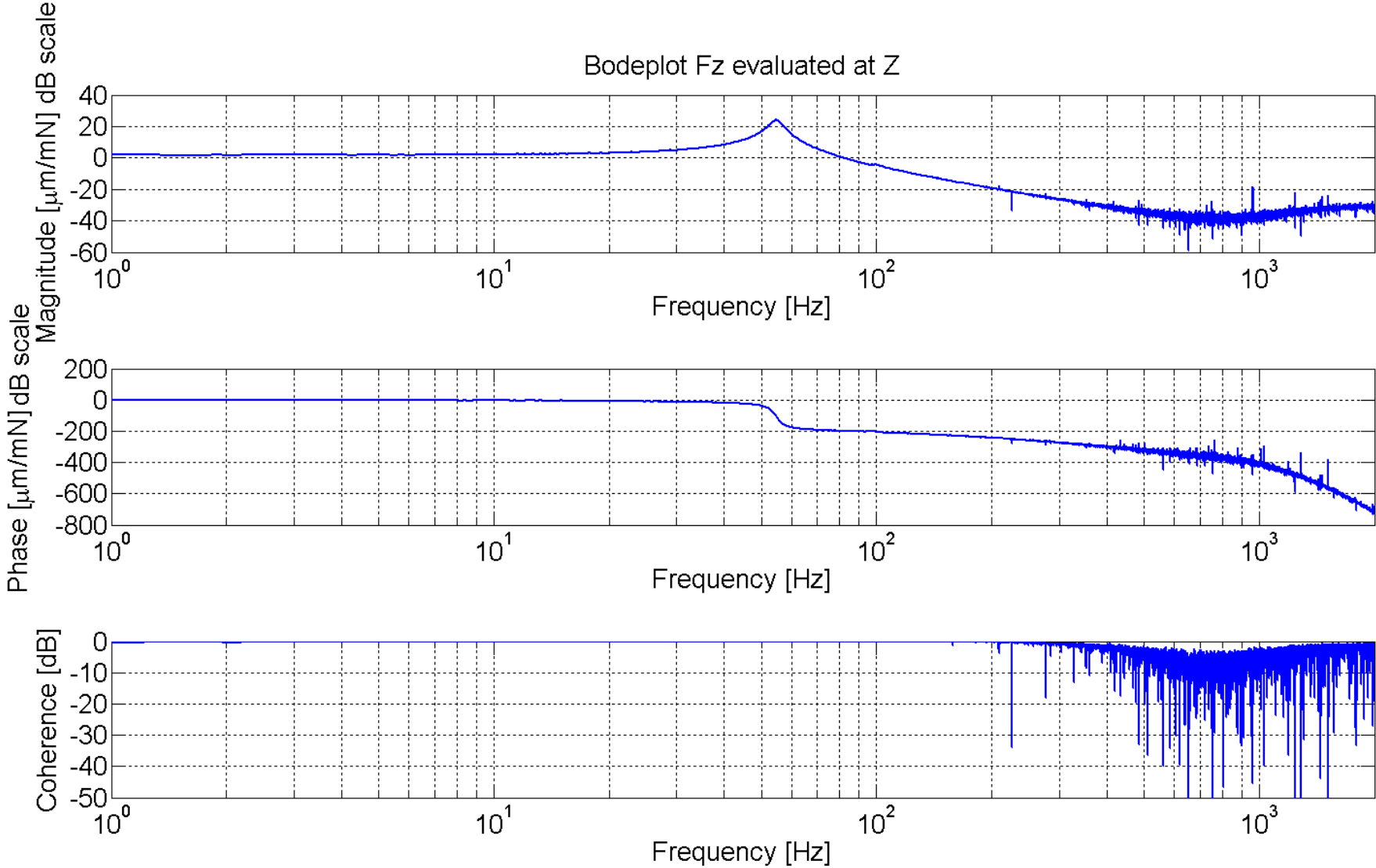


Figure 5.46 Bode plot of Fz evaluated at Z, with the added phase and coherence information.

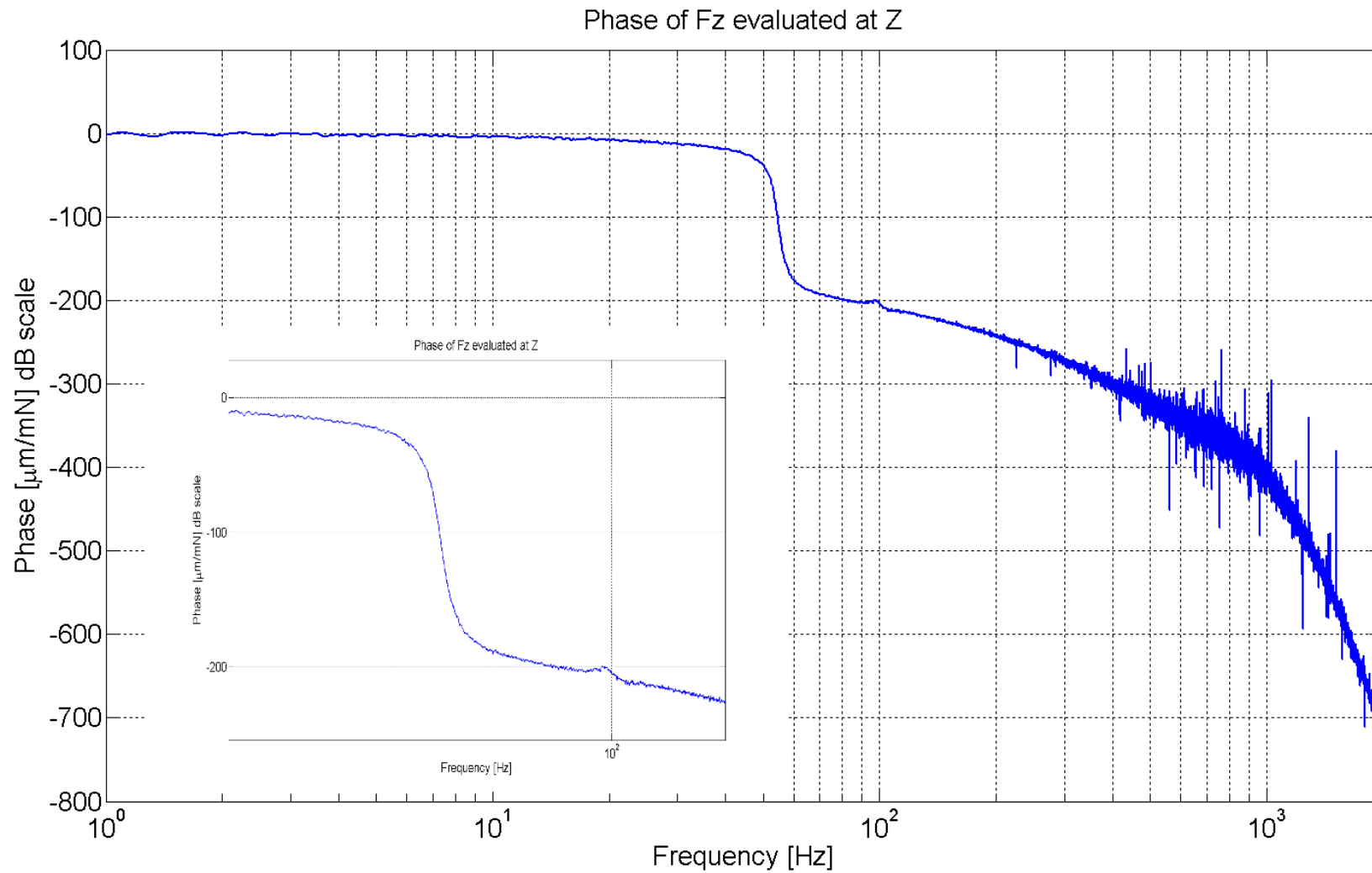


Figure 5.47: Phase of Fx evaluated at Z, we can see that around the resonance frequency of the angular frequencies there is a slightly less drop in phase, explained by imperfections in geometric tolerances, which are not taken into account in the calculation

## J. References

---

- [1] S. Rajesh en Y. Bellouard, "Towards fast femtosecond laser micromachining of fused silica: The effect of deposited energy.", *Optics Express*, vol. 18, nr. 20, pp. 21490-21497, 2010.
- [2] Y. Bellouard, "Femtosecond-laser processing of glass to create integrated microsystems", *SPIE Newsroom*, 2009.
- [3] Y. Bellouard, "Monolithic multifunctional integration in fused silica", 2006, vol. 6400, pp. 640004-640004-13.
- [4] Y. Bellouard, A. Said, M. Dugan, en P. Bado, "Fabrication of high-aspect ratio, micro-fluidic channels and tunnels using femtosecond laser pulses and chemical etching", *Optics Express*, vol. 12, nr. 10, pp. 2120-2129, mei 2004.
- [5] "Femtoprint project webpage". [Online]. Available: <http://www.femtoprint.eu/index.php>. [Accessed: 16-nov-2011].
- [6] K. M. Davis, K. Miura, N. Sugimoto, en K. Hirao, "Writing waveguides in glass with a femtosecond laser", *Optics Letters*, vol. 21, nr. 21, pp. 1729-1731, nov. 1996.
- [7] S. Nolte, M. Will, J. Burghoff, en A. Tuennermann, "Femtosecond waveguide writing: a new avenue to three-dimensional integrated optics", *Applied Physics A: Materials Science & Processing*, vol. 77, pp. 109-111, jun. 2003.
- [8] A. Szameit e.a., "Discrete Nonlinear Localization in Femtosecond Laser Written Waveguides in Fused Silica", *Optics Express*, vol. 13, nr. 26, pp. 10552-10557, dec. 2005.
- [9] C. Mauchair e.a., "Dynamic ultrafast laser spatial tailoring for parallel micromachining of photonic devices in transparent materials", *Optics Express*, vol. 17, nr. 5, pp. 3531-3542, mrt. 2009.
- [10] G. Della Valle, S. Taccheo, R. Osellame, A. Festa, G. Cerullo, en P. Laporta, "1.5  $\mu\text{m}$  single longitudinal mode waveguide laser fabricated by femtosecond laser writing", *Optics Express*, vol. 15, nr. 6, pp. 3190-3194, mrt. 2007.
- [11] L. Canioni, M. Bellec, A. Royon, B. Bousquet, en T. Cardinal, "Three-dimensional optical data storage using third-harmonic generation in silver zinc phosphate glass", *Optics Letters*, vol. 33, nr. 4, pp. 360-362, feb. 2008.
- [12] M. Beresna, M. Gecevičius, P. G. Kazansky, en T. Gertus, "Radially polarized optical vortex converter created by femtosecond laser nanostructuring of glass", *Applied Physics Letters*, vol. 98, p. 201101, 2011.
- [13] Y. Bellouard, A. Said, en P. Bado, "Integrating optics and micro-mechanics in a single substrate: a step toward monolithic integration in fused silica", *Optics Express*, vol. 13, nr. 17, pp. 6635-6644, 2005.
- [14] F. Madani-Grasset en Y. Bellouard, "Femtosecond laser micromachining of fused silica molds", *Optics Express*, vol. 18, nr. 21, pp. 21826-21840, okt. 2010.
- [15] Y. Bellouard en M.-O. Hongler, "Femtosecond-laser generation of self-organized bubble patterns in fused silica", *Optics Express*, vol. 19, nr. 7, pp. 6807-6821, mrt. 2011.
- [16] Y. Bellouard, T. Colomb, C. Depeursinge, M. Dugan, A. A. Said, en P. Bado, "Nanoindentation and birefringence measurements on fused silica specimen exposed to low-energy femtosecond pulses", *Optics Express*, vol. 14, nr. 18, pp. 8360-8366, 2006.
- [17] Y. Bellouard, E. Barthel, A. A. Said, M. Dugan, en P. Bado, "Scanning thermal microscopy and Raman analysis of bulk fused silica exposed to lowenergyfemtosecond laser pulses", *Optics Express*, vol. 16, nr. 24, pp. 19520-19534, nov. 2008.
- [18] B. Lenssen, "Glass Micro Actuator made by femtosecond laser exposure and chemicaletching". Internal TU/e Publication, 30-aug-2011.
- [19] A. Schaap, Y. Bellouard, en T. Rohrlack, "Optofluidic lab-on-a-chip for rapid algae population screening", *Biomedical Optics Express*, vol. 2, nr. 3, pp. 658-664, mrt. 2011.
- [20] E. Hecht, *Optics*, 4e ed. Addison Wesley, 2001.

- [21] A. Goshaw, "Phy 42: Fundamentals of Physics", *Optics course Duke university*. [Online]. Available: <http://www.phy.duke.edu/courses/042/>. [Accessed: 16-nov-2011].
- [22] Lumenera Corp, "Lu205". [Online]. Available: <http://www.lumenera.com/products/industrial-cameras/lu205.php>. [Accessed: 16-nov-2011].
- [23] D. C. Montgomery en G. C. Runger, *Applied Statistics and Probability for Engineers, 4th Edition*, 4e ed. John Wiley & Sons, 2006.
- [24] "NIST/SEMATECH e-Handbook of Statistical Methods". [Online]. Available: <http://www.itl.nist.gov/div898/handbook/>. [Accessed: 18-nov-2011].
- [25] "Adjusted Coefficient of Determination | R Tutorial". [Online]. Available: <http://www.r-tutor.com/content/adjusted-coefficient-determination>. [Accessed: 18-nov-2011].
- [26] V. E. Gough, "Universal tyre test machine", pp. 117-133, 1962.
- [27] L. Tsai en F. Tahmasebi, "Synthesis and analysis of a new class of six-degree-of-freedom parallel minimanipulators", *Journal of Robotic Systems*, vol. 10, nr. 5, pp. 561-580, jul. 1993.
- [28] R. Clavel, "DELTA, a fast robot with parallel geometry", pp. 91-100, apr. 1988.
- [29] J. P. Merlet en C. Gosselin, "Nouvelle architecture pour un manipulateur à 6 degrés de liberté", vol. 26 No 1, pp. 77-90, 1991.
- [30] Y. Bellouard, *Microrobotics: Methods and Applications*, 1e ed. CRC Press, 2009.
- [31] van de Wouw, N., *Multibody Dynamics Lecture notes TU/e*. 2007.
- [32] P. T. Jutte, *Light path design for optical disk systems*. Eindhoven : Technische Universiteit Eindhoven, 2005.
- [33] P. C. J. N. Rosielle, "Constructieprincipes: voor nauwkeurig bewegen en positioneren". Technische Universiteit Eindhoven, 2011.
- [34] C. Werner, *A 3D translation stage for metrological AFM*. Eindhoven: Technische Universiteit Eindhoven, 2010.
- [35] "COMSOL Multiphysics® User's guide". okt-2010.
- [36] "Präzisionslehrenband, Sonderbreiten, Messingfolien, Fühlerlehren, Hasberg-Schneider". [Online]. Available: <http://www.hasberg-schneider.de/praezisions-lehrenband-sonderbreiten.html>. [Accessed: 18-nov-2011].
- [37] "Online Materials Information Resource - MatWeb". [Online]. Available: <http://www.matweb.com/>. [Accessed: 21-nov-2011].
- [38] "CEDRAT Group: APA®". [Online]. Available: <http://www.cedrat.com/en/mechatronic-products/actuators/apa.html>. [Accessed: 02-dec-2011].
- [39] "PI: Products | Selection Guide | PI Piezo Actuator, Piezo Transducer, Piezoceramics". [Online]. Available: [http://www.physikinstrumente.com/en/products/piezo/piezo\\_actuator\\_selection.php#preload](http://www.physikinstrumente.com/en/products/piezo/piezo_actuator_selection.php#preload). [Accessed: 02-dec-2011].
- [40] "BEI Kimco Magnetics - Voice Coil Actuators & Brushless DC Motors for Industrial, Aerospace/Defense, and Transportation Applications". [Online]. Available: [http://www.beikimco.com/actuators\\_linear\\_CYL\\_unhoused.php](http://www.beikimco.com/actuators_linear_CYL_unhoused.php). [Accessed: 20-nov-2011].
- [41] "Piezosystem Jena - company providing: piezo technology, nanopositioning equipment, nanoautomation, piezo stages, micropositioning, tilting mirror, high resolution positioning, metrology, fiber switches, microscopy, stack actuators, AFM components, object". [Online]. Available: [http://www.piezojena.com/en/Home\\_\\_2/](http://www.piezojena.com/en/Home__2/). [Accessed: 02-dec-2011].
- [42] "Piezo | Piezoelectric | Piezoceramics | Piezoelectric ceramics | Piezo components | Piezo actuators | Piezo sensors | Piezo transformers | Piezo generators | Piezo drivers | Piezo transducers | Noliac Group | Piezo actuator drive | PAD". [Online]. Available: <http://www.noliac.com/>. [Accessed: 02-dec-2011].
- [43] J. R. Brauer, *Magnetic Actuators and Sensors*, 1e ed. Wiley-IEEE Press, 2006.
- [44] "H2w technologies voice coils". [Online]. Available: <http://www.h2wtech.com/Pages/Product-Overview.aspx>. [Accessed: 02-dec-2011].
- [45] "TMMotion voice coils". [Online]. Available: <http://www.tmmotion.com/english/index.asp>. [Accessed: 02-dec-2011].

- [46] J. C. Compter, *The Design and Application of industrial linear motors*. Eindhoven University of Technology. Internal publication, 2010.
- [47] "PHILTEC: fiberoptic sensors". [Online]. Available: <http://www.philtec.com/downloadsupport/faqs.html>. [Accessed: 21-nov-2011].
- [48] "TUeDACS". [Online]. Available: <http://www.tuedacs.nl/>. [Accessed: 22-nov-2011].
- [49] S. Skogestad en I. Postlethwaite, *Multivariable Feedback Control: Analysis and Design*, 2e ed. Wiley-Interscience, 2005.
- [50] special optics, "Bestform laser lens theory" . .
- [51] R. Kingslake en R. B. Johnson, *Lens Design Fundamentals, Second Edition*, 2e ed. Academic Press, 2009.
- [52] Zemax, "ZEMAX: Software for Optical System Design Manual". [Online]. Available: [http://www.zemax.com/index.php?option=com\\_content&task=category&sectionid=9&id=68&Itemid=164](http://www.zemax.com/index.php?option=com_content&task=category&sectionid=9&id=68&Itemid=164). [Accessed: 17-nov-2011].